ABSTRACT

Title of thesis: THE EFFECTS OF TIDAL FORCES ON THE MINIMUM ENERGY CONFIGURATIONS OF THE FULL THREE-BODY PROBLEM

Edward Levine, Master of Science, 2016

Thesis directed by: Professor Christine Hartzell
Department of Aerospace Engineering

We investigate the evolution of minimum energy configurations for the Full Three Body Problem (3BP). A stable ternary asteroid system will gradually become unstable due to the Yarkovsky-O'Keefe-Radzievskii-Paddack (YORP) effect and an unpredictable trajectory will ensue. Through the interaction of tidal torques, energy in the system will dissipate in the form of heat until a stable minimum energy configuration is reached. We present a simulation that describes the dynamical evolution of three bodies under the mutual effects of gravity and tidal torques. Simulations show that bodies do not get stuck in local minima and transition to the predicted minimum energy configuration.

THE EFFECT OF TIDAL FORCES ON THE MINIMUM ENERGY CONFIGURATIONS OF THE FULL THREE-BODY PROBLEM

by

Edward Levine

Thesis submitted to the Faculty of the Graduate School of the
University of Maryland, College Park in partial fulfillment
of the requirements for the degree of
Master of Science
2016

Advisory Committee:
Professor Christine Hartzell, Chair/Advisor
Professor Derek Paley
Professor Olivier Bauchau

Dedication

To my Mom and Dad who inspire me to dream bigger than what life can offer.

Acknowledgments

I want to foremost thank my advisor, Dr. Hartzell, who worked tirelessly with me improving this research until it was something we could both be happy about. Through her dedication and knowledge, I was exposed to an amazing world of simulation physics that I intend to explore further and expand my own knowledge on. I want to thank my labmates, Tom, Anthony, and Dylan, who were always there for me whenever a question arose and were always more than willing to lend their expertise. Working with them has been a pleasure and I hope to continue our technical talks on a frequent basis. Finally, I wish to thank my girlfriend, Amanda, for her patience when listening to me talk about this project. She was a great person to bounce off new ideas and granted me an inquisitive audience for when I would talk through my work.

Table of Contents

List of Tables

List of Figures

Chapter 1: Introduction

1.1 Introduction

Tracing the movement of celestial bodies into the past provides information on where the bodies came from and their dynamical evolution. The simplest formulation for modeling the dynamic evolution of solar system bodies is to treat gravitational objects as point masses of infinite density. The point mass approximation is suitable for modeling planets and moons orbiting the sun at relatively large distances because these celestial bodies will never come into contact. For our study, we wanted to predict the transient and long-scale evolution of a ternary asteroid system that has experienced angular acceleration due to the YORP effect. Scheeres has shown that a ternary system will exist in one of several equilibrium depending on its angular momentum [1]. These equilibrium involve surface contacts and rely on the finite size of the bodies.

1.1.1 Motivation

There are two main problems with predicting the evolution of a ternary asteroid systems that must be resolved to obtain accurate, long-term results. In order to properly model asteroids in close proximity, especially those that come into contact along their surfaces, the asteroids must be treated as finite volumes. A point-mass assumption alone would allow for asteroids to come arbitrarily close to each other and does not allow for surfaces to maintain persistent contacts.

With the finite volume model, asteroids may collide and form persistent contacts, as well as orbit one another from a distance. The rigidity of two asteroids prevent their surfaces from penetrating, thus limiting the minimum distance and gravitational potential between the asteroids. A system of two or more asteroids will contain at least one equilibrium configuration for which the bodies will retain their relative positions and velocities until perturbed by an outside force. For the case of three perfectly spherical bodies, Scheeres has identified a total of seven unique equilibrium configurations [1]. These configurations are solely dependent on the angular momentum of the ternary system, and as such, any change to their angular momentum can cause the bodies to transition to another equilibrium configuration.

Additionally, finite volume bodies are subject to a variety of forces that affect their motion and rotation. Celestial bodies orbiting the sun will experience a change in spin rate due to non-radial thermal re-radiation of the sun's energy. This is known as the Yarkovsky-O'Keefe-Radzievskii-Paddack (YORP) effect, and it will gradually increase or decrease the angular momentum of orbiting bodies [2]. Over long enough timescales (10^5 years), the YORP effect can alter the angular momentum of orbiting bodies to the point that their relative equilibrium configuration becomes unstable [3]. For the three-body system, the bodies will transition away from one of the seven equilibrium configurations. The motion of the bodies during this transition are governed by N-body gravitational dynamics for which there is no analytic solution. The motion of the bodies are also affected by tidal forces, which cause energy dissipation in the system and prevent any analytical study of the bodies during the transition.

Tidal forces cause the dissipation of mechanical energy in the three-body system, resulting in the transition of the system between equilibria configurations. Tidal forces naturally arise from gravity gradients across the surface of the bodies, a result of the bodies having a distributed, non-point-like mass. Due to the time dependent nature of tidal forces, their specific application and effect can not be analytically determined beforehand; rather, the dynamics of the bodies must be numerically simulated.

Thus to accurately predict the evolution of a ternary asteroid system, each body must be regarded with a physical spatial dimension and allowed to interact with each other at their surface boundaries. Furthermore, each body must be subjected to a time-varying tidal force to slowly dissipate excess mechanical energy.

1.1.2 Previous Work

The dynamical evolution of the full three-body problem has been detailed by Scheeres [1]. The Sundman inequality for a point-mass system provides an upper-bound for the angular momentum H of an N-body system based on the total kinetic energy T and polar moment of inertia I_p [4].

$$H^2 \leq 2I_pT \tag{1.1}$$

By considering the moments of inertia matrix I for finite-volume bodies, Scheeres defines an alternate moment of inertia for the system $I_H = \hat{H} \cdot I \cdot \hat{H}$, where $\hat{H}$ is the direction of the total angular momentum in inertial space. By using I_H, the upper limit to the Sundman inequality can be refined such that: $H^2 \leq 2I_HT$. We state without proof (which can found in the paper by Scheeres [1]) that using this new inequality definition allows for the total energy of the finite-volume system E to be bounded below by a minimum energy function $\mathcal{E}$ which depends only on H, I_H and the total potential energy U. By considering all generalized spatial arrangements of the three bodies, the possible equilibrium configurations are obtained from solutions to the minimum energy function. Scheeres derived the corresponding energy and angular momentum of each equilibrium configuration, and has speculated on the likely transition pathways between equilibria. To verify his model and predictions requires numerical simulation of the full three-body system at varying initial configurations and angular momenta.

In a paper by Jacobson and Scheeres [3], it was shown that “rubble pile” asteroids could repeatedly undergo rotational fission and either form a stable binary or ternary system, or re-accrete into a single asteroid. Over a large timespan of 10^6 years, the YORP effect could cause an asteroid to shed or fission mass to form a binary or ternary system. Their simulation showed that with the right mass distribution, one of the asteroids of the binary system would split into a third body, forming a chaotic ternary system. They estimated that within 10^7 years, tidal forces would synchronize the rotation and orbital rates of the bodies so that the system as a whole would be indefinitely stable. However, their study did not test for the transitions between equilibrium configurations of the stable ternary system after subjected again to the YORP effect. Thus, it is still inconclusive how these transitions occur and whether the final configuration agrees with the analytical predictions made by Scheeres [1].

1.1.3 Thesis Contributions

This thesis presents an algorithm written in MATLAB that simulates the full three-body problem. The algorithm simulates a ternary system that has undergone YORP angular acceleration to the point of inducing a transition to a lower energy configuration. It incorporates collision and contact physics between bodies, allowing simulated bodies to come together and form persistent contacts. The trajectory of the bodies are affected by ellipsoidal gravitational potentials as well as time-varying tidal forces. The bodies are propagated until the system begins to converge to a stable equilibrium and shows signs of transitioning to a tidally locked, minimum energy configuration.

The efficacy of different numerical propagators are tested and compared. The performance of each algorithm is judged primarily by its ability to conserve energy and angular momentum, and conform to the underlying physical constraints preventing bodies from penetrating. Explicit integrators, like Runge-Kutta and Velocity Verlet, are simple to implement and are computational cheap but struggle to resolve numerically stiff contact interactions, often resulting in long-term energy instability. Implicit integrators, such as the SHAKE algorithm [5], are able to resolve physical constraints and system-wide energy invariants down to a pre-specified tolerance, but suffer from increased complexity and computation time. Additionally, two methods to compute contact forces are tested and compared; the first being a geometric contact force algorithm [6] [7], the second being a soft-sphere discrete element method [8].

Using simulation results, we confirm the pathway transitions between minimum energy configurations of the full three-body problem as predicted by Scheeres. The three bodies often form pseudo-equilibrium states during the transition, during which time the bodies are suspended in an unstable orbit resembling an equilibrium state until enough energy is decayed for the system to collapse to a ground state. Our results show that the bodies do not get stuck in any local energy minima during their transitions between minimum energy configurations, which is a conclusion that could not be tested with the analytical theory. For each possible transition, the bodies converge to the minimum energy configuration predicted by Scheeres based on the angular momentum of the system.

1.1.4 Thesis Overview

In Chapter 2, we present an in-depth description of the problem along with the mathematical representation of the three-body system. Chapter 3 provides the dynamics used to model the motion of the bodies. Chapter 4 discusses the simulation hierarchy and integrator schemes used to numerically propagate the system. In Chapter 5, we present the results of the simulation. Chapter 6 explains the sources of error in the simulation and how they affected the simulation results. Suggested improvements and conclusion are provided in Chapter 7.

Chapter 2: Problem Background

2.1 The Full Three-Body Environment

We will begin by formalizing the equilibrium configurations of the full three-body problem. Assume the three bodies are identical spheres with diameter d and mass m. The bodies are considered rigid, preventing their surfaces from interpenetrating, such that the minimum distance between any two bodies is given by d. We now restrict the motion of the bodies to a single plane, say the XY plane in Cartesian space, for simplicity. Likewise, the bodies are restricted to rotate about the axis perpendicular to their plane of motion (Z direction). The spin rate of a body i about its center of mass is given by $\dot{\psi}_i$ and the rotation of a body i about the barycenter is given by $\dot{\theta}_i$. The origin of the inertial frame is placed at the barycenter of the three body system at the initial state. The position of each body i is given by $\vec{r}_i$ and the relative position between two bodies i and j is given by $\vec{r}_{ij} = \vec{r}_i - \vec{r}_j$. Given the diameter of the bodies, the relative positions are bounded by $\|\vec{r}_{ij}\| \geq d$. These variables are expressed in Figure 2.1.

The energies and momentum of the system can be specified in terms of the relative position and velocities between two bodies:

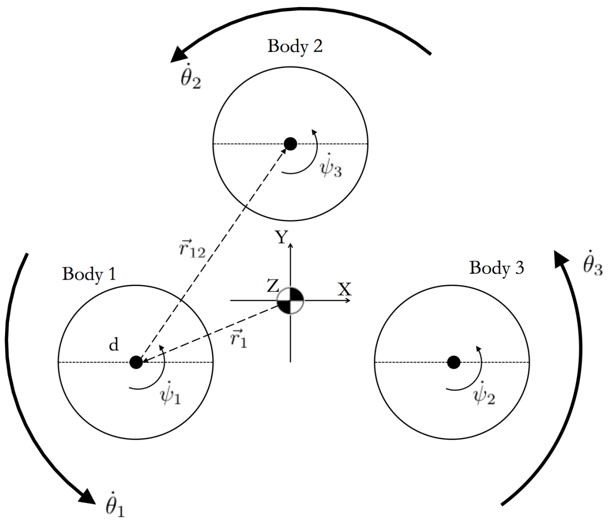

Figure 2.1: Body frame showing the relative positions between bodies and their rotation rates. Z is perpendicular to the XY plane and by the right-hand rule, points out of the page.

$$T = \frac{m}{3}\sum_{i=1}^{2}\sum_{j=i+1}^{3}\frac{(\dot{\vec{r}}_{ij}\cdot\dot{\vec{r}}_{ij})}{2} + \frac{1}{2}\sum_{i=1}^{3}\frac{md^2}{10}\dot{\psi}_i \tag{2.1}$$

$$U = -G\sum_{i=1}^{2}\sum_{j=i+1}^{3}\frac{m^2}{\|\vec{r}_{ij}\|} \tag{2.2}$$

$$\mathbf{H} = \frac{m}{3}\sum_{i=1}^{2}\sum_{j=i+1}^{3}(\dot{\vec{r}}_{ij}\times\dot{\vec{r}}_{ij}) + \frac{1}{2}\sum_{i=1}^{3}\frac{md^2}{10}\dot{\psi}_i \tag{2.3}$$

$$I_H = \frac{m}{3}\sum_{i=1}^{2}\sum_{j=i+1}^{3}(\vec{r}_{ij}\cdot\vec{r}_{ij}) + \frac{1}{10}\sum_{i=1}^{3}md^2 \tag{2.4}$$

$$E = T + U \tag{2.5}$$

where T = total system kinetic energy, U = total system potential energy, H = total system angular momentum, I_H = system polar moment of inertia, and E = total energy of system. The goal is to determine the relative positions of the bodies that minimize the total system energy. These minimum energy states are the equilibrium configurations of the system. To find them, a refined version of the Sundman inequality is applied to the system which provides a lower bound on the total energy of the bodies [1]:

$$\mathcal{E} = \frac{H^2}{2I_H} + U \leq E \tag{2.6}$$

where $\mathcal{E}$ = minimum energy function and $I_H = \hat{H} \cdot \mathbf{I} \cdot \hat{H}$ is the moment of inertia along the axis aligned with the total angular momentum unit vector $\hat{H}$. Here, $\mathbf{I}$ is the moment of inertia matrix of a spherical body.

When written in this form, the minimum energy function $\mathcal{E}$ is dependent only on the angular momentum of the system, the relative position of the three bodies, and the physical properties of the bodies, thereby removing any dependence on kinetic energy. We can simplify the expressions for U and I_H by eliminating the summation terms of Equation 2.4 to simplify:

$$U = -Gm\left[\frac{1}{r_{12}} + \frac{1}{r_{23}} + \frac{1}{r_{31}}\right] \tag{2.7}$$

$$I_H = \frac{m}{3}(r_{12}^2 + r_{23}^2 + r_{31}^2) + \frac{3}{10}md^2 \tag{2.8}$$

where $r_{ij} = \|\vec{r}_{ij}\|$, the 2-norm of the relative position vector.

Before these expressions are substituted into $\mathcal{E}$, the diameter d is nondimensionalized to 1 such that $r_{ij} \geq 1$, the polar moment of inertia along the $\hat{H}$ direction I_P is scaled by md^2, and the potential energy U is scaled by Gm^2/d. This gives the following expression for the minimum energy function:

$$\bar{\mathcal{E}} = \frac{\bar{H}^2}{2[(\bar{r}_{12}^2 + \bar{r}_{23}^2 + \bar{r}_{31}^2)/3 + 0.3]} - \left[\frac{1}{\bar{r}_{12}^2} + \frac{1}{\bar{r}_{23}^2} + \frac{1}{\bar{r}_{31}^2}\right] \tag{2.9}$$

$$I_H = \frac{1}{3d^2}(r_{12}^2 + r_{23}^2 + r_{31}^2) + \frac{3}{10} \tag{2.10}$$

$$\bar{\mathcal{E}} = \frac{\mathcal{E}d}{Gm^2} \tag{2.11}$$

$$\bar{H}^2 = \frac{H^2}{Gm^3 d} \tag{2.12}$$

where the $b\bar{a}r$ notation represents normalized quantities. As can be seen, the minimum energy function is only a function of the angular momentum of the system and the relative distance between the three bodies. The equilibrium configurations are found by examining the critical points of the minimum energy function. Figure 2.2 shows the two generic contact arrangements of the three bodies, where θ is the constraint angle and R is the distance from the center of the resting pair to the center of the third body.

The critical points of the minimum energy function occur at the values of θ and R such that the derivatives of $\mathcal{E}$ with respect to θ and R are 0. Similarly, the stability

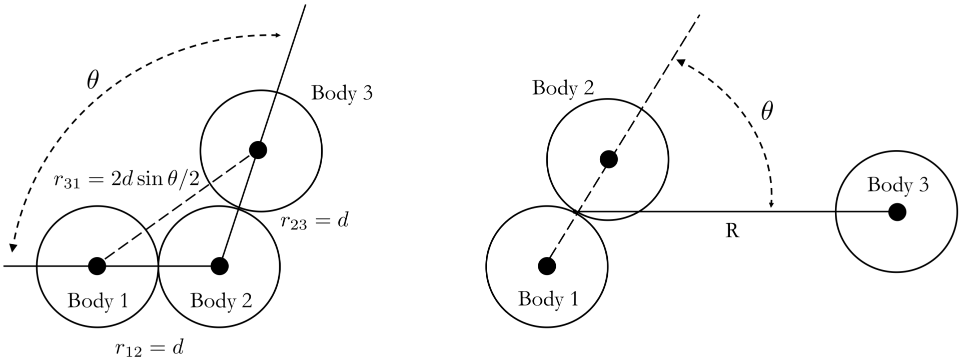

Figure 2.2: Generic arrangement for resting contact between three bodies (left) and two bodies (right). Reproduced from Scheeres. [1]

of each equilibrium point is found by looking at the sign of the second derivative of $\mathcal{E}$. Scheeres has showed that there are seven unique equilibrium configurations (discounting those under symmetry transformations), as seen in Figure 2.3.

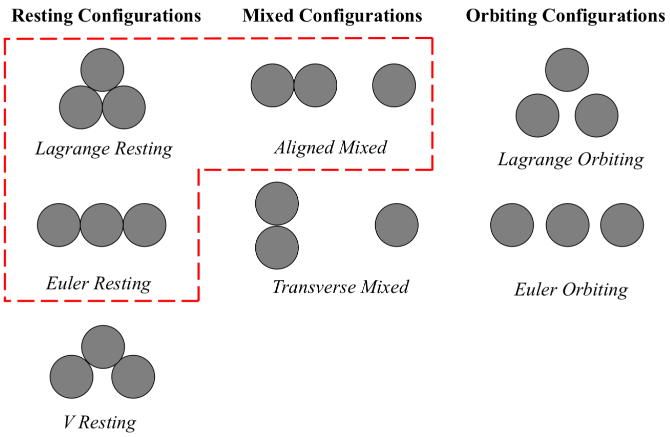

Figure 2.3: Reproduced from Scheeres. [1] Relative equilibrium configurations for the Full Three-Body Problem. Those boxed in red are the only stable configurations, all other are energetically unstable.

The three Resting Configurations (see Figure 2.3) have the three bodies in persistent (static) contact with zero relative motion at the point of contact. Each of the resting configurations are simply a permutation of two bodies in contact with the third body at an angle bounded between $60° \leq \theta \leq 300°$. As such, the resting configurations are defined by the angle the third body makes with the axis connecting the center of masses of the other two bodies. The Mixed Configurations are distinguished by two bodies in static contact with a third body offset along the axis that is either parallel or perpendicular to the axis connecting the two bodies in contact. The Orbiting Configurations have all three bodies physically separated.

The relative distances r_{ij} between bodies in contact for each configuration are constant, so by referring back to Equation 2.6, we have that angular momentum is the only variable that affects the minimum energy of the system (assuming physical properties of the bodies are constant). The bodies in each equilibria are tidally locked - the rotation rate of each body about its center $\dot{\psi}_i$ is equal to the rotation rate of each body about the system barycenter $\dot{\theta}_i$. As will be discussed in Chapter 3, this is an important distinction because bodies not tidally locked will dissipate energy as a result of tidal forces. Any arbitrary system and arrangement of three bodies will dissipate energy until one of the seven equilibrium configurations is reached and the bodies are tidally locked.

The energy, stability, and existence of each equilibrium configuration depends on the value of angular momentum for the system. Figure 2.4 shows the range of angular momenta (given in terms of $\bar{H}^2$) for which certain configurations are possible. The colors are used to indicate if a configuration is energetically stable in each interval. As $\bar{H}^2$ is increased/decreased through different intervals, the stability of a configuration can change. For example, consider the Euler Resting configuration at $\bar{H}^2 = 0$, which is energetically unstable. When $\bar{H}^2$ for this system is increased past a threshold of 1.98375, the configuration becomes stable and the system will tend back towards this nominal configuration under small perturbations. Similarly,

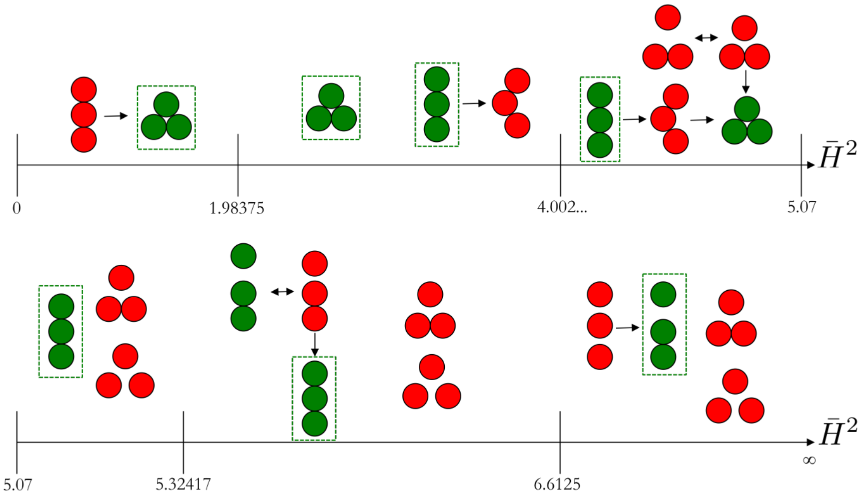

Figure 2.4: Reproduced from Scheeres. [1] The diagram shows the possible equilibrium configurations within different ranges of normalized angular momentum values $\bar{H}^2$ along the horizontal axis. Configurations marked in red are unstable and those marked in green are stable. A configuration boxed in green indicates the minimum energy configuration for the specified interval of normalized angular momentum. Arrows between configurations show how the transition between states might occur.

new configurations may bifurcate into existence while others cease to exist as $\bar{H}^2$ increases. For example, when $\bar{H}^2$ for a stable Resting Euler configuration is increased through $\bar{H}^2 = 6.6125$, the Resting Euler configuration ceases to exist and will transition to either the Aligned Mixed configuration. Given an initially unstable configuration for a given value of angular momentum, we wish to understand the evolution of the system to the stable equilibrium. As we will show, the trajectory of the bodies and whether the system can become stuck in local energy minima can not be analytically determined, even though the final equilibrium configuration can be determined [1].

When a system transitions between equilibrium states, it will always transition from a higher energy configuration to a lower energy configuration. Unstable equilibria transition to a stable lower energy state, notionally the minimum energy state.

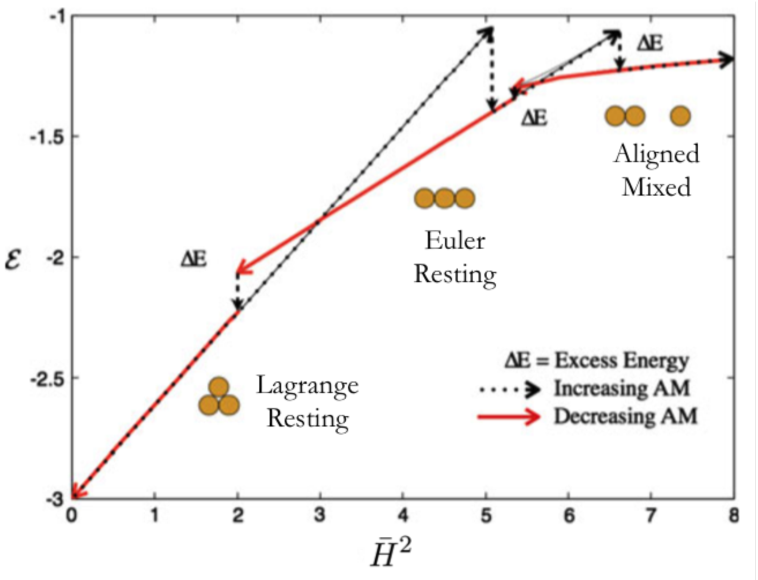

Figure 2.5: Reproduced from Scheeres. [1] The plot shows how excess mechanical energy emerges from a transitioning system. Going from left to right, the dotted black line shows how the energy of the Lagrange Resting configuration changes as $\bar{H}^2$ is increased. At a value of $\bar{H}^2 = 2.99$, LR and ER configurations are equal in energy, but LR is still stable here so the system will remain in the LR configuration. At a value of 5.07, the LR configuration ceases to exists and the system will begin to transition to the Euler Resting configuration, which is lower in energy at this value of angular momentum.

Configurations that are no longer physically viable will transition to a new minimum energy configuration, as can be seen in Figure 2.5. Starting from a minimum energy configuration, there are four possible transition:

1. Lagrange Resting (LR) to Euler Resting (ER)
    - As $\bar{H}^2$ is increased through 5.07, the bodies roll along each other and straighten out. Often one body separates from the bunch and rejoins following a collision. This transition accounts for the largest excess mechanical energy to be dissipated.
2. Euler Resting (ER) to Aligned Mixed (AM)

   - As $\bar{H}^2$ is increased through 6.6125, one of the outer bodies breaks away from the remaining two and orbits the barycenter at a fixed distance to form an Aligned Mixed configuration. The Aligned Mixed configuration is the only stable equilibria for all higher values of $\bar{H}^2$.

3. Aligned Mixed (AM) to Euler Resting (ER)
   - As $\bar{H}^2$ is decreased through 5.32417, the singular orbiting body reaccretes with the two contacting bodies to form an Euler Resting configuration. While excess energy is decaying, the central body in the configuration may change 1 or more time(s).

4. Euler Resting (ER) to Lagrange Resting (LR)
   - As $\bar{H}^2$ is decreased through 1.98375, the central body is squeezed to one side and forms a temporary V-Rest configuration before the bodies collapse into a Lagrange Resting configuration.

These are the four cases that are tested in this thesis. In all instances, the change in angular momentum instantaneously affects the equilibria configurations without altering the energy of the system. The energy of the system then exceeds the energy associated with the new minimum energy configuration based on the value of $\bar{H}^2$. Before the system can reach the new minimum energy configuration, it must dissipate its excess energy. While dissipating the excess energy, the bodies will follow a non-trivial trajectory and may collide with each other many times. The only way to analyze this transition is to numerically simulate the bodies and track their resulting, highly nonlinear motion until they reach the new stable equilibrium configuration.

In order to accurately simulate the behavior of the bodies during a transition, we model the three most important forces that govern the behavior of the bodies. The first force is the mutual gravitation between bodies that has already been expressed in the derivation of the equilibrium configurations. The second necessary force is the contact force between bodies whose surfaces are in contact, that is, when $r_{ij} = d$. The contact force ensures that bodies do not interpenetrate. Collisions between bodies are modeled as perfectly inelastic, which is the first mode of energy decay in the system. The final modeled force is a tidal force that serves as the second mode for excess energy decay. The tidal force is a result of gravity gradients between bodies that is able to decay excess energy in the system and synchronize body rotation rates at any distance of separation. The formulation of body dynamics and these three forces are discussed in greater detail in the next chapter.

Chapter 3: System Dynamics

3.1 Equations of Motion

We begin the derivation of the body dynamics by first describing the coordinates of a body in the inertial frame. The bodies are assumed to be, in general, ellipsoids with dimensions given by a, b, c. We consider only the planar motion of the bodies and are interested in tracking the translation and rotation of the bodies in the XY plane. The position of Body N is specified by the location of the body's center of mass, given by the cartesian coordinates (x_n, y_n), with the origin of the system located at the system barycenter. Next, we specify the semi-major axis $\hat{a}_n$ of Body n for a general ellipsoid. If the geometric projection onto the XY plane is circular, then the semi-major axis is initially taken as an arbitrary radial vector. For this project, we only consider and simulate spherical bodies with a circular projection on the XY plane, although we present generalized equations for ellipsoidal bodies. Finally, we define three angles, $\psi_n, \theta_{nm}, \phi_{nm}$, that track the rotation of the each body relative to the other bodies and the inertial frame. Here, ψ_n is the angle measured from the inertial X axis to $\hat{a}_n$, θ_{nm} is the angle between $\hat{r}_{nm}$ and the inertial X axis, and $\phi_{nm} = \psi_n - \theta_{nm}$ is the angle between $\hat{a}_n$ and $\hat{r}_{nm}$. Once again, the barycenter between the three bodies is taken as the origin of the system.

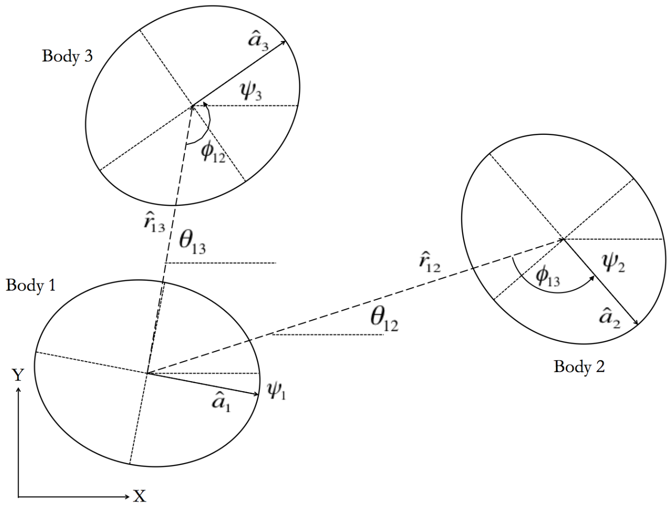

Figure 3.1: Relative Body Angles

Of these three angles, it is only necessary to numerically integrate ψ_n for each body because the other two angles can be calculated from basic geometry. The angle θ_{nm} is calculated as: $\theta_{nm} = atan2(r_{nm,y}, r_{nm,x})$, that is, the two argument arctan function with the y and x components of $\vec{r}_{nm}$ as inputs. The state vector for the system is:

$$\mathbf{q} = \begin{bmatrix} x_1 & y_1 & \psi_1 & \cdots & x_3 & y_3 & \psi_3 \end{bmatrix}^T \tag{3.1}$$

With this coordinate system, we can now find the equations of motion that govern the bodies considering generalized ellipsoidal gravity potentials and tidal forces. The tidal force, as will be explained in the subsequent section, has the net effect of exerting a torque about the center of mass of each body while applying a commensurate change to in the orbital energy of the bodies. The easiest way to model the effect of ellipsoidal shapes and tidal torques on the motion of the bodies is to use a modification of the Euler-Lagrange equation. We begin by writing the general form of the equation with an augmented term to include the effect from the tidal torque:

$$\frac{d}{dt}\left(\frac{\partial L}{\partial \dot{\mathbf{q}}}\right) = \frac{\partial L}{\partial \mathbf{q}} - \mathbf{\Gamma}_q \tag{3.2}$$

where $L = T - U$, $\mathbf{\Gamma}_q$ is the sum of tidal torque terms, T is the total kinetic energy, and U is the total potential energy. The kinetic energy (T) of the three-body system can be calculated by adding the translational and rotational energy of each body.

$$T = \frac{1}{2}\sum_{n=1}^{3} M_n(\dot{x}_n^2 + \dot{y}_n^2 + \bar{I}_{n,z}\dot{\psi}_n^2) \tag{3.3}$$

where M_n is the mass of Body n, $\bar{I}_{n,z}$ is the mass normalized moment of inertia of Body n along the Z axis, and:

$$\bar{I}_n = \frac{1}{M_n}\begin{bmatrix} \frac{1}{5}M_n(b^2+c^2) & 0 & 0 \\ 0 & \frac{1}{5}M_n(a^2+c^2) & 0 \\ 0 & 0 & \frac{1}{5}M_n(a^2+b^2) \end{bmatrix}$$

$$\hat{\bar{I}}_n = trace(\bar{I}_n)$$

The total potential energy (U) of the three-body system is slightly more complex due to the ellipsoid-ellipsoid interaction between the bodies. The potential is a second-order expansion in the moments of inertia between two ellipsoidal bodies: [9]

$$U_{n,m} = -\frac{GM_nM_m}{r_{nm}}\Big\{1 + \frac{1}{2r_{nm}^2}\Big[\hat{\bar{I}}_n + \hat{\bar{I}}_m - \frac{3}{2}(\bar{I}_{n_x} + \bar{I}_{n_y} + \bar{I}_{m_x} + \bar{I}_{m_y} - \cos{(2\phi_{nm})}(\bar{I}_{n_y} - \bar{I}_{n_x}) - \cos{(2\phi_{mn})}(\bar{I}_{m_y} - \bar{I}_{m_x})\Big]\Big\} \tag{3.4}$$

For spherical bodies, $\bar{I}_{n_y} = \bar{I}_{n_x}$ and the potential energy between two bodies reduces to:

$$U_{n,m} = -\frac{GM_nM_m}{r_{nm}} \tag{3.5}$$

Finally, the total potential energy of the system is the sum of the mutual potential energies between body pairs:

$$U = U_{1,2} + U_{1,3} + U_{2,3} \tag{3.6}$$

The standard gravitational potential between two point masses appears at the beginning of this equation. The secondary terms account for the unsymmetrical distribution of mass along an ellipsoid. The potential is dependent on the angles ϕ_{nm}, ϕ_{mn}, which in general will not be equal. When the moment of inertia along each body axis is equal, as is for the case of a sphere, the secondary terms cancel out.

Now that the general framework of the problem has been setup, we will take the partial derivatives with respect to the state variables (x_n, y_n, ψ_n) to obtain the equations of motion for each body. The tidal torque term only appears in the expression for the partial derivative with respect to ψ_n.

$$x_n :$$

$$\begin{aligned}
\frac{d}{dt}\left(\frac{\partial L}{\partial \dot{x}_n}\right) &= \frac{\partial L}{\partial x_n} \\
\frac{1}{2}M_n(2\ddot{x}_n) &= -\frac{\partial U}{\partial x_n} \\
\ddot{x}_n &= -\frac{1}{M_n}\frac{\partial U}{\partial x_n}
\end{aligned}$$

$$y_n :$$

$$\begin{aligned}
\frac{d}{dt}\left(\frac{\partial L}{\partial \dot{y}_n}\right) &= \frac{\partial L}{\partial y_n} \\
\frac{1}{2}M_n(2\ddot{y}_n) &= -\frac{\partial U}{\partial y_n} \\
\ddot{y}_n &= -\frac{1}{M_n}\frac{\partial U}{\partial y_n}
\end{aligned}$$

Finally, we wish to track the evolution of the semi-major body axis (ψ_n). Here, the tidal torque terms are nonzero. There will be one tidal torque term for each of the two bodies exerting a tidal force on Body N.

$$\psi_n :$$

$$\begin{aligned}
\frac{d}{dt}\left(\frac{\partial L}{\partial \dot{\psi}_n}\right) &= \frac{\partial L}{\partial \psi_n} - \Gamma_{\phi_{nm}} - \Gamma_{\phi_{nk}} \\
M_n\bar{I}_n\ddot{\psi}_n &= -\left[\frac{3GM_n}{2}(\bar{I}_{ny} - \bar{I}_{nx})\left(\frac{M_m \sin 2\phi_{nm}}{r_{nm}^3} + \frac{M_k \sin 2\phi_{nk}}{r_{nk}^3}\right)\right] - \Gamma_{\phi_{nm}} - \Gamma_{\phi_{nk}} \\
\ddot{\psi}_n &= \frac{1}{M_n\bar{I}_n}\left(-\frac{\partial U}{\partial \psi_n} - \Gamma_{\phi_{nm}} - \Gamma_{\phi_{nk}}\right)
\end{aligned}$$

These equations of motion are integrated in order to propagate the motion of the bodies. There are two additional forces that factor into these body dynamics: tidal torques and contact forces. Each will be discussed in detail below.

3.2 Tidal Forces

Tidal torques arise between two bodies when there is a gravity gradient on the body. A gravity gradient arises for finite sized bodies because each infinitesimal mass unit throughout the body will feel a varying magnitude of gravitational acceleration inversely proportional to the distance squared from the mass unit to the center of mass of an attracting body. The gravity gradient serves to place mechanical stress on the interior structure of the body. Figure 3.2 demonstrates the accelerations a spherical 'Parent' asteroid would feel due to the gravity of a nearby spherical 'Child' asteroid.

To see how the body bulge forms, consider the forces acting on the Parent body in Figure 3.2. The tidal force $\vec{F}_{tidal}$ is the force that each infinitesimal mass element of the Parent body feels relative to the Parent body's center of mass:

$$\vec{F}_{tidal} = \vec{F}_g - < \vec{F}_g > \tag{3.7}$$

where $< \vec{F}_g >$ is the gravitational acceleration of the body's center of mass and $\vec{F}_g$ is the force felt by a single mass element of the body. Because the sides of the Parent body facing towards and away from the Child asteroid are respectively closer and further away from the Child, the particles along the closer and further surfaces will experience respectively a greater and smaller gravitational attraction, compared to the center of mass of the Parent body. Similarly, the poles of the Parent body will experience a net acceleration relative to the acceleration of the Parent body center of mass directed radially inwards. The net affect of these gravity gradients is a stretching of the Parent body along the axis connecting the centers of the Parent and the Child [10]. Similarly, the Parent body experiences a compressive deformation along its poles directed radially inwards. The elongated body axis is known as the body bulge. The amplitude of the body bulge depends on the mean rigidity of the asteroid $\bar{\mu}$ and is independent of the actual shape of the asteroid [3]. Thus both spherical and ellipsoidal bodies will develop a body bulge that will tend to undulate across the surface. To make this concept clear, consider the diurnal tides raised on Earth by the Moon. High tide is the observed body bulge of Earth, and this body bulge undulates across the oceans of Earth because of the dissimilar rotation rates of Earth and the Moon's orbit.

The Child asteroid will exert a force on the body bulge, which causes a torque about the Parent body center of mass, as depicted in Figure 3.3. This torque serves three main purposes: to dissipate excess energy in the system, to transfer angular momentum between asteroids, and to synchronize rotation rates of asteroids from a distance. [9]

In general, solving for an explicit net torque caused by these tidal forces is non-trivial. To explicitly solve for the tidal torque involves integrating the torque generated by the gravitational force of the Child body acting on each mass element of the Parent body, with a lever arm of $d\vec{r}$ extending from the center of mass of the

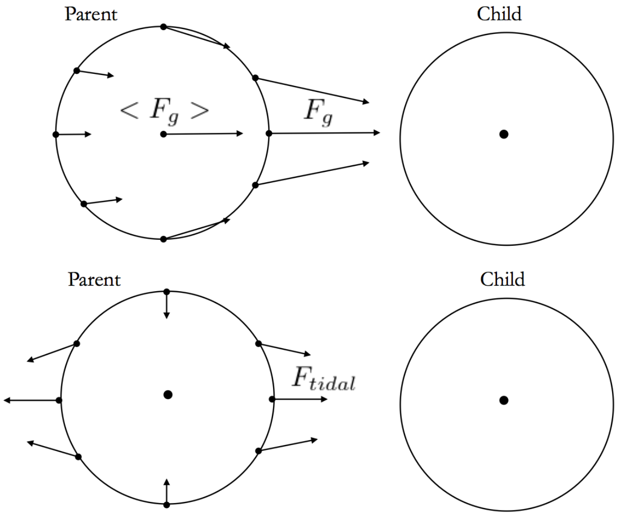

Figure 3.2: Gravity gradients cause stretching along a center of mass axis and compression along a perpendicular axis [9]. Relative to the center of mass of the Parent body, the side facing the Child body will experience a greater gravitational force towards the Child. The side facing away from the Child will experience a greater gravitational force away from the Child.

Parent body to the mass element.

$$\vec{\Gamma} = \int_{Vol} d\vec{r} \times \vec{F_g} \tag{3.8}$$

The magnitude of the gravitational force at each mass element also depends on the distance that the mass element is located away from the Parent body center

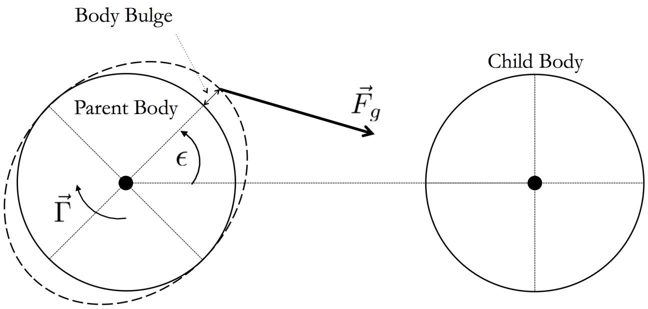

Figure 3.3: Gravitational forces will act on the body bulge and cause a net torque about a body.

of mass, thus $\vec{F}_g$ also depends on $d\vec{r}$. At present, we know of no explicit solution to this integral. The integral could be solved numerically at the cost of increased computation time. For the sake of simplicity, we employ an approximation commonly made by similar works to calculate the tidal torque a body would feel from a Child body [3]. The tidal torque used in this model is approximated to a first order from the classic tidal torque between two spherical bodies derived by Murray and Dermott [9]. Implicit in this approximation is the assumption that the distance between the two bodies is much greater than the diameter of the Parent body, which is certainly violated in the context of this paper, and is meant to be taken as a first order approximation for the true tidal torque. Γ_{ij} is the magnitude of the torque a spherical body j exerts on the tidal bulge of a spherical body i.

$$\Gamma_{ij} = sign(\dot{\phi_{ij}})\frac{3}{2}k_2\left(\frac{3}{4\pi\rho_i}\right)^2\frac{Gm_i^2m_j^2}{r_{ij}^6}\sin 2\epsilon_i \tag{3.9}$$

where $\dot{\phi}_{ij} = \dot{\psi}_i - \dot{\theta}_{ij}$, ϵ_i is the tidal lag angle of Body i, k_2 is the tidal Love number, and ρ_i is the density of Body i.

To find the total torque on a body due to tidal forces, we sum the individual torques exerted by the two orbiting bodies. The tidal lag angle ϵ physically represents the angle of the body bulge relative to $\vec{r}_{ij}$. The body bulge is independent of the body spin rate $\dot{\psi}_i$, and will undulate around the surface of the body. Tracking the body bulge angle necessitates modeling the time dependent deformation of the body due to tidal forces. We make the assumption that the shape of the body remains constant over the course of the simulation and furthermore, that the body bulge angle remains constant. The first assumption is justified because the asteroids we simulate are small and rigid enough that any physical body bulge would be negligible relative to the diameter of the body. The latter assumption is supported by considering the body bulge angle as a measure of the effectiveness for two bodies to tidally dissipate energy [9]. The body bulge angle ϵ is related to the specific tidal dissipation function Q by:

$$Q = \frac{1}{\tan 2\epsilon} \tag{3.10}$$

For comparison, $Q_{Earth} = 12$ and $Q_{Moon} = 27$ [11]. In general, Q must be estimated for each solar system body, although a typical value of 100 is used for small rocky bodies, which is used in this investigation. [12] The tidal Love number k_2 depends on the mean rigidity $\bar{\mu}$ of the body and has been estimated for a number of larger planetary bodies.

$$k_2 = \frac{3/2}{1 + \bar{\mu}} \tag{3.11}$$

Our current investigation uses an estimate for $k_2 = 10^{-5}$ taken from a paper by Jacobson that simulated asteroids of similar size and densities [3].

Finally, we finish our discussion of tidal torques by considering the resulting tidal force on the Child asteroid and the time rate of change of energy in the system. As was previously established, the Child asteroid will exert a torque about the spin axis of the Parent asteroid, causing the angular velocity of the Parent asteroid to increase or decrease. Equivalently, there is an equal and opposite torque exerted by the Parent asteroid onto the Child asteroid that changes its orbital speed. If the rotation rate of the Parent asteroid $\dot{\psi}$ is greater than the instantaneous orbital rate of the Child asteroid $\dot{\theta}$, the body bulge will be carried ahead of the Child. In this instance, the tidal torque Γ serves to decrease the rotational kinetic energy of the Parent asteroid at a rate $\Gamma\dot{\psi}$ while increasing the orbital energy of the Child asteroid at a rate $\Gamma\dot{\theta}$. Because $\dot{\psi} \neq \dot{\theta}$, the rates of work done by the tidal torque Γ are not equal and the total mechanical energy of the system, E will decrease at a rate [9]:

$$\dot{E} = -\Gamma(\dot{\psi} - \dot{\theta}), \text{ for } \dot{\psi} > \dot{\theta} \tag{3.12}$$

Conversely, if the rotation rate of the Parent asteroid is less than the instantaneous orbital rate of the Child asteroid, $\dot{\psi} < \dot{\theta}$, the tidal bulge will lag behind the orbit of the Child asteroid. In this case, the tidal torque Γ increases the rotational kinetic energy of the Parent asteroid at a rate $\Gamma\dot{\psi}$ while decreasing the orbital energy of the Child asteroid at a rate $\Gamma\dot{\theta}$. However, the total mechanical energy of the system will still decrease at a rate:

$$\dot{E} = \Gamma(\dot{\psi} - \dot{\theta}), \text{ for } \dot{\psi} < \dot{\theta} \tag{3.13}$$

The physical manifestation of this energy decay is escaping heat that is generated by material deformations within the body of the Parent asteroid. Modeling the internal structure of the asteroids and the friction generated by mechanical stress is complicated and beyond the scope of this study. For the sake of simplicity, we model this heat loss by applying a tidal torque to the Parent Asteroid and an equivalent tidal force to the Child asteroid. We already know that an external torque Γ will be applied to the rotational dynamics of the Parent asteroid so as to equalize its spin rate with the orbit of the Child asteroid. But the dynamical representation of the orbit raising/lowering tidal torque acting on the Child asteroid has yet to be determined.

We derive the dynamics of the orbiting raising/lowering tidal torque by equating the torque to a force acting about a lever arm. In this case, the lever arm is given by the vector $\vec{r}$ connecting the center of the Parent to that of the Child asteroid. The torquing force $\vec{F_\Gamma}$ is applied at the center of the Child asteroid and points in-plane, perpendicular to $\vec{r}$. From this relationship, we have a scaler equation that can be solved for the magnitude of $\vec{F_\Gamma}$:

$$\Gamma = \|\vec{F_\Gamma}\|\|\vec{r}\| \tag{3.14}$$

Or

$$\|\vec{F_\Gamma}\| = \frac{\Gamma}{\|\vec{r}\|} \tag{3.15}$$

This tidal force $\vec{F_\Gamma}$ is then incorporated into the linear dynamics of the Child asteroid:

$$\vec{a} = \frac{\sum \vec{F}_{gravity} + \vec{F_\Gamma}}{m} \tag{3.16}$$

The sign of Γ indicates whether the orbital energy, and thus orbitals speed of the Child asteroid, should increase ($\Gamma > 0$) or decrease ($\Gamma < 0$). As a matter of convention, we take the initial direction of the applied force so as to complete the right-hand set of $\vec{r}$ and the positive out-of-plane spin axis:

$$\hat{F}_{\perp} = +\hat{Z} \times \hat{r} \tag{3.17}$$

Where $Z = [0, 0, 1]^T$. The applied tidal force vector is:

$$\vec{F}_{\Gamma} = \frac{\Gamma}{\|\vec{r}\|} \hat{F}_{\perp} \tag{3.18}$$

For a system of 3 bodies, we assume that the effects of the tidal torque between body pairs can be added linearly. Thus the total dynamics for a body takes the form:

$$\vec{a}_n = \frac{1}{m} (\sum \vec{F}_{gravity} + \sum \vec{F}_{contact} + \sum \vec{F}_{\Gamma}) \tag{3.19}$$

$$\ddot{\psi}_n = \frac{1}{I_n} (\sum \tau_{ext} + \sum \Gamma) \tag{3.20}$$

Where $\vec{a}_n$ is the cartesian acceleration of Body n, $\ddot{\psi}_n$ is the angular acceleration of the Body n, $\vec{F}_{gravity}$ is the mutual gravitational force acting on Body n, $\vec{F}_{contact}$ is the sum of the soon to be discussed contact forces acting on Body n, and τ_{ext} is the gravitational torque exerted on Body n due to the gravitational acceleration from an ellipsoidal body. In our study, we consider only spherical bodies so $\tau_{ext} = 0$ for each body pair.

We conclude the section on tidal torques by proving that applying a torque Γ to the Parent asteroid and a tidal force $\vec{F}_{\Gamma}$ to the Child asteroid will always result in a net energy decrease. An applied torque Γ over some infinitesimal time dt will do some work δW_ψ to change the rotational energy of the system.

$$\delta W_\psi = -\Gamma\dot{\psi}dt \tag{3.21}$$

A positive Γ will slow the rotational energy of the Parent and conversely a negative Γ will increase the rotational energy. Now we shall compare this small work to the work done by applying the tidal force to the Child asteroid for the same infinitesimal time dt. A tidal force $\vec{F}_\Gamma$ acting on the Child asteroid for an infinitesimal time dt will do some work δW_s to change the orbital energy of the system.

$$\delta W_s = (\vec{F}_\Gamma \cdot \vec{v})dt \tag{3.22}$$

Where $\vec{v}$ is the velocity of the Child asteroid. Since $\vec{F}_\Gamma$ is perpendicular to $\vec{r}$, we are only concerned with the component of $\vec{v}$ that is along $\vec{F}_\Gamma$ - call this component $\vec{v}_\perp$. The instantaneous orbital rate of the Child asteroid $\dot{\theta}$ is related to $\vec{v}_\perp$ by:

$$\|\vec{v}_\perp\| = \dot{\theta}\|\vec{r}\| \tag{3.23}$$

Plugging this and the expression for $\vec{F}_\Gamma$ into the equation for δW_s and simplifying yields:

$$\delta W_s = \Gamma\dot{\theta}dt \tag{3.24}$$

Now we have simple expressions for the work done by the tidal torque Γ over some small time dt. By summing both works, we can see the net change in mechanical energy $\dot{E}$ of the system:

$$\dot{E} = \frac{dE}{dt} = \frac{\delta W_s + \delta W_\psi}{dt} = -\Gamma(\dot{\psi} - \dot{\theta}) \tag{3.25}$$

Thus $\dot{E}$ will always be negative because Γ and $\dot{\psi} - \dot{\theta}$ always carry the same sign. The net result is always a decrease in mechanical energy of the system. This notion of energy decay is very important because it drives the system towards a rotationally synchronized state. Given enough time, the system will eventually reach an equilibrium where $\dot{\psi} = \dot{\theta}$ for each pair of bodies, at which point the system is tidally locked.

3.3 Impulsive Collision Handling

When the surfaces of two bodies meet with some relative velocity, a collision is triggered and both bodies receive an impulsive change in their linear momentum before separating or forming a persistent contact. The goal is to calculate an impulse $\vec{J}$ such that the bodies move in a physically consistent manner and their surfaces do not penetrate. The change in linear velocity $\delta\vec{v}$ experienced by a colliding body is given by:

$$\delta\vec{v} = \frac{\vec{J}}{m} \tag{3.26}$$

$$\vec{J} = j\hat{n}(t_0) \tag{3.27}$$

where m is the mass of the body, j is the scalar impulse, and $\hat{n}(t_0)$ is the unit normal to the contact surface. If bodies A and B are colliding, then we define $\hat{n}(t_0)$ to point from the contact surface of Body B to Body A. For circular bodies, $\hat{n}(t_0)$ is simply:

$$\hat{n}(t_0) = \frac{\vec{r}_A - \vec{r}_B}{\|\vec{r}_A - \vec{r}_B\|} \tag{3.28}$$

With this notation, Body A will receive an impulse of $+j\hat{n}(t_0)$ while Body B receives an impulse of $-j\hat{n}(t_0)$. By looking at the symmetry of the applied impulse, it's easy to see that linear & angular momentum are conserved. To actually solve for the impulse term j, we first define the relative velocity between the two bodies at the contact point p before and after the collision. If $p_A = -R\hat{n}(t_0)$ is the vector from the center of Body A to the point of contact, then the velocity at contact point on A is

$$\dot{p}_A^- = \vec{v}_A^-(t_0) + \omega_A^- \times p_A \tag{3.29}$$

Where the superscripts (-) and (+) indicate quantities evaluated before and after the collision impulse is applied. The above equation is the same for the contact point on Body B, with $p_B = +R\hat{n}(t_0)$.

Now we can write the post collision velocity $\vec{v}_A^+$ in terms of the pre-collision velocity $\vec{v}_A^-$:

$$\vec{v}_A^+ = \vec{v}_A^- + \frac{j\hat{n}(t_0)}{m} \tag{3.30}$$

Then the relative velocity before the collision v_{rel}^- and after the collision v_{rel}^+ at the contact point can be calculated by:

$$v_{rel}^- = \hat{n}(t_0) \cdot (\dot{p}_A^- - \dot{p}_B^-) \tag{3.31}$$

$$v_{rel}^+ = \hat{n}(t_0) \cdot (\dot{p}_A^+ - \dot{p}_B^+) \tag{3.32}$$

Finally, we invoke the empirical law for frictionless collisions that allows for j to be explicitly solved for

$$v_{rel}^+ = -\epsilon v_{rel}^- \tag{3.33}$$

Where ϵ is the coefficient of restitution of the collision. A factor of $\epsilon = 1$ implies the bodies will bounce apart in a perfectly elastic collision and kinetic energy will be conserved. Any factor of $\epsilon < 1$ implies an inelastic collision between the bodies, resulting in a net loss of kinetic energy due to a supposed material deformation of the body. For our simulation, we take $\epsilon = 0$, which implies a perfectly inelastic collision between the bodies. This results in the bodies moving in tandem after the collision and a maximum loss of kinetic energy. Through this interaction, bodies can dissipate large amounts of excess mechanical energy in the system, shortening the time span for tidal torques to decay any remaining excess energy.

By combining the above equations (see paper for Baraff for reference [6]), we can arrive at an expression for j

$$j = \frac{-(1+\epsilon)\vec{v}_{rel}^{\,-}}{1/m_A + 1/m_B + \hat{n}(t_0) \cdot (\mathbf{I}_A^{-1}(p_A \times \hat{n}(t_0))) \times p_A + \hat{n}(t_0) \cdot (\mathbf{I}_B^{-1}(p_B \times \hat{n}(t_0))) \times p_B} \tag{3.34}$$

where $\mathbf{I}_i$ is the moment of inertia matrices for Body i, where $i = A$ or $i = B$. This is the general formula presented for any two rigid bodies in a collision. However, we are dealing with a much simpler case because the bodies in this simulation are considered spherical without Coulomb surface friction. Due to spherical symmetry, we note that for any collision $p_A \times \hat{n}(t_0) = 0$ and $p_B \times \hat{n}(t_0) = 0$ because the two vectors will always be parallel. Similarly, the angular component of the contact point velocity of Body i, $\omega_i^- \times p_i$ (for $i = A$ or $i = B$), will always be parallel with $\hat{n}(t_0)$ and will not appear in the v_{rel}^- and j equations. With these simplifications and the treatment of both bodies having identical mass and moment of inertia, the equation for the impulse scaler j reduces to

$$j = -\frac{m}{2}(\hat{n}(t_0) \cdot (\vec{v}_A^{\,-} - \vec{v}_B^{\,-})) \tag{3.35}$$

This is a fairly simple result because of the underlying geometric symmetry of the collision. With the impulse scalar determined, the velocities of each body post-collision are calculated

$$\vec{v}_A^+ = \vec{v}_A^- + \frac{j\hat{n}(t_0)}{m}$$
$$\vec{v}_B^+ = \vec{v}_B^- - \frac{j\hat{n}(t_0)}{m}$$

Applying this impulse allows the bodies to continue moving in a physically sensible manner and prevents their surfaces from immediately interpenetrating. In the general case for colliding rigid bodies, there will also be an impulsive change to the spin rate of each body that scales with j. Due to the symmetry of the bodies studied here, the angular momentum impulse evaluates to 0. This is the algorithm for handling collisions in the simulation. In the next section, we discuss the algorithm for handling bodies that form persistent contacts.

3.4 Persistent Contacts

In this simulation, the bodies are assumed to be rigid such that their surfaces do not deform. However, numerical interpenetration of bodies may occur for two reasons. The first is if two or more bodies form a persistent contact; that is, their physical surfaces are in contact, but they have zero or nearly zero relative velocity. Without the application of any contact force, the mutual gravitational force will pull the bodies closer causing a physical overlap of their surfaces. The second cause of a penetration arises from the the size of the time steps taken by the numerical integrator. Given a large enough time step, the physical surfaces of the bodies may overlap at the end of a timestep.

In practice, we will see that some small penetration is nearly impossible to avoid but the effects of violating this physical condition can be limited to within an acceptable tolerance. We explore two methods, the Fast Contact Force and Soft-Sphere Discrete Element Method (SSDEM), to calculate the persistent contact and interpenetration forces.

3.4.1 Fast Contact Forces

The first contact force model is a geometric approach that uses a rigorous physical formulation of the body geometry surrounding each contact point. The algorithm was formulated by Barraff and was originally developed for fast contact force computations in real-time physics engines like video games [7]. The method operates by examining the forces acting on each contact point and calculating a reaction force such that the gap d_i does not decrease.

When two or more bodies are in resting contact (zero relative velocity between their surfaces), gravity will pull the bodies closer and cause interpenetration. The rigid body assumption prevents interpenetration, which is accomplished by a reactionary normal force at the point of contact. In general, the distance between the surfaces of two bodies near a contact point is given by $d_i(t)$, shown in Figure 3.4. For $d_i(t) = 0$ the two bodies are in contact, $d_i(t) > 0$ the bodies have separated and $d_i(t) < 0$ the bodies have interpenetrated.

There is a simple relation between the contact points ($p_A(t)$ and $p_B(t)$) and contact distance ($d_i(t)$):

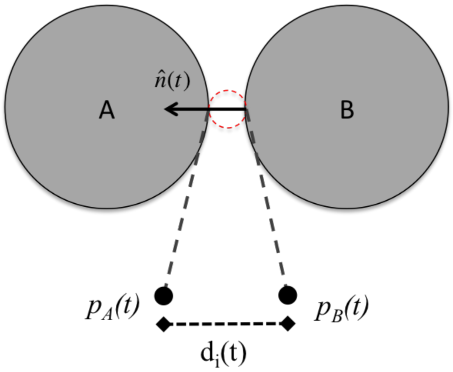

Figure 3.4: An infinitesimal gap d_i separates two bodies in contact, which must be guaranteed to increase or stay constant.

$$d_i(t) = \hat{n}_i \cdot (p_A(t) - p_B(t)) \tag{3.36}$$

Where $\hat{n}_i$ is the unit vector normal to surface of body B at the i^{th} contact point. At the current time $t_0, d_i(t_0) = 0, \dot{d}_i(t_0) = 0$, saying that the bodies are in direct contact initially with 0 relative velocity. The goal is to keep $d_i(t) \geq 0$ for all $t > t_0$.

This condition is ensured by maintaining that $\ddot{d}_i(t) \geq 0$, that is, the relative acceleration of the gap distance is either 0 (gap is held constant) or positive (gap increases and the bodies separate). The case of $\ddot{d}_i(t) < 0$ must be avoided, as this would cause the gap d_i to decrease and physical penetration would occur between the bodies. A further discussion of the Fast Contact Force model and derivations are listed in Appendix A.

We found through testing that the Fast Contact Force model tended to add energy to the system that would accumulate to a significant amount over long enough simulation durations. Coupled with an explicit integrator, the contact forces discussed in this section did a net positive work on the system. To understand why, we must first present the integration schemes used in the simulation and how this contact force model interacted with the integrator.

3.4.2 Soft-Sphere DEM Model

The second contact force model explored in this thesis is a soft-sphere distinct element method (SSDEM) model. The method was originally formulated for simulating granular mechanics problems, but has also been used to simulate small planetary bodies and rubble-pile asteroids [8]. A SSDEM model is useful for dense systems with persistent static contacts because it applies a restoring force that scales with the penetration distance of bodies. Physically, the SSDEM model treats interpenetration as a deformation of the body surfaces, but in our case of rigid bodies, we are using the restoring force as a correction term for bodies forming a persistent contact. Unlike with the Fast Contact Force method, the SSDEM model maintains an equilibrium point between bodies in persistent contact and stabilizes their energy and angular momentum over long durations. The latter point is essential for performing long duration simulations because all equilibrium configuration transitions include at least one persistent contact. Without the stabilizing restoring force of the SSDEM model, the energy and angular momentum of the numerical simulation can grow without bound until an artificial separation of bodies occurs. For these reasons, this thesis presents simulations results obtained using only the Soft-Sphere DEM model.

We will begin by describing the normal force between bodies in contact. The normal force is modeled as a linear, damped spring connected to the bodies along their contact normal.

The elastic force is given by:

$$\vec{f_e} = k_e \xi \hat{n} \tag{3.37}$$

and the damping force is simply:

$$\vec{f_d} = k_d \dot{\xi} \hat{n} \tag{3.38}$$

The total contact force is the sum of the elastic and damping force, $\vec{f_n} = \vec{f_e} + \vec{f_d}$. In the above equations, k_e is the elastic spring constant, ξ is the displacement from equilibrium (penetration distance), $\hat{n}$ is the unit normal direction joining the centers of the bodies in contact, k_d is the damping constant and is related to k_n, and $\dot{\xi}$ is the rate of penetration. For two bodies in contact, Body A and Body B of radius R with their locations specified at $\vec{r}_A$ and $\vec{r}_B$ respectively, we derive the variables used in equations 3.37 and 3.38:

$$\hat{n} = \frac{\vec{r}_A - \vec{r}_B}{\|\vec{r}_A - \vec{r}_B\|} \tag{3.39}$$

It can be shown that the relative velocity of the surfaces is as follows:

$$\vec{v}_{AB} = (\vec{v}_A + \dot{\psi}_A \times (-R\hat{n})) - (\vec{v}_B + \dot{\psi}_B \times (R\hat{n})) \tag{3.40}$$

The penetration distance and penetration speed can be defined as:

$$\xi = 2R - \|\vec{r}_A - \vec{r}_B\|$$

$$\dot{\xi} = \vec{v}_{AB} \cdot \hat{n}$$

The final step is to determine the values of k_e and k_d. The parameter of k_e is strongly dependent on the material properties of the bodies and their ability to deform. A good approximation for rigid bodies is to use their material strength as the elastic coefficient [8]. This assumption makes sense because a penetration would physically result in a deformation of the body and the tendency for the body to push against the deforming force. The mean rigidity is taken as $\bar{\mu} = 10^{13}\ kN/km^2$ assuming a carbonaceous asteroid [13] and so we take $k_e = 10^{13}\ kN/km^2$.

Calculating the damping coefficient k_d requires a deeper analysis of the harmonic motion of the spring-damper. The analytic solution for two spherical bodies A and B connected by a spring damper leads to expression for the restitution coefficient r:

$$r = e^{-\pi\eta/\omega} \tag{3.41}$$

Where,

$$\eta = k_d / m_{AB}$$

$$m_{AB} = m_A m_B / (m_A + m_B) = m/2$$

$$\omega = \sqrt{\omega_0^2 - \eta^2}$$

$$\omega_0^2 = k_e / m_{AB}$$

For an undamped oscillator, $k_d = 0$ and $r = 1$, the bodies will oscillate about their surfaces with constant magnitude. In our simulation, we want the oscillations to dampen quickly and for the bodies in persistent contact to remain as close as possible to each others surfaces while obeying the underlying physical constraint. For this reason, we ideally wanted a restitution coefficient of $r = 0$, implying the spring oscillator is critically damped and will not oscillate. To meet this condition requires that $\omega = 0$, and ultimately that $k_d = k_e$. For all of the simulations results presented, we take $k_d = k_e = 10^{13}\ kN/km^2$.

In practice, the bodies in contact will oscillate about some non-zero equilibrium point with some small oscillation frequency and magnitude. The reason is that the gravitational forces offset the equilibrium point of the damped spring oscillator to slightly below the surfaces of the bodies. When the bodies are perfectly in contact at each others surfaces ($\xi = 0$) with no relative movement ($\dot{\xi} = 0$), both the elastic force $\vec{f_e}$ and damper force $\vec{f_d}$ evaluate to 0. With no restoring normal force, the gravitational force will cause the bodies to interpenetrate after the next timestep. On the next step, there will be some penetration and a nonzero force $\vec{f_n}$ will pull the bodies apart. The result of this cyclical process is some small oscillation about the mean penetration distance. For stable contacts, the magnitude of these oscillations will eventually dampen to a negligible value and do not present any problems to stability of the energy and angular momentum for the system.

Finally, the total dynamics for a spherical body n is given by:

$$\vec{a}_n = \frac{1}{m}(\sum \vec{F}_{gravity} + \sum \vec{F}_{contact} + \sum \vec{F}_{\Gamma}) \tag{3.42}$$

where $\sum \vec{F}_{gravity}$ is the sum of the gravitational forces acting on body n, $\sum \vec{F}_{contact}$ is the sum of the contact forces $\vec{f}_e$ and $\vec{f}_d$ acting on body n, and $\sum \vec{F}_{\Gamma}$ is the sum of the tidal forces acting on body n.

Chapter 4: Methodology

In this chapter, we discuss how the simulation operates and applies the dynamics formulated in the previous sections. The simulation consists of: a dynamics function to calculate the gravitational, tidal, and contact forces acting on the bodies; a numerical integrator to propagate the dynamics of the system forwards in time; and an adaptive ordinary differential equation (ODE) solver to condition the accuracy of the propagation. The code is written in MATLAB. The position, velocity, and bulk properties of each body are stored in a structure variable type, which gets passed between various functions. We tested and compared the efficacy of two integrator schemes: an explicit Runge-Kutta 4(5) integrator and a symplectic Velocity Verlet integrator.

The simulation consists of three overarching functions that handle the bulk of calculations.

- **mainPropagator**: The outer-most and first called function which contains the governing logic for how the simulation proceeds. This function takes in a structure containing the initial state variables of the three bodies and simulation parameters like initial step size, error tolerance, and simulation end time. The function will advance the state of the bodies until the specified end time is reached. The output is an array of state variables at each timestep that can be later processed for data visualization. Collision and contact events are handled here. The function determines if the attempted propagation was successful and selects a new timestep to try for the next iteration.

- **mainIntegrate**: This function is called inside of 'mainPropagtor' and applies the chosen integration scheme to advance the state of the system. The function takes as input the state variables of the system at the current simulation time and outputs the state of the system advanced by the timestep h. Contact conditions are assumed to be constant over an integration step so that consistent dynamics are applied throughout.

- **calcForces**: This function calculates the linear and angular accelerations for each body based on the model dynamics described in Chapter 3. The function is called from within 'mainIntegrate', often more than once, to return the instantaneous accelerations and velocities of the bodies used to advance the state of the system. It takes as inputs a set of state variables and a contact condition matrix. The function outputs the linear and angular accelerations, which get converted to velocities, and the velocities of each body, which get converted to linear and angular positions.

4.1 Simulation Logic

In this section, we detail the order of events for each timestep of the simulation which occur in the function 'mainPropagator'. The overall logic of the simulation is largely independent of the specific numerical integrator and contact force model used. As such, different integration schemes can be easily tested with little or no modification to the core code of the simulation.

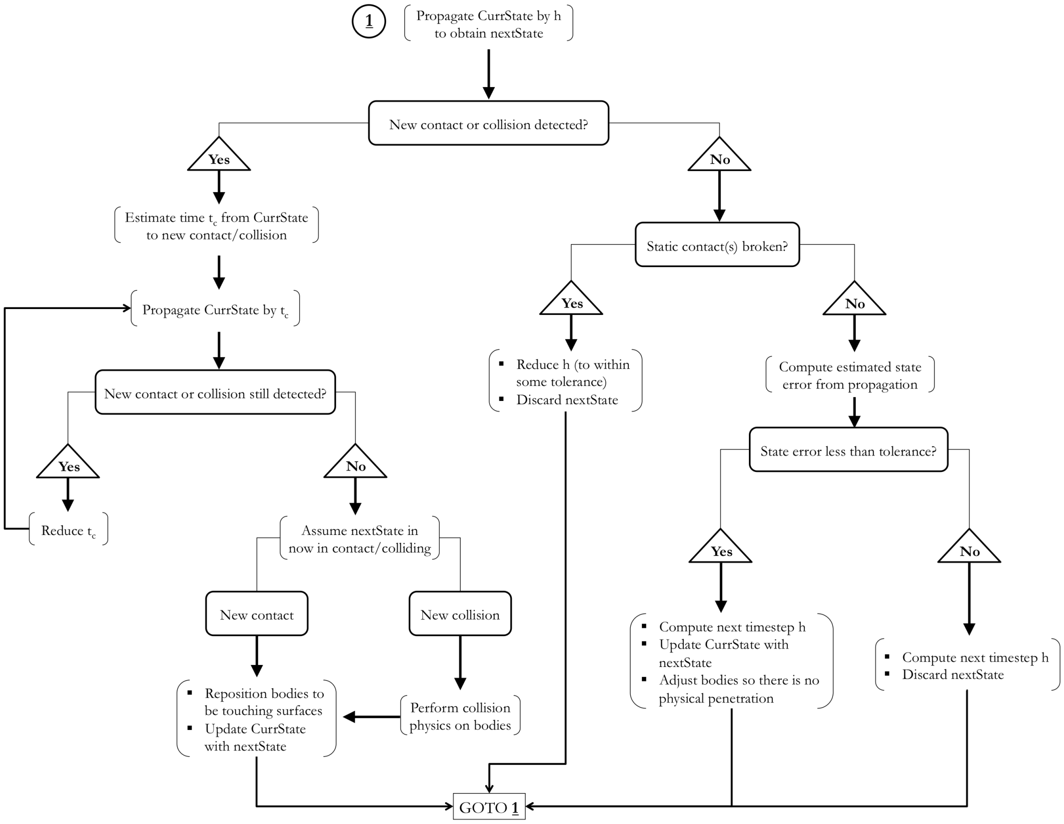

Figure 4.1: Logic tree algorithm 1 used with the Runge-Kutta adaptive step method.

The initial positions, velocities, and bulk properties of the bodies, as well as simulation parameters like the initial timestep h_0, simulation end-time, and convergence tolerance ϵ are set by the user. The simulation will attempt to propagate the dynamics of the bodies by the initial timestep. If the simulation is set to run as fixed timestep, then the initial timestep will be used for all subsequent propagations of the system. If the simulation is set to run with a variable timestep, then the specified error tolerance ϵ will be compared against the estimated state error Δ

produced by integration scheme. If the estimated state error Δ is greater than the maximum allowed error ϵ, the propagator will choose a smaller time step and retry. If $\Delta < \epsilon$, then the propagator will continue with the next step and calculate a larger timestep such that $\Delta \approx \epsilon$ on the next timestep.

There are two different strategies employed to propagate the dynamics of the bodies that stem from how the estimated state error Δ is calculated. The first algorithm, labeled here as the "Adaptive Step Method", uses the known order of the integrator to estimate the state error and requires only a single propagation for each successful timestep. For the Adaptive Step Method, we consider a Runge-Kutta integration scheme.

The second algorithm, labeled here as the "Half-Step Method," computes two propagated states to estimate the state error and requires three separate propagations in order to advance by one step. The idea behind the Half-step method is to propagate the system twice using timesteps of $h/2$, then repropagate the system using a timestep of h, and then compare the two final states. If the difference between the final states are within the specified error tolerance ϵ, then we can increase the next step size since propagating by h yields about the same result as propagating twice by $h/2$. In both cases, the propagator function takes in the structure variable of the current system state (called 'CurrState'), advances the system by a timestep h, and outputs a structure containing an estimate of the new state of the system (called 'nextState'). The operational differences between the two methods are visually captured in the following logic tree diagrams.

The important distinction between the two methods is how the state error is

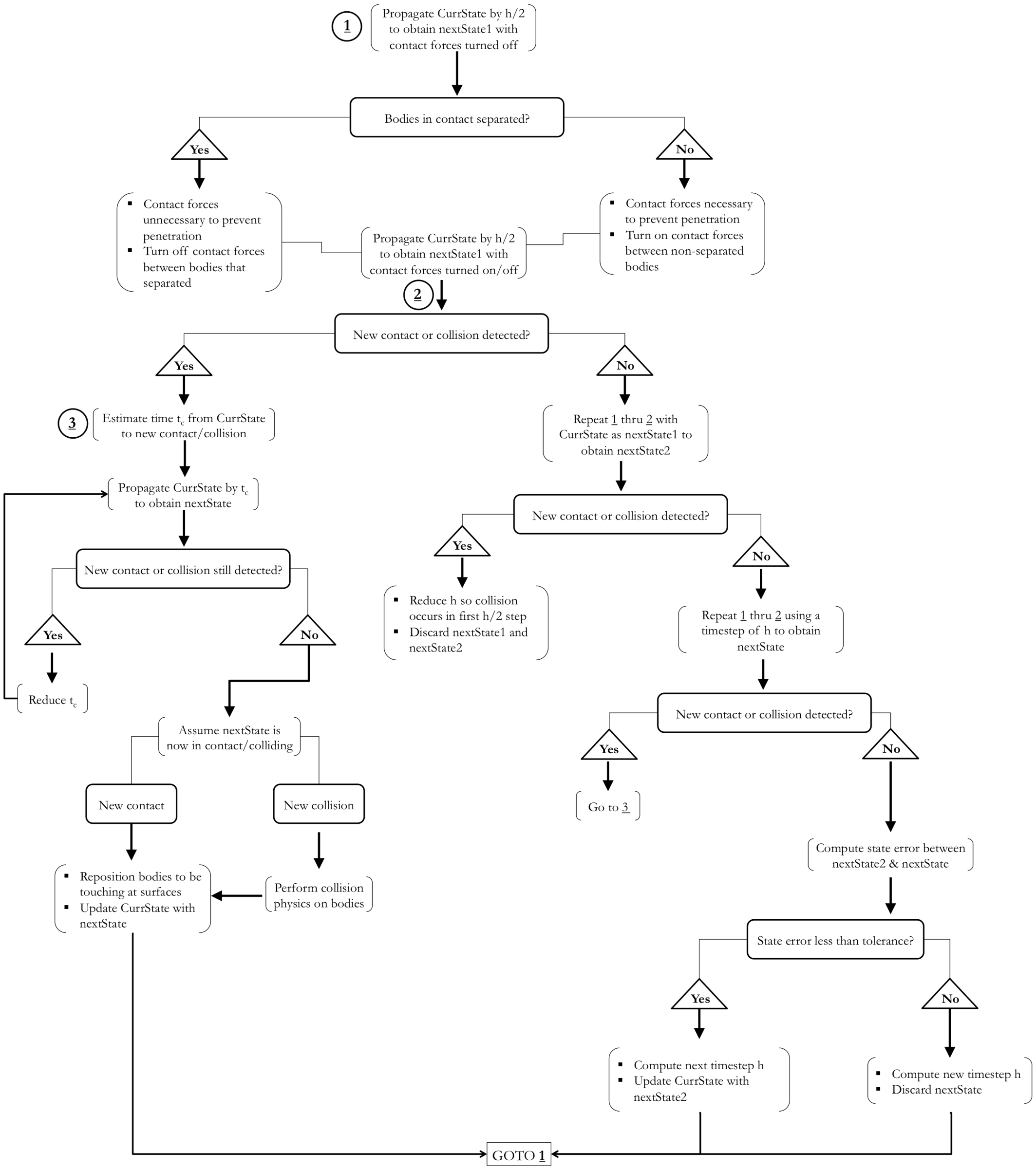

Figure 4.2: Logic tree algorithm 2 used with the Half-step method.

estimated. Other than that quality, the methods use the same logic and routines for handling contacts, collisions, and separation events.

4.2 Numerical Integrator

All numerical integrators have a set of assumptions used to approximate the true solutions of the underlying system dynamics. While all numerical propagators provide us with approximate knowledge of the solution, some are better suited for certain types of dynamical systems. A system is said to be numerically stiff if the dynamics are prone to sudden changes within a small interval of convergence [14]. Even though a stiff system may be sufficiently smooth and stable around its equilibrium points, the dynamics change so rapidly that numerical integrators must use increasingly smaller step sizes to correctly converge to the true solution. If too large a step size is taken, the approximate solution may become numerically unstable and grow towards infinity.

Take the basic stiff equation, $y'(t) = -\lambda y(t), y(0) = 1, \lambda > 0$, for which the analytic solution is $y(t) = e^{-\lambda t}$. For $t > 0$, the solution $y(t)$ quickly converges to 0. However, let's see what happens when a simple first-order Euler's method is implemented to approximate the first two seconds of the solution to $y'(t)$ using a step of $h = 1$ and $\lambda = 10$.

$$y'(0) = -10y(0) = -10$$

$$y(1) = y(0) + hy'(0)$$

$$y(1) = 1 + 1(-10) = -9$$

$$y'(1) = -10y(1) = -10(-9) = 90$$

$$y(2) = y(1) + hy'(1)$$

$$y(2) = -9 + 1(90) = 81$$

Comparing the results to the true values, $y_{true}(1) = e^{-10 \cdot 1} \approx 4.54(10^{-5})$ & $y_{true}(2) = e^{-10 \cdot 2} \approx 2.06(10^{-9})$, we see that the numerical results produced by Euler's Method are wildly inaccurate. And if we let this numerical propagator continue, instead of the solution stabilizing and converging to 0 as it should, it will oscillate between increasingly larger values as it diverges to $\pm\infty$. So in addition to not approximating the solution to the stiff differential equation, our choice of Euler's Method integrator led to numerical instability of the solution. However, if the step size was reduced to say $h = 0.1$, then the first-order Euler's Method integrator would produce a stable solution to the differential equation that oscillates around the equilibrium point of $y = 0$ (although the numerical solution will never converge to 0). Depending on the system that we are simulating, an oscillating numerical solution, even if stable, may not be desirable.

Contact forces, which are an integral part of the simulation for keeping bodies from physically penetrating, are an example of stiff model dynamics. Contact forces are especially difficult to simulate because in addition to being dynamically rigid, they are also non-smooth. Two bodies separated by an infinitesimal gap are only subject to gravitational and tidal forces, but the moment their surfaces touch, there is a discontinuous change to their governing dynamics. In this scenario, collision physics would dictate the energy lost in this encounter and bring the relative velocity of the bodies to 0. Now consider the dynamics of two bodies in a stable persistent contact. As the body dynamics are propagated forward in time, the applied contact forces will attempt to maintain a fixed relative distance between the centers of the bodies. In practice, maintaining this fixed distance with any numerical integration scheme is nearly impossible and every state is prone to some numerical inaccuracies. After every time step, the bodies will either penetrate by some small amount or separate by some other small amount. As will be empirically shown, both cases can lead to numerical instability of the system even though the bodies are at an equilibrium. We tested two contact force models and three numerical propagators with the simulation. We found that an explicit velocity verlet integration scheme and a soft-sphere DEM contact force model worked the best and produced long-term stable results with small errors in conserved quantities.

4.2.1 Runge-Kutta 4(5) Method

We have implemented and tested two different integrators, an explicit Runge-Kutta integrator and a symplectic integrator. The explicit Runge-Kutta integrator is the based on the Dormand-Prince (RKDP) method, the same explicit integrator used by the MATLAB function ode45. This method produces fourth-order and fifth-order accurate solutions in order to generate a state estimate with error $O(h^5)$. The state estimates are based on the following formulation and Butcher Tableau [15], where y_n is the state vector of the system at time t_n and $f()$ is the function that computes the forces on each body.

$$\begin{aligned}
&y_{n+1} = y_n + h\sum_{i=1}^{7} b_i k_i = \text{ fifth-order accurate solution at time } t_{n+1}\\
&\hat{y}_{n+1} = y_n + h\sum_{i=1}^{7} \hat{b}_i k_i = \text{ fourth-order accurate solution at time } t_{n+1}\\
&k_1 = f(t_n, y_n)\\
&k_i = f(t_n + c_i h, y_n + h\sum_{j=1}^{6} a_{ij} k_j)\\
&e_{n+1} = y_{n+1} - \hat{y}_{n+1} = h\sum_{i=1}^{7}(b_i - \hat{b}_i)k_i = \text{ state error estimate of order } O(h^5)
\end{aligned}$$

The next state estimate y_{n+1} gets output to the propagator in order to update the state of the system and check for collision/separation events. If the Runge-Kutta adaptive step method is used, then the k_i terms are used to calculate the estimated state error. If the Half-step method is used, the error estimate comes from comparing y_{n+1} for two separate propagations using a timestep of h and $h/2$.

$$\begin{aligned}
&y_{n+\frac{1}{2}}(t_n + \frac{h}{2}) = y_n + \frac{h}{2}\sum_{i=1}^{7} b_i k_i\\
&y_{n+1}(t_n + h) = y_{n+\frac{1}{2}} + \frac{h}{2}\sum_{i=1}^{7} b_i k_i\\
&\bar{y}_{n+1}(t_n + h) = y_n + h\sum_{i=1}^{7} b_i k_i\\
&e_{n+1} = y_{n+1} - \bar{y}_{n+1}
\end{aligned}$$

The largest error amongst the different state variables of e_{n+1}, that is $max(e_{n+1}) = \Delta$, is used to determine the subsequent timestep and whether the propagation is considered successful. The max error Δ is compared to the convergence tolerance ϵ at the beginning of the simulation. If the error is less than the acceptable error tolerance, the propagation is considered successful and the timestep is increased. Similarly, if the error is greater than the tolerance, the propagation must be redone with a smaller timestep. In either case, the timestep is changed predicatively so that the error of the next propagation is very close to the acceptable tolerance. This approach reduces computation time by jumping to the largest such timestep that will produce a successful propagation [15]. Based on the maximum state error Δ, the next timestep to try h_{n+1} is given by:

$$h_{n+1} = 0.9 h_n \left[\frac{\epsilon}{\Delta} \right]^{\frac{1}{p+1}} \tag{4.1}$$

Where $p = 5$ is the order of the numerical integrator.

4.2.1.1 Choice of Contact Force Model and Integration Scheme

The simulation was originally tested using the Fast Contact Force model and the Runge-Kutta 4(5) integration scheme. Both methods were eventually discarded after it was experimentally found to add unbounded energy and angular momentum to the system for bodies in persistent contact. The reason for the unbounded errors has to do the way the contact forces interacted with the integrator.

The calculated contact force $\vec{F}_{contact}$ is only valid for the current state of the

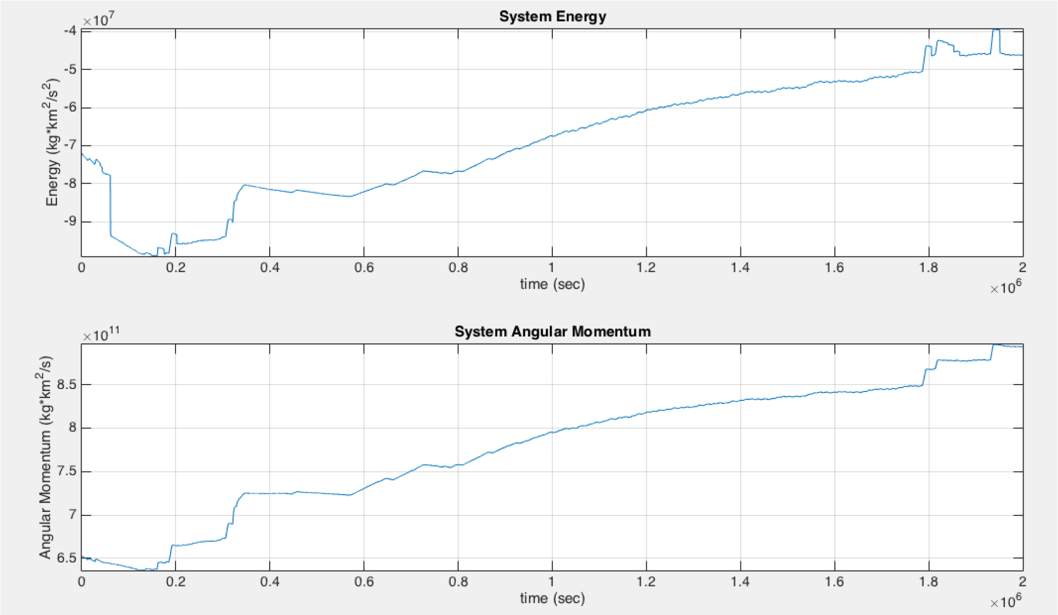

Figure 4.3: Energy and angular momentum for the transition from LR to ER using Fast Contact Force model and a Runge-Kutta 4(5) integrator over 2 million seconds.

system at the current time. During the course of the RK integration, several intermediate states are obtained and then averaged together, each with their own specific contact force based on the position and velocity of the bodies at that intermediate time. The contact forces, when averaged together, are not exactly perpendicular to the movement of the bodies. Work done by a force is given by $\delta W = \vec{F} \cdot d\vec{r}$, and because $\vec{F}_{contact}$ and the displacement $d\vec{r}$ of the bodies are not perpendicular, the contact forces inevitably did work on the system.

Without any stabilizing forces, like the spring-damper force of the SSDEM contact force model, the contact forces would continue to add energy to the system as long as bodies were in a persistent contact. Figure 4.3 show the significant effect of the contact forces on the total energy and angular momentum for the Lagrange Resting to Euler Resting transition.

After 2,000,000 seconds, the contact forces have produced a total error in the system energy $O(10^7)$ which is the same order of magnitude as the total energy of the system. Similarly, the error in angular momentum is on the same order as the total angular momentum for the system. Clearly, using these methods for handling persistent contacts and propagating motion of the bodies will not suffice. Instead, we use the soft-sphere DEM contact force model along with the Velocity Verlet integration scheme to obtain the final results presented at the end of this paper.

4.2.2 Velocity Verlet Method

The second integrator tested is a mid-step Velocity Verlet method, which is a second-order symplectic integrator. The integration scheme is split into two steps which propagate the position and velocity of each body in separate steps. Propagating the bodies in this manner preserves the phase space area of the system. For a Hamiltonian system, preserving phase space area is equivalent to conserving the wedge product of the change in position and change in momentum of the system, $dp \wedge dq$. Intuitively, the phase space is visually represented by a 2D graph with the position and momentum on the X and Y axis, respectively. If the position and momentum of each body were plotted in this phase space graph, one could connect the points to define a shape. The area of that shape is the phase space area, and a symplectic integrator preserves the total area of the shape as the system is advanced forward (or backwards) in time. Propagating the system by a single time-step will distort the shape of the area but the total area will remain the same. The change in shape is equivalent to some small change in the total energy of the system, so on an individual timestep basis, energy is not conserved. But for any Hamiltonian system exhibiting harmonic oscillations, a symplectic integrator ensures that the shape of the deformed phase space area will eventually return to its original configuration [16]. Stated differently, a symplectic integrator will not conserve energy at each propagation step but the total energy will oscillate about its original value over large durations. In this way, the total change in energy of the system is bounded. Non-symplectic integrators, like Runge-Kutta 4(5), do not conserve the phase space area and cause energy errors to diverge exponentially [15]. For these long-term energy bounding properties, symplectic integrators are widely used in simulations of astrodynamical and molecular systems [8] [17] [18].

The steps of the mid-step velocity verlet integrator are relatively simple. We begin by calculating the half-step velocity $\vec{v}_{\frac{1}{2}}$ after a timestep h/2 using the current position $\vec{r}(t)$ and velocity $\vec{v}(t)$:

$$\vec{v}_{\frac{1}{2}}(t + h/2) = \vec{v}(t) + \frac{h}{2}\vec{a}(\vec{r}(t)) \tag{4.2}$$

The acceleration $\vec{a}$ is assumed to be a function of only the positions of the bodies. The half-step velocity $\vec{v}_{\frac{1}{2}}$ can be thought of as the average velocity the body after a full time step h. The next position is calculated using the half-step velocity. This physically makes sense because as position crosses the interval from $\vec{r}(t)$ to $\vec{r}(t + h)$, the velocity in the middle of the interval best represents the approximate speed during this time.

$$\vec{r}(t+h) = \vec{r}(t) + h\vec{v}_{\frac{1}{2}} \tag{4.3}$$

From these equations, we have that the next position is only dependent on the current state variables of the body. The next step of the propagation is to calculate the next velocity of the body $\vec{v}(t+h)$ using the updated position of the body $\vec{r}(t+h)$:

$$\vec{v}(t+h) = \vec{v}_{\frac{1}{2}} + \frac{h}{2}\vec{a}(\vec{r}(t+h)) \tag{4.4}$$

Again if we look at what is physically happening with these equations, we see that the average acceleration is used to calculate the next velocity. The velocity crosses the interval from $\vec{v}(t)$ to $\vec{v}(t+h)$ using half of the initial acceleration plus half of the final acceleration.

The magnitude of the errors of this integrator is of order $O(h^2)$. Note that the formulation of this integrator assumed that the acceleration $\vec{a}$ was only a function of position $\vec{r}$. For our simulation, this assumption is satisfied when all three bodies are separated from each other. However, when two or more bodies are in contact, a velocity-dependent spring-damper force is introduced into the system. The acceleration would thus depend on both the position and velocity of the bodies. Similar simulations in granular mechanics have used spring-damper contact forces in tangent with a velocity verlet integration scheme [8]. We will eventually show that this condition violation does not significantly affect the energy and angular momentum conserving properties of the Velocity Verlet integration scheme.

When the system is in a state of equilibrium, the damper-force will evaluate to

0. When the system is still dynamically evolving, the damper will dissipate energy that is introduced by the propagator in the short-term that would otherwise cause the bodies to cyclically penetrate and separate. We can assert this because after a collision, the relative velocity between bodies is zeroed out and their surfaces will be pulled in by gravity. Once the bodies remain in long-duration, persistent contacts, an equilibrium of penetration distance is reached and the damper force quickly converges to 0. We will also show this reasoning to be experimentally true from the results of the simulation. Although a tenant of the velocity verlet integrator is violated, we have found that this integration scheme was the best at conserving energy on transient and long-duration scales compared to the other integrators tested.

Unlike the Runge-Kutta 4(5) method, the velocity verlet integrator is nominally configured to operate using fixed step sizes. To overcome this limitation, we use the Half-Step method in conjunction with the velocity verlet integrator to allow for variable step sizes. We compute an appropriate step size after each iteration by performing two separate propagations using different step sizes and comparing their differences.

1. Propagate CurrState by h/2: nextState1 = mainIntegrate(CurrState, h/2)
2. Propagate nextState1 by h/2: nextState2 = mainIntegrate(nextState1, h/2)
    - nextState2 should represent the state of the system at time $t + h$
3. Propagate CurrState by h: nextState = mainIntegrate(CurrState, h)
    - nextState should represent the state of the system at time $t + h$

4. Compute the maximum magnitude of the errors between the two final states

    - $\Delta = |nextState2 - nextState|_{max}$

If the maximum difference between the two states is greater than the user defined error tolerance ($\Delta > \epsilon$), then the step size h was too large and must be decreased because propagating by $h/2$ must not be equivalent (to within a tolerance) to propagating by a full h. The latest propagated state is discarded and the last state is propagated again using a small step size. Conversely, if $\Delta < \epsilon$, then the propagation is valid and we can advance the state of the system; however the step size used is too small and can be made larger to make the simulation run faster. In either case, the new step size h_1 will be scaled by the old step size h_0 as follows [19]:

$$h_1 = h_0(\epsilon/\Delta)^{1/p} \tag{4.5}$$

Where $p = 2$ is the order of the error for the integrator. However, we are cautious about the event of a small error term Δ producing a large increase in the next step size, which can lead to missed collisions and may cause the bodies to behave inaccurately. This can also lead to simulation constantly oscillating between small and large time steps which ultimately increases computation time. So instead we choose a more conservative method for calculating the next step size. that is slower to grow but allows for the simulation to smoothly converge upon the most efficient timestep:

$$h_{n+1} = 0.9 h_n \left(\frac{\epsilon}{\Delta} \right)^{0.1} \tag{4.6}$$

4.3 Test Configuration Initialization

For each of the seven possible initial equilibria configurations, the initial positions and velocities between bodies are determined by a normalized value of angular momentum $\bar{H}^2$. First, the positions of the bodies are adjusted so that the barycenter is at the origin of the coordinate system. Then the initial translational and angular velocities are calculated such that all the bodies are tidally locked, meaning that the bodies orbit about the barycenter and spin about their body axis at the same rate ($\dot{\theta} = \dot{\psi} = \omega$). This common rate ω can be calculated for any H (provided some $\bar{H}^2$) by considering the moment of inertia of the system rotating around the barycenter and the body axis spin.

$$\omega = \frac{H}{3I + M(|\vec{r}_1|^2 + |\vec{r}_2|^2 + |\vec{r}_3|^2)} \tag{4.7}$$

where $I = \frac{2}{5} M (d/2)^2$.

For rotations about an axis perpendicular to the plane of motion, which is the case we have examined, the initial spin rate of Body i is simply:

$$\vec{\omega}_i = [0, 0, \omega]^T \tag{4.8}$$

Each of the three bodies will be initialized with this same rotation vector $\vec{\omega}_i$.

We calculate the initial velocity of Body i such that Body i will rotate about the barycenter at a rate equal to ω. The required tangential velocity of Body i is thus:

$$v_i = \omega|\vec{r}_i| \tag{4.9}$$

The direction of v_i is tangent to the position vector of Body i and the body spin axis $\vec{\omega}_i$. Thus initial velocity vector of Body i such that the bodies are tidally locked is given by:

$$\vec{v}_i = v_i\left(\frac{\vec{\omega}_i \times \vec{r}_i}{|\vec{\omega}_i \times \vec{r}_i|}\right) \tag{4.10}$$

4.3.1 Canonical Units

The introduction of canonical units into the system offers a number of attractive computational advantages. Using SI units or another base for modeling celestial systems can lead to greater numerical inaccuracies due to the finite precision of a computer. The mass of solar system bodies are typically on the order of $> 10^{13}$ kg. Compare this magnitude to that of the gravitational constant G (10^{-20}) $km^3/(kg \cdot s^2)$ and the orbital velocity of bodies 10^1 km/s. Unless special caution is paid to preserving the trailing digits when multiplying these numbers together, the large difference in their magnitudes will result in a loss of numerical accuracy. Switching the base units of the simulation to canonical units reduces the affect of finite numerical precision and inaccuracies by rescaling the commonly used variables to be on or close to the same order of magnitude.

We define the canonical distance unit DU to be equal to the radius of the bodies, where r is the radius of the body in SI units.

$$DU = r \tag{4.11}$$

The canonical mass unit MU is taken to be the mass of each body.

$$MU = m \tag{4.12}$$

Finally, we wish to rescale the canonical time unit TU such that the gravitational constant $G = 1$. In SI units, we have the gravitational constant is $G_0 = 6.67 \times 10^{-20} \frac{km^3}{kg \cdot s^2}$. Thru basic unit conversion, we arrive at the equation for TU:

$$G = 1 = G_0 \frac{km^3}{kg \cdot s^2} \cdot \left(\frac{MU[kg]}{1[MU]}\right)\left(\frac{1[DU]}{DU[km]}\right)^3\left(\frac{TU[s]}{1[TU]}\right)^2 \tag{4.13}$$

Solving for the time unit TU yields:

$$TU = \sqrt{\frac{DU^3}{G_0 MU}} \tag{4.14}$$

Expressing the physical properties in these canonical units reduces their overall magnitude and makes many of the computations trivial (like multiplying by G or squaring the radius R). The time unit TU will essentially "absorb" the differences in scale of the other parameters, which might initially seem problematic because in general, TU will be 3-4 orders of magnitudes larger than the other canonical units. However, TU is only used in a scalar multiplication of the velocity and acceleration terms a few times per propagation. This limits the total amount of calculations performed per timestep that involve very large and very small numbers, thereby reducing the total numerical rounding error by the machine. In experimental test case, we found that while the difference in accuracy was marginal, the overall computation time using canonical units compared to SI units was anywhere from 15-35% faster. The results presented all use canonical units during the simulation and were later reconverted back to SI units for post processing.

Chapter 5: Simulation Results

The simulation results we obtained support and validate the hypothesized transitions between the three minimum energy configurations. The scenarios we chose to test are those that begin in a configuration that was stable prior to an angular momentum increase or decrease (see Figure 2.3). Each case presented here was simulated using the Velocity Verlet integrator, the Soft Sphere DEM contact force model, and the Half-Step variable timestep propagation method.

Overall, we found that systems transitioned to the analytically predicted minimum energy configuration within a short amount of time relative to overall duration of the simulation. The majority of collisions subsided after 100,000 seconds. The largest deviation in total energy and angular momentum, ignoring collision and dissipative effects, did not exceed 1 part in 10^8. Furthermore, total energy and angular momentum, again ignoring any modeled energy losses, reached a steady state over long enough durations, suggesting that total energy and angular momentum errors are bounded.

We will discuss the results of the simulation broken down into three sections:

- Validation of the simulation code through comparison with well known solar system bodies. We must first prove that the simulation is capable of producing results that are in agreement with the orbits of well documented celestial objects, like the Sun-Earth-Moon system.

- Capability of the simulation to handle stable, persistent contact cases. We will prove the fidelity of the code to handle static contacts and maintain a minimum equilibrium configuration before attempting a more complicated case.
- Simulation results for the transitions between minimum energy configurations. We will discuss and apply several metrics to justify that the hypothesized minimum energy configuration transitions are validated by these results. Finally, the limitations and known errors of the simulation results will be discussed, with a greater detail being given in the Error Analysis section.

5.1 Validation of Simulation

Before a discussion of the primary thesis results, we begin by establishing the accuracy of the simulation in modeling the physical behavior of gravitationally attracting bodies. For this test, we only model the gravitational forces acting between bodies and do not consider the effects of tidal torques or contact forces. The easiest and certainly most well known physical system to compare to our simulation results in this limited scenario is the Sun-Earth-Moon system. None of these bodies are in direct contact and tidal torques do not significantly affect the orbits of the bodies over the simulation duration. We will show that our simulation accurately calculates the orbital trajectory of the Sun-Earth-Moon system to within an allowable tolerance.

The three bodies of the simulation, representing the Sun, Earth, and Moon, were initialized using position and velocity data from the JPL HORIZONS system at an arbitrary start date [20]. Similarly, the mass of each body was obtained through the HORIZONS system. The system was propagated for four complete orbits (4×365 days) using a fixed timestep of $h = 80$ seconds.

In this idealized system, energy and angular momentum are notionally conserved. We can see in Figure 5.1 that the total energy and angular momentum are conserved to within 1 part in 10^{13}. Additionally, the acceleration of each body is solely dependent on the positions of the bodies, so the Velocity Verlet integrator should cause these quantities to oscillate about the original energy of the system. Indeed, we see a somewhat cyclic fluctuation in energy and angular momentum that is bounded because of the nature of the symplectic integrators.

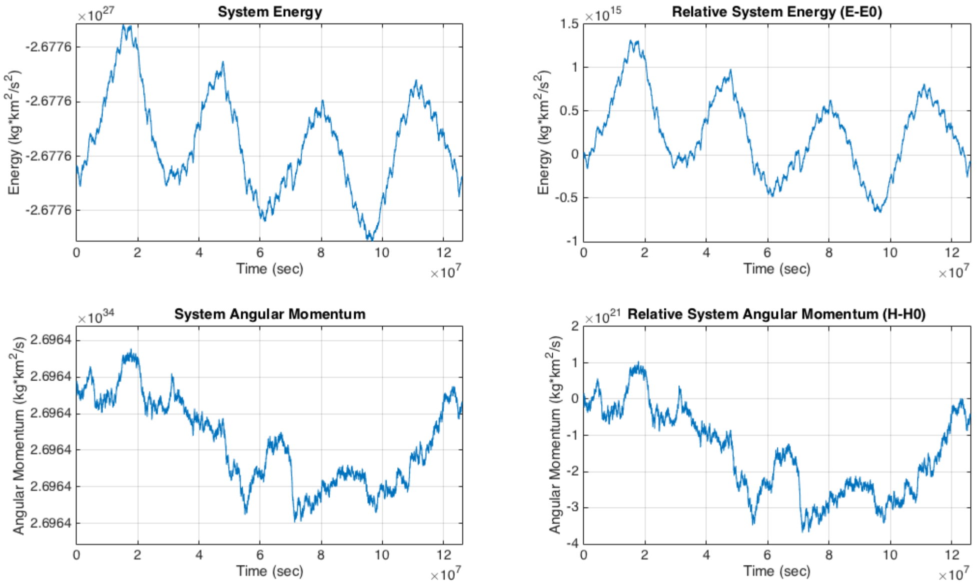

Figure 5.1: Energy and angular momentum for the Sun-Earth-Moon system. Relative energy and angular momentum on the right are with respect to the initial values of the system.

We conclude that the simulation accurately simulates the motion of the Sun-Earth-Moon and conserves the total energy and angular momentum of the system to within an acceptable tolerance. This result supports the validity of the simulation and implemented gravitational dynamics to be used for future test cases.

5.2 Fidelity of Stable Configurations

The next cases to test are the three minimum energy configurations while in a stable, non-transitioning (static) configuration. This allows us to validate the fidelity of the contact force and tidal force dynamics. We now shift our attention to the equilibrium configurations of the full three-body problem. There are seven unique equilibrium configurations - of these, 4 are always unstable. These unstable equilibria are the: V-Rest configuration, Transverse Mixed configuration, Euler Orbiting configuration, and Lagrange Resting configuration (see Figure 2.3). We focus on the stable equilibria: the Lagrange Resting configuration, Euler Resting Configuration, and Aligned Mixed configuration. We wish to show that the simulation is capable of reproducing the stable and periodic orbit of these three stable configurations in the presence gravitational forces, contact forces, and tidal torques.

For each test case, we treated the bodies as spheres with equal diameters. The bulk body constants used for each simulation are listed in Table 5.1. The initial conditions specified are consistent with a tidally locked system for the given level of angular momentum of the system. The initial angular momentum for the system was chosen such that the test configuration was the only possible minimum energy configuration at that level of $\bar{H}^2$.

Table 5.1: Bulk Body Properties

d	$4\ [km]$
ρ	$2\ [g/cm^3]$
k_2	10^{-5}

5.2.1 Lagrange Resting Configuration

The system was initialized with a normalized value of angular momentum $\bar{H}^2 = 1$. The initial positions for each body of the Lagrange Resting configuration are calculated to form an equilateral triangle by connecting their centers. Their rotation axes are initially angled towards the system barycenter. Figure 5.2 shows the initial layout of the Lagrange Resting configuration.

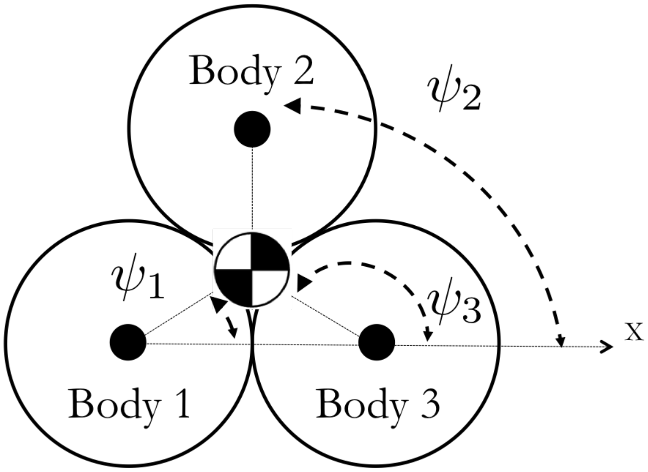

Figure 5.2: Lagrange Resting configuration.

The initial positions $\vec{r}_i$ and initial body rotation angles ψ_i for each body are specified as:

$$\vec{r}_1 = d\begin{bmatrix} -1/2 \\ -\sqrt{3}/6 \\ 0 \end{bmatrix} \qquad \vec{r}_2 = d\begin{bmatrix} 0 \\ \sqrt{3}/3 \\ 0 \end{bmatrix} \qquad \vec{r}_3 = d\begin{bmatrix} 1/2 \\ -\sqrt{3}/6 \\ 0 \end{bmatrix}$$

$$\psi_1 = \pi/6 \qquad \psi_2 = -\pi/2 \qquad \psi_3 = 5\pi/6$$

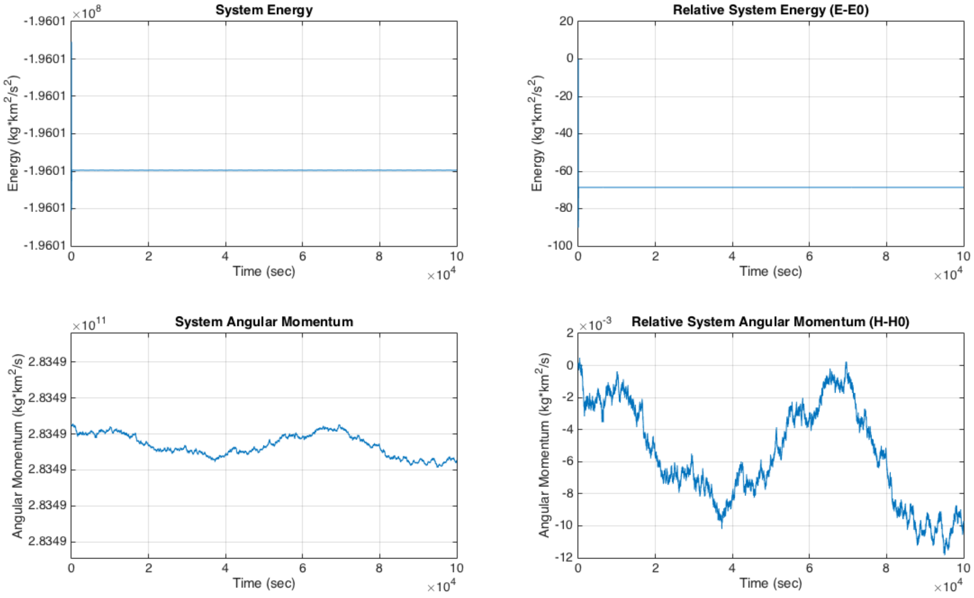

Figure 5.3: Energy and angular momentum for the static Lagrange Resting configuration. Plots on the right are the respective values of energy and angular momentum compared to the initial values of the system.

As we can see in figure 5.3, the total energy of the system under the presence of contact forces and tidal torques is well behaved. There is a transient damped oscillation at the beginning of the simulation because the bodies are allowed to penetrate before the contact forces bring the dynamic state to a stable equilibrium.

Within the first 100 seconds, the energy oscillation damps to effectively 0 and remains bounded for the simulation duration. The error in energy is contained to within 1 part in 10^6. The angular momentum of the system experiences a net negative trend. However, the total error in angular momentum is within 1 part in 10^{12} and thus has a negligible effect on the behavior of the system.

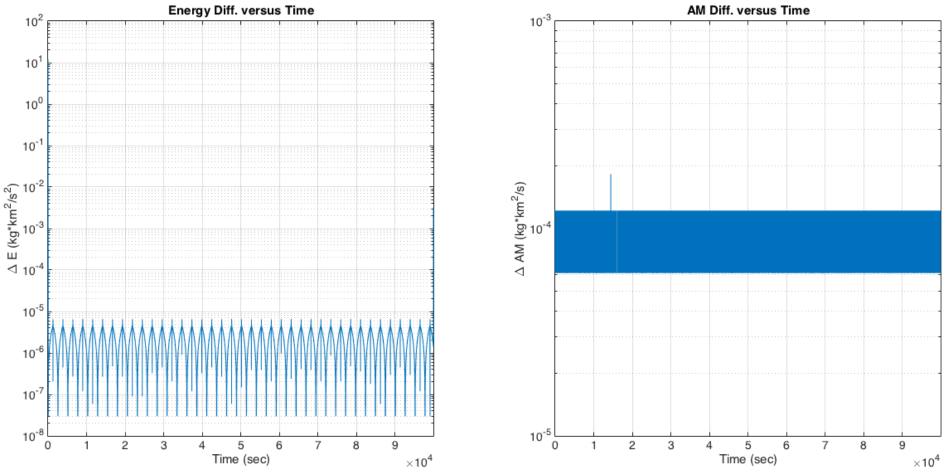

Figure 5.4: Left: Energy and angular momentum change incurred between timesteps over simulation duration. Right: Energy and angular momentum change incurred between timesteps over simulation iteration.

Figure 5.4 shows the magnitude change of energy and angular momentum between every timestep of the simulation. This allows us to gauge the accuracy of a single propagation step. As can be seen, the change in total energy over a single step ranges from 10^{-6} to 10^{-8}, ignoring the initial energy change as the contact forces reach equilibrium. We want to make sure that the energy changes are not accumulating (however small they may be). By examining the final quarter of the simulation, we can confirm that the accumulated energy changes are bounded and oscillate about some mean value as seen in Figure 5.5. The accuracy of the total angular momentum ranges from 10^{-4} to 10^{-5} over each timestep. Unlike with the energy deviations, the errors in angular momentum at each timestep accumulate.

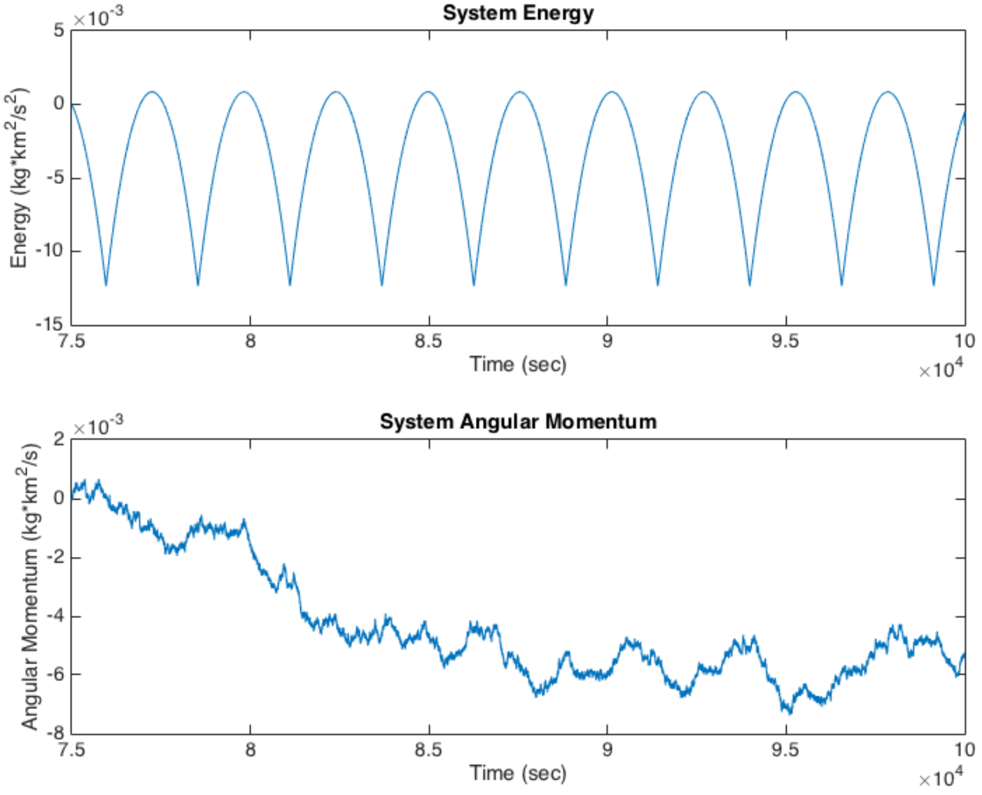

Figure 5.5: Changes in total energy and angular momentum compared to the state at 75,000 seconds during the final 1/4 of the static Lagrange Resting simulation.

Next we examine the agreement of the body relative positions as compared to the analytic configuration. For the Lagrange Resting configuration, all bodies start out exactly d from their mutual centers, each separated by 120°. By looking at Figure 5.6, we can track the displacement from the initial relative positions of each body. We see that there is a slight penetration between body pairs of about 1.5 mm. This is a negligible amount of penetration; note that some small penetration is necessary for the bodies to reach a steady state and remain in persistent contact.

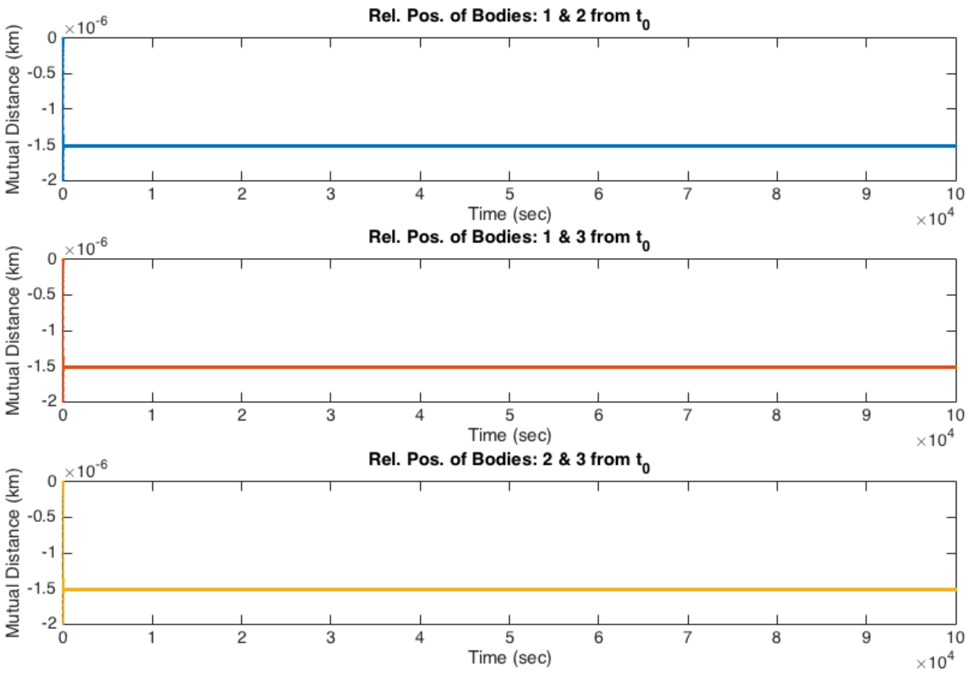

Figure 5.6: Displacement of relative positions between bodies for the static Lagrange Resting simulation. All three bodies remain in contact at a fixed distance from their centers.

Furthermore, we can quantify the degree to which the relative positions of the bodies align with the ideal configuration by calculating a metric we defined called the form factor. The form factor $F\theta$ is simply the angle between two bodies and the barycenter:

$$F\theta_{k,m} = \cos^{-1}\left(\frac{\vec{r}_k \cdot \vec{r}_m}{|\vec{r}_k|\,|\vec{r}_m|}\right) \tag{5.1}$$

By comparing the form factor of each pair of bodies to the form factor of the ideal configuration, we can get a sense for how aligned the numerical system is to the ideal system (see Figure 5.7). For the Lagrange Resting configuration, the ideal form factor between each pair of bodies is precisely 120°.

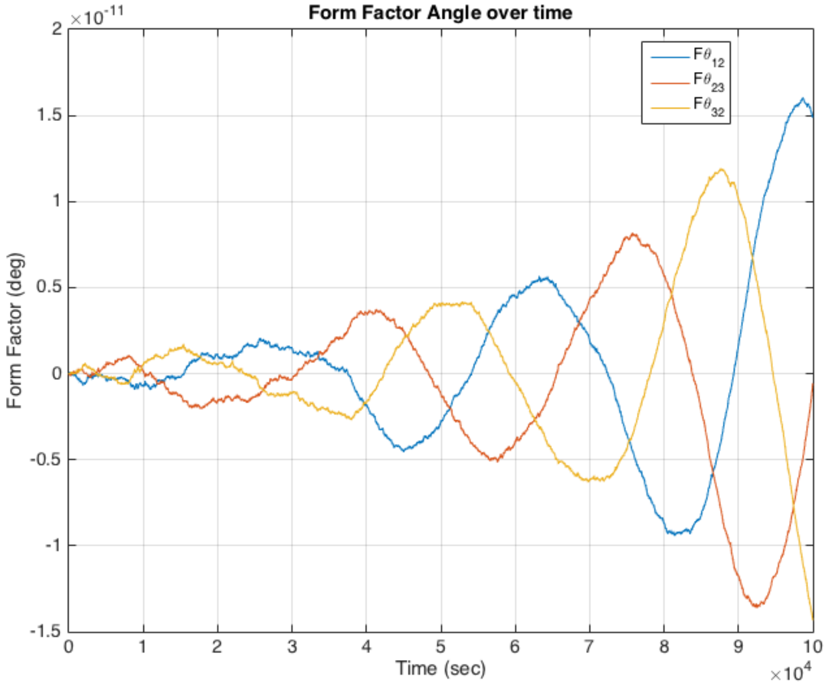

Figure 5.7: Form factor of each body compared to the ideal form factor of 120 degrees for the static Lagrange Resting simulation.

Although there is a growing trend of all the relative form factors, the negligible magnitude of 10^{-11} degrees suggests that the bodies are well aligned with the ideal configuration.

Finally, we wish to compare the orbital rate of the bodies about the barycenter to the analytical rate n. Using a a value of $\bar{H}^2 = 1$, we can calculate the ideal orbital rate to be $n = 2.03357 \cdot 10^{-4}$ $[rad/s]$. Figure 5.8 shows the instantaneous orbital rate of the bodies about the barycenter.

As seen from the plot, the bodies are rotating about the barycenter at same rate as the analytical rate we calculated. Thus we are able to say that the behavior of the simulated static Lagrange Resting configuration agrees with the expected behavior of the analytical case. With this configuration fully functional, we move

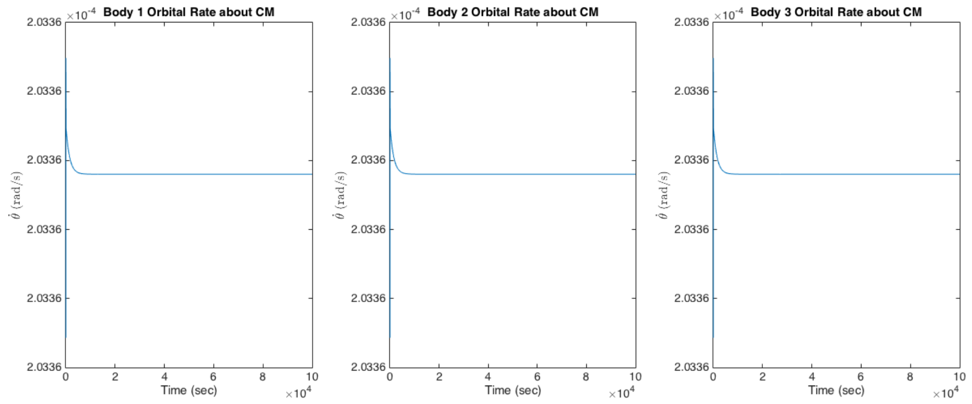

Figure 5.8: Instantaneous mean motion of each body about barycenter for static Lagrange Resting simulation. The value is equivalent to the analytical orbital rate.

on to testing the static Euler Resting configuration.

5.2.2 Euler Resting Configuration

The system was initialized with a normalized value of angular momentum $\bar{H}^2 = 3.5$. The initial positions for each body of the Euler Resting configuration are calculated such that their centers are all collinear. Their rotation axes are initially angled towards the system barycenter. Figure 5.9 shows the initial layout of the Euler Resting configuration.

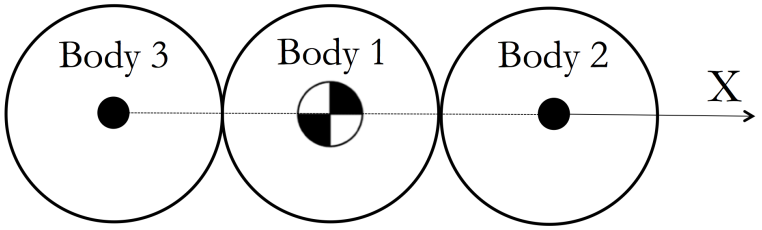

Figure 5.9: Euler Resting configuration.

The initial positions $\vec{r}_i$ and initial body rotation angles ψ_i for each body are specified as:

$$\vec{r}_1 = \begin{bmatrix} 0 \\ 0 \\ 0 \end{bmatrix} \qquad \vec{r}_2 = \begin{bmatrix} d \\ 0 \\ 0 \end{bmatrix} \qquad \vec{r}_3 = \begin{bmatrix} -d \\ 0 \\ 0 \end{bmatrix}$$

$$\psi_1 = 0 \qquad \psi_2 = 0 \qquad \psi_3 = 0$$

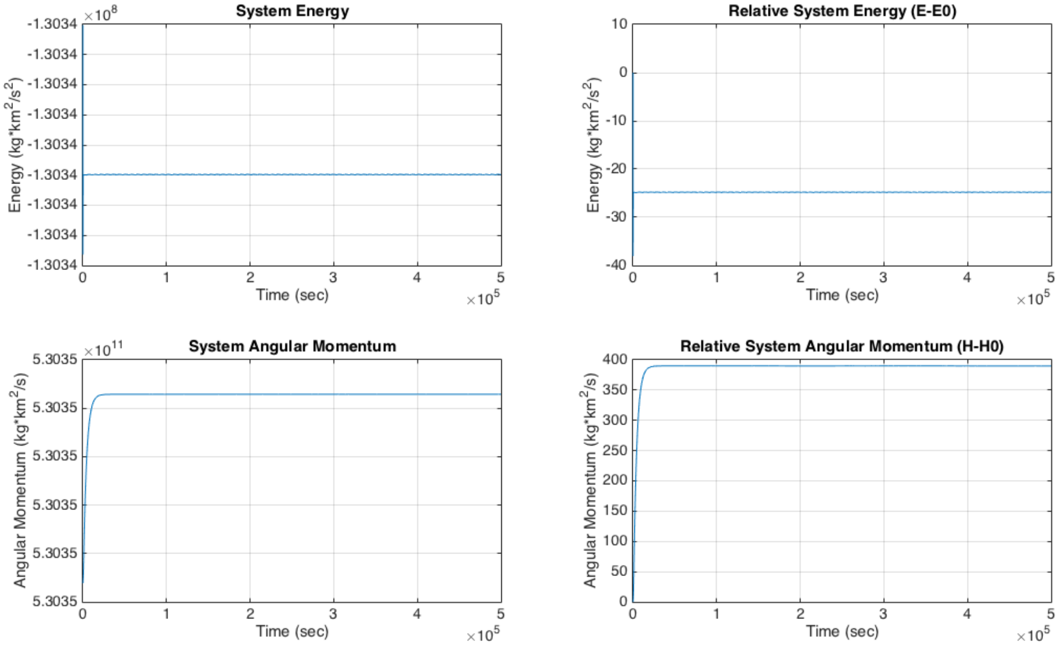

Figure 5.10: Energy and angular momentum for the static Euler Resting configuration. Plots on the right are the respective values of energy and angular momentum compared to the initial values of the system.

Immediately we see a transient damped oscillation in the total energy of the system. This is the same phenomenon observed in the static Lagrange Resting case: the interaction of the gravitational and spring forces shift the equilibrium penetration slightly, leading to an overall increase in energy. However the spring damper quickly brings the total energy gain to a near constant value that it will continue to oscillate about. The global error in energy is less than 1 part in 10^7. The angular momentum behaves similarly; the system undergoes a transient gain in total angular momentum until a force balance is reached. The global error in angular momentum is less than 1 part in 10^9.

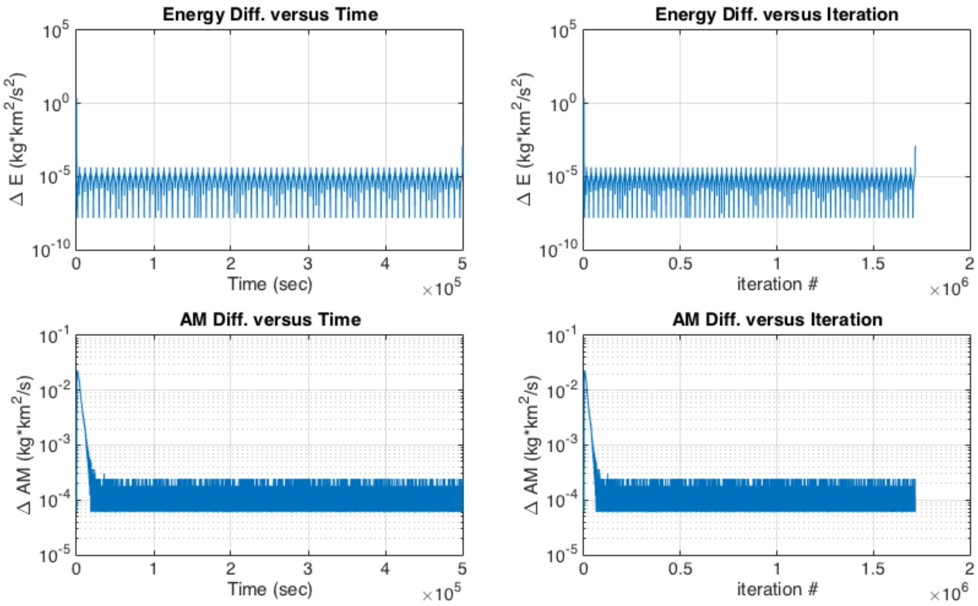

Figure 5.11: Left: Energy and angular momentum change incurred between timesteps over simulation duration. Right: Energy and angular momentum change incurred between timesteps over simulation iteration. Both plots are for the static Euler Resting simulation.

Figure 5.4 shows the magnitude change of energy and angular momentum between every timestep of the simulation. As can be seen, the accuracy in total energy over a single step ranges from 10^{-5} to 10^{-8}, ignoring the initial energy change as the contact forces reach equilibrium. We can again show that the small energy errors are not accumulating by examining the final quarter of the simulation. From

Figure 5.12 we can confirm that the accumulated energy changes are bounded and oscillate about some mean value. The accuracy of the total angular momentum ranges from 10^{-4} to 10^{-5} over each timestep. Unlike with the energy deviations, the errors in angular momentum at each timestep accumulate and show a negative trend. The cause is most likely numerical inaccuracies of the integrator as error is within 1 order of magnitude of the allowed error tolerance. For the timescales we are simulating, this small error has no physical impact on the stability and configuration of the system.

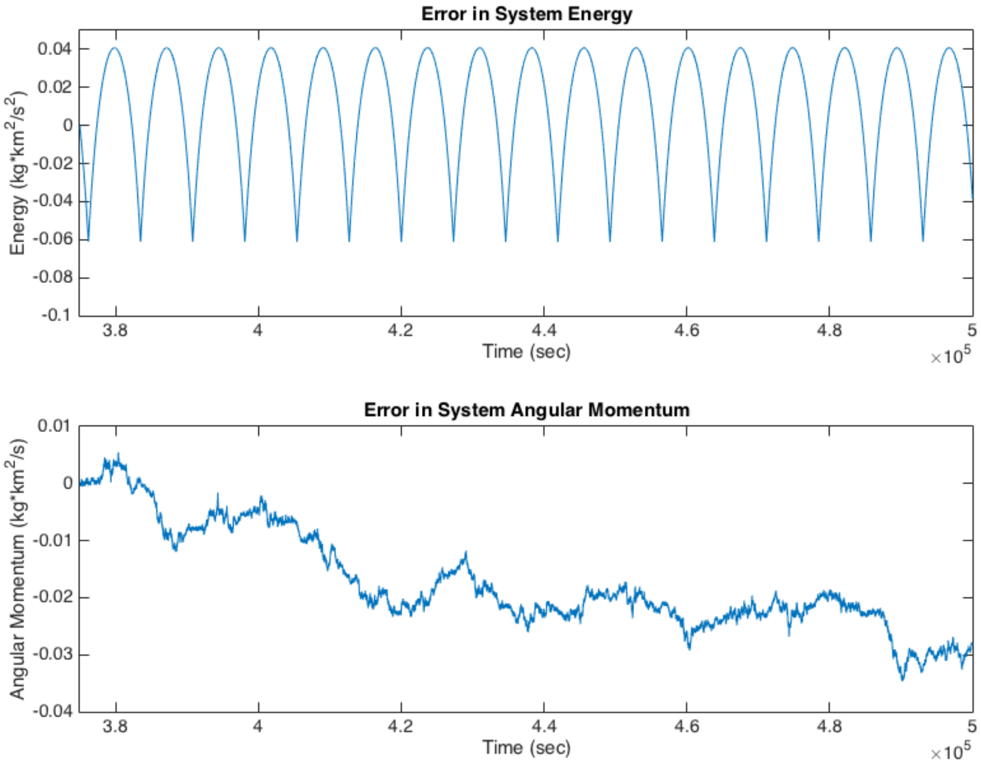

Figure 5.12: Energy and angular momentum accumulated error per timestep during the final 1/4 of the static Euler Resting simulation.

Next we examine the uniformity of the body positions relative to the analytic configuration. For the Euler Resting configuration, the two outer bodies start out exactly d from the center body. By looking at Figure 5.6, we can track the displacement from the initial relative positions of each body. We see that there is a slight penetration between body pairs of about 1.5 mm. This is a negligible amount of penetration; note that some small penetration is necessary for the bodies to reach a steady state and remain in persistent contact.

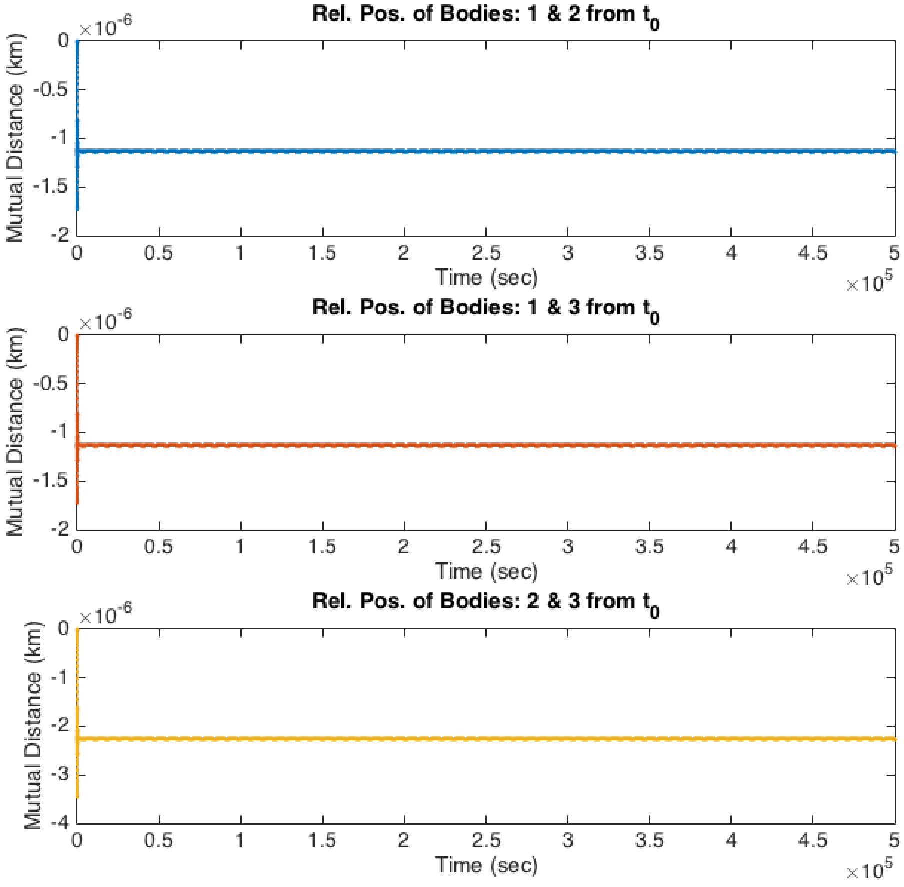

Figure 5.13: Displacement of relative positions between bodies. The two outer bodies (2 and 3) remain at a fixed distance from the center body (1).

For the Euler Resting configuration, the ideal form factor between each pair of bodies is 0 degrees. The center body (1) is at or very close to the origin of the system, so we take form factor between the center body and outer two bodies to always be 0. In this case, we are only interested in the form factor between the outer two bodies $F\theta_{2,3}$.

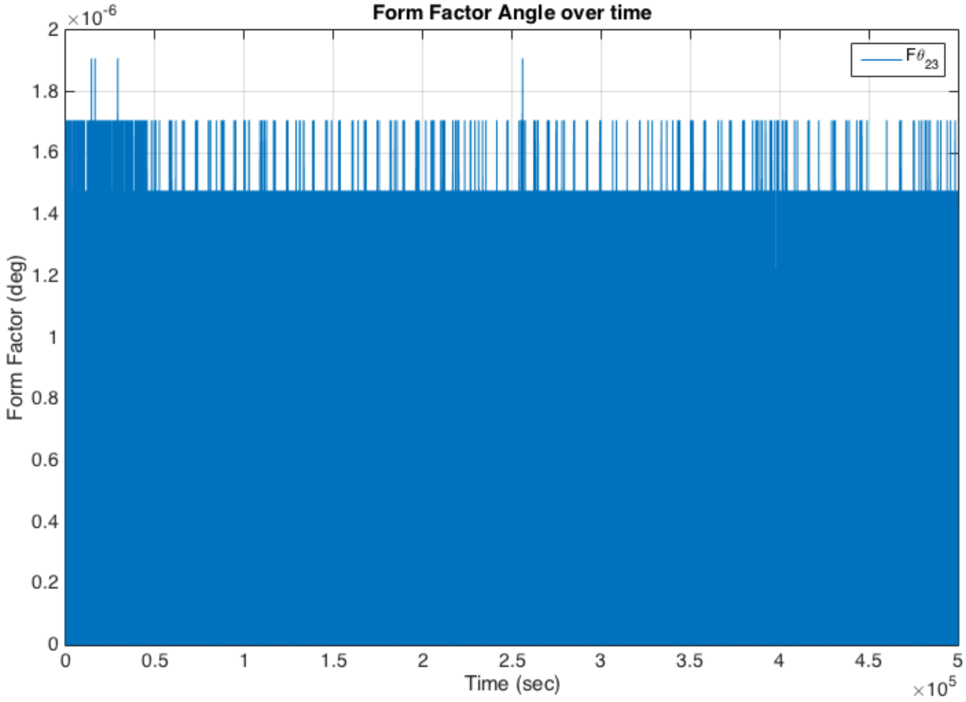

Figure 5.14: Form factor angle between the outer bodies 2 and 3 of the static Euler Resting simulation.

The form factor between body 2 and 3 fluctuates wildly, but remains bounded between $\pm 2 \cdot 10^{-6}$ degrees. Thus we can conclude that the relative positions of the bodies remain close enough to the ideal equilibrium configuration.

Finally, we wish to compare the orbital rate of the bodies about the barycenter to the analytical rate n. Using a a value of $\bar{H}^2 = 3.5$, we calculate the ideal orbital rate to be $n = 2.15035 \cdot 10^{-4}$ $[rad/s]$. In Figure 5.15, we show the instantaneous orbital rate of each body about the barycenter:

As seen from Figure 5.15, the bodies are rotating about the barycenter at same rate as the analytical rate we calculated. The center body (1) was not included

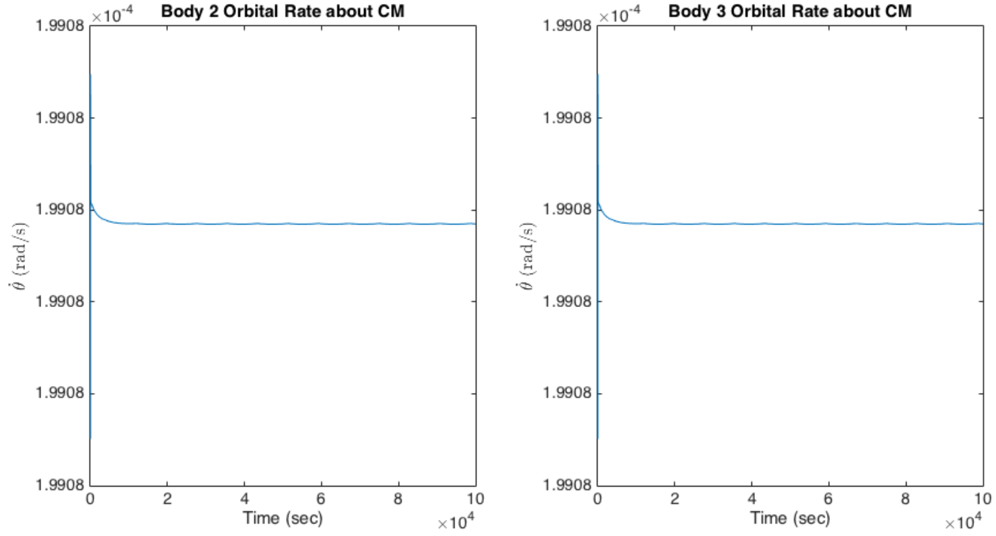

Figure 5.15: Instantaneous mean motion of each body about barycenter for the static Euler Resting simulation. The value is equivalent to the analytical orbital rate.

because it orbits at or very close to the origin. Thus we are able to say that the behavior of the simulated static Lagrange Resting configuration agrees with the expected behavior of the analytical case. With this configuration fully working, we move on to testing the static Aligned Mixed configuration.

5.2.3 Aligned Mixed Configuration

The system was initialized with a normalized value of separation $R = 3.6$. The initial positions for each body of the Aligned Mixed configuration are calculated such that their centers are all collinear. Their rotation axes are initially angled towards the system barycenter. Figure 5.16 shows the initial layout of the Euler Resting configuration.

The initial positions $\vec{r}_i$ and initial body rotation angles ψ_i for each body are specified as:

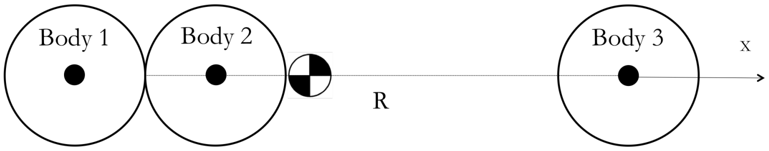

Figure 5.16: Aligned Mixed configuration.

$$\vec{r}_1 = \begin{bmatrix} -d/2 \\ 0 \\ 0 \end{bmatrix} \qquad \vec{r}_2 = \begin{bmatrix} d/2 \\ 0 \\ 0 \end{bmatrix} \qquad \vec{r}_3 = \begin{bmatrix} dR \\ 0 \\ 0 \end{bmatrix}$$

$$\psi_1 = 0 \qquad \psi_2 = 0 \qquad \psi_3 = 0$$

The total energy of the system in Figure 5.17 is well conserved. There is a transient damped oscillation at the beginning of the simulation like all of the previous test cases. The error in energy is contained to within 1 part in 10^6. The angular momentum of the system oscillates with larger peaks than the previous stable test configurations. However, the global error in angular momentum is still within 1 part in 10^8 and will have a negligible effect on the behavior of the system. The errors in angular momentum are larger in this scenario because the relative rotation rate $\dot{\phi}$ between bodies takes a greater time to reach equilibrium.

If we look at the figure of relative rotation rates 5.18, we see that bodies are oscillating about the 0 line as they slowly converge.

We see the results of this effect in the orbital and body-centered rotational

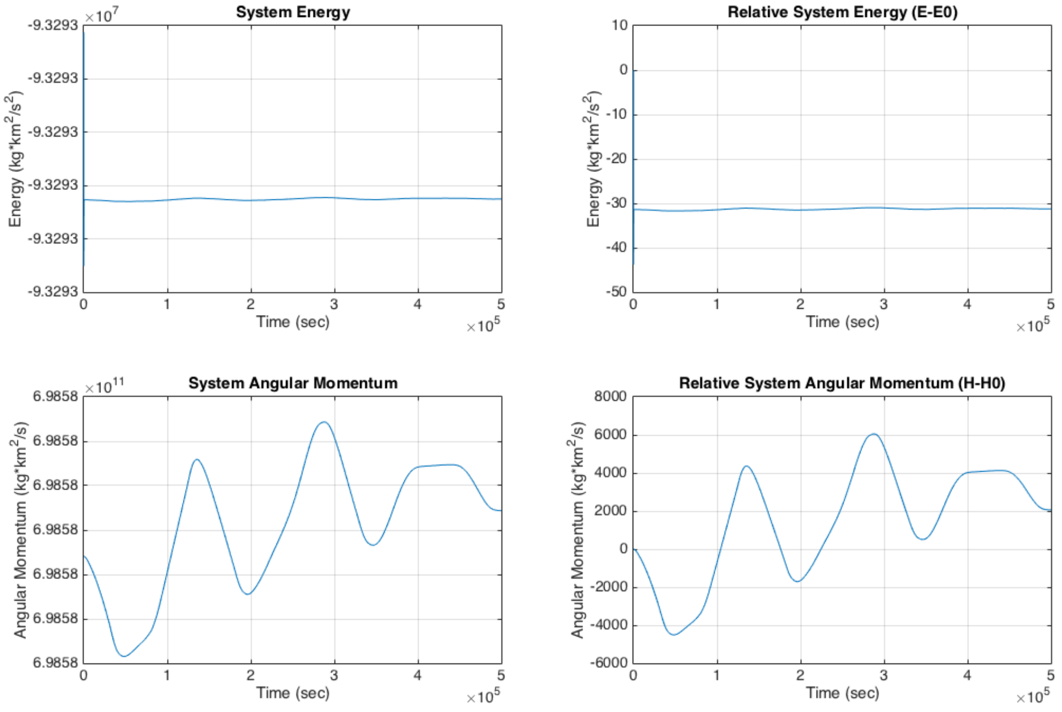

Figure 5.17: Energy and angular momentum for the static Aligned Mixed configuration. Plots on the right are the respective values of energy and angular momentum compared to the initial values of the system.

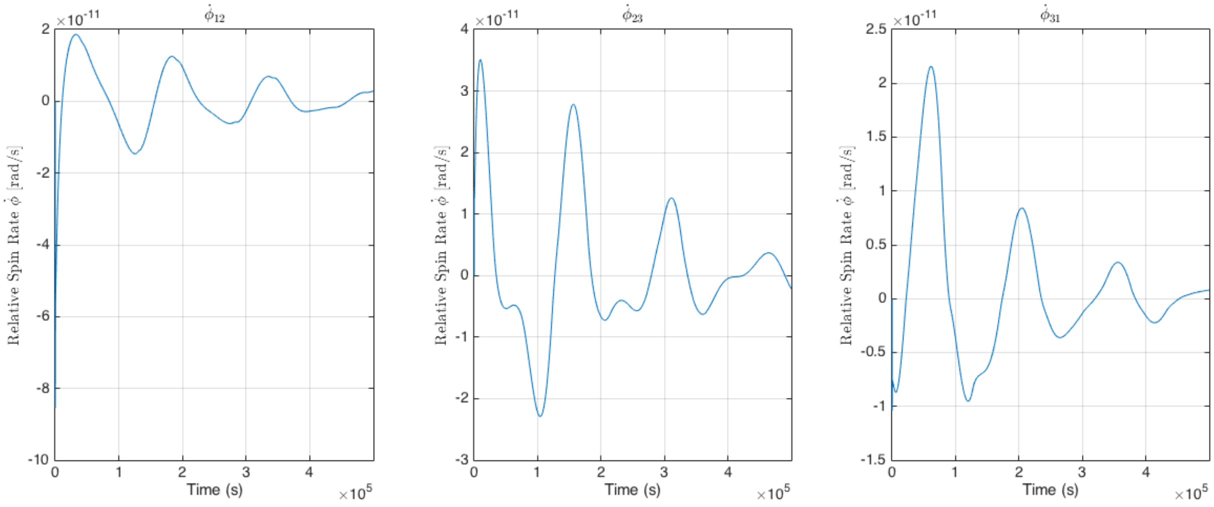

Figure 5.18: Relative angle rotation rate between body pairs for the static Aligned Mixed configuration.

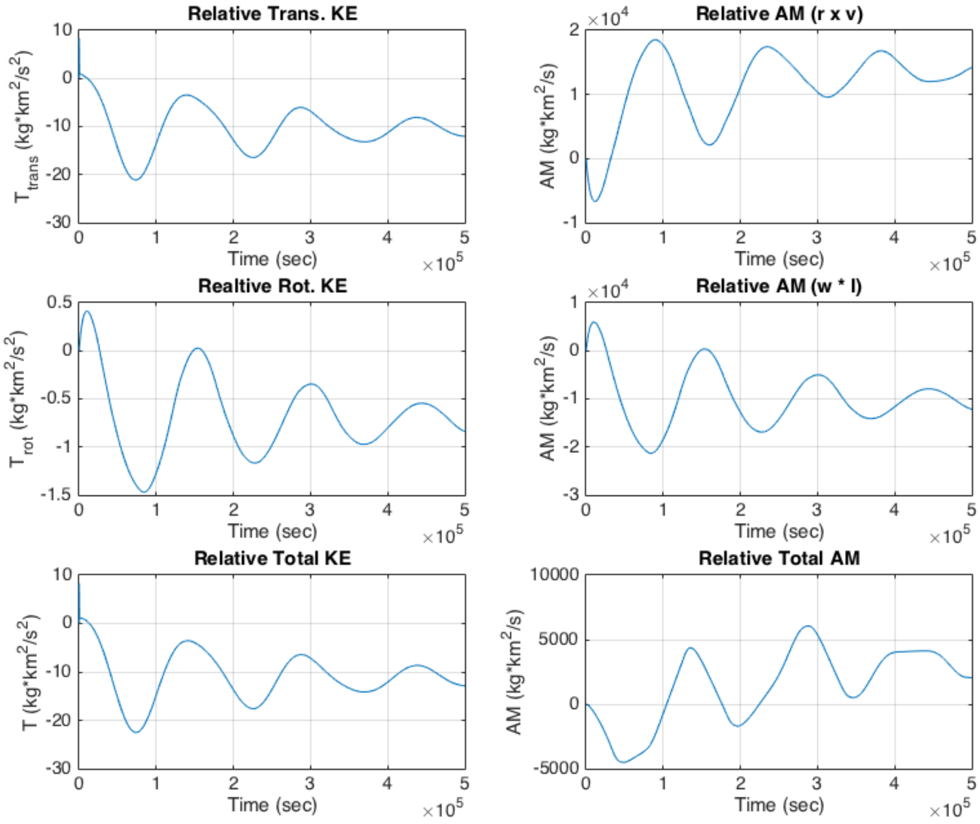

Figure 5.19: Left: Components of kinetic energy T relative to initial state. Right: Components of angular momentum relative to initial state. Plots are for the static Aligned Mixed simulation

components of the total angular momentum over time in Figure 5.19. As expected, the orbital component of angular momentum $\vec{r} \times \vec{v}$ changes with the reciprocal of the body-center rotational angular momentum ωI. Both components of angular momentum change to match the sign and magnitude of $\dot{\phi}$, and are likewise slowly converging to a steady state value.

Figure 5.20 shows the magnitude change of energy and angular momentum between every timestep of the simulation. The accuracy in total energy over a single step ranges from 10^{-5} to 10^{-7}, ignoring the initial energy change as the contact forces

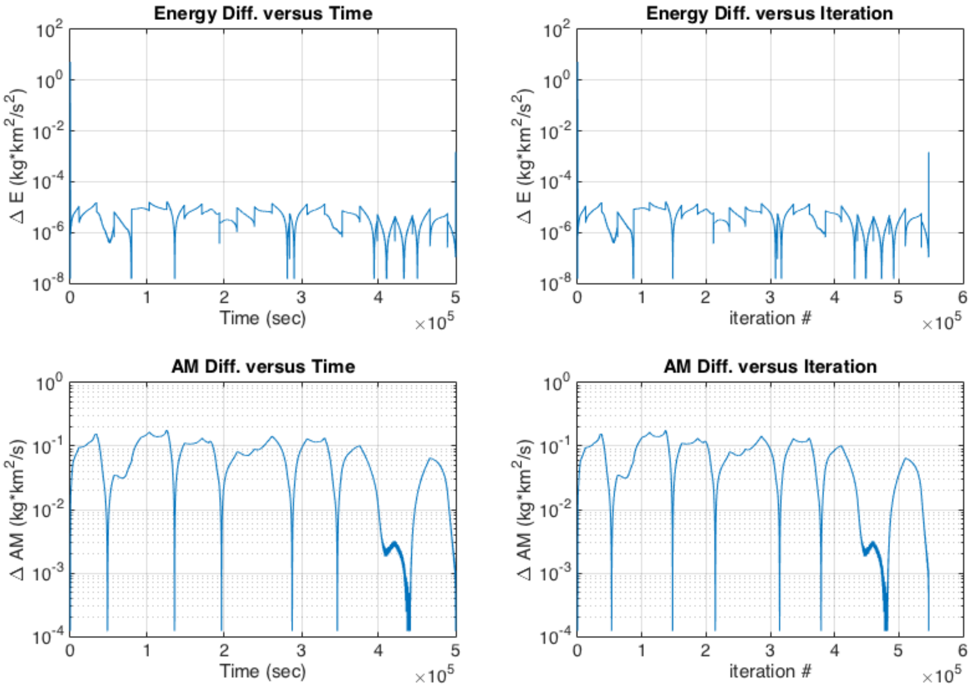

Figure 5.20: Left Energy and angular momentum change incurred between timesteps over simulation duration. Right: Energy and angular momentum change incurred between timesteps over simulation iteration.

reach equilibrium. The accuracy of the total angular momentum ranges from 10^{-4} to 10^{-5} over each timestep. This test case has greater errors in conserved quantities because of the inherent asymmetry in the initial configuration of the bodies. In the previous Euler and Lagrange Resting configurations, accumulated errors affected all bodies equally and this typically resulted in a smaller global error. We still want to make sure that the energy changes are not accumulating in one direction. By examining the final quarter of the simulation, we continue to see relatively small changes in the system energy and angular momentum, although the system has yet to converge to a steady state value 5.21. Based on the continuing trend of $\dot{\phi}$, we can expect the energy and angular momentum errors to converge if the simulation were run for a longer duration. While undesirable, the larger errors in conserved quantities have a negligible affect on the stability of the system and can be ignored.

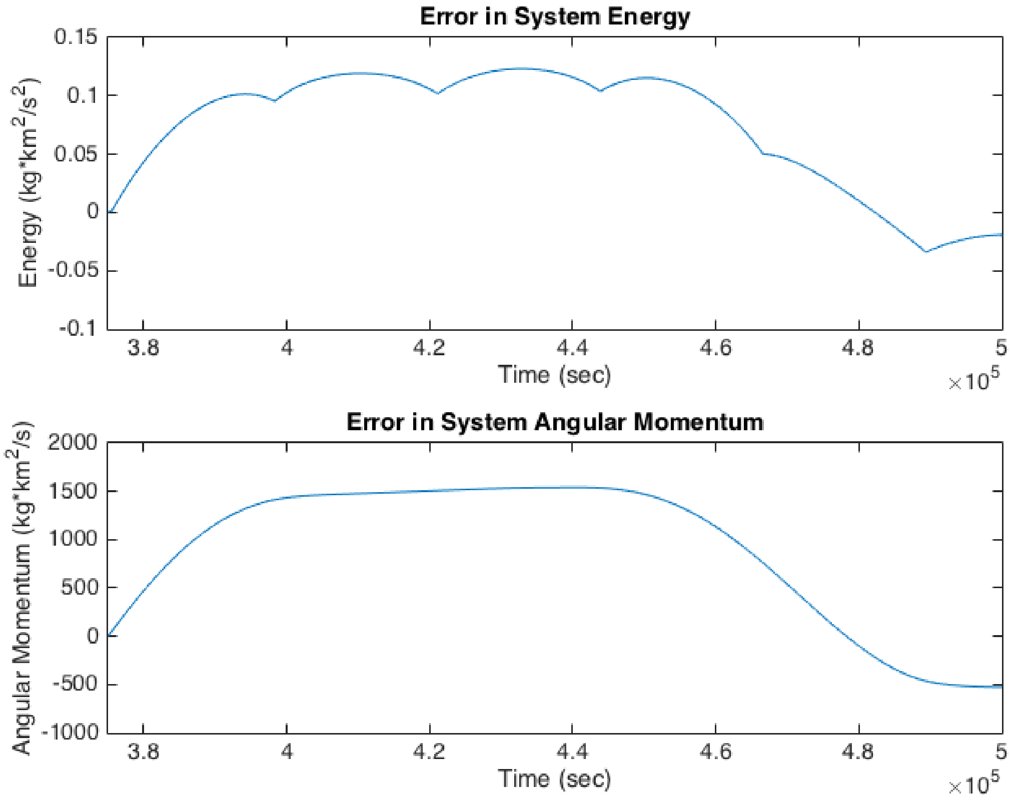

Figure 5.21: Energy and angular momentum during the final 120,000 seconds of the static Aligned Mixed simulation.

Next we examine the uniformity of the body positions relative to the analytic configuration. For the Aligned Mixed configuration, all bodies start out exactly d from their mutual centers. By looking at Figure 5.22, we can track the displacement from the initial relative positions of each body. We see that there is a slight penetration between the two bodies in contact (1 and 2) of about 1.8 mm. The other two body pairs oscillate by a few millimeters but are slowly converging to a steady state value.

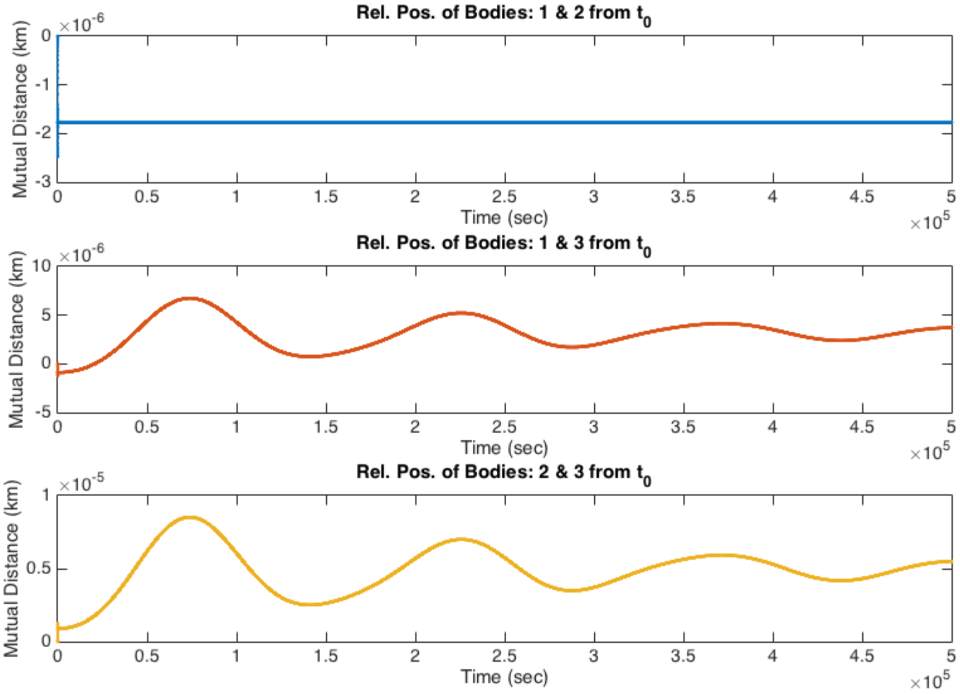

Figure 5.22: Displacement of relative positions between bodies for the static Aligned Mixed configuration. Bodies 1 and 2 are the contact pair.

By comparing the form factor of each pair of bodies to the form factor of the ideal configuration, we can get a sense for how aligned the numerical system is to the ideal system 5.23. For the Aligned Mixed configuration, the ideal form factor between each pair of bodies is 0 degrees.

There are slight deviations in the form factors but they are all bounded by fractions of a degree, and so we can say that the bodies maintain the ideal configuration of the analytic solution.

Finally, we wish to compare the orbital rate of the bodies about the barycenter to the analytical rate n. Using a a value of $\bar{H}^2 = 1$, we can calculate the ideal orbital rate to be $n = 6.0911 \cdot 10^{-4}$ $[rad/s]$. The instantaneous orbital rates of the bodies

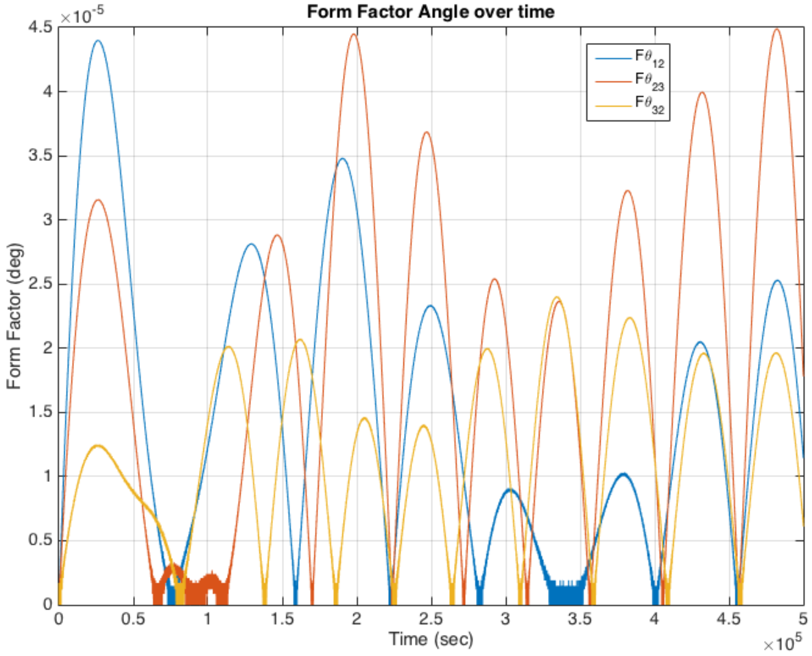

Figure 5.23: Form factor of bodies in static Aligned Mixed configuration. Ideal form factor is 0 degrees.

are plotted in Figure 5.24:

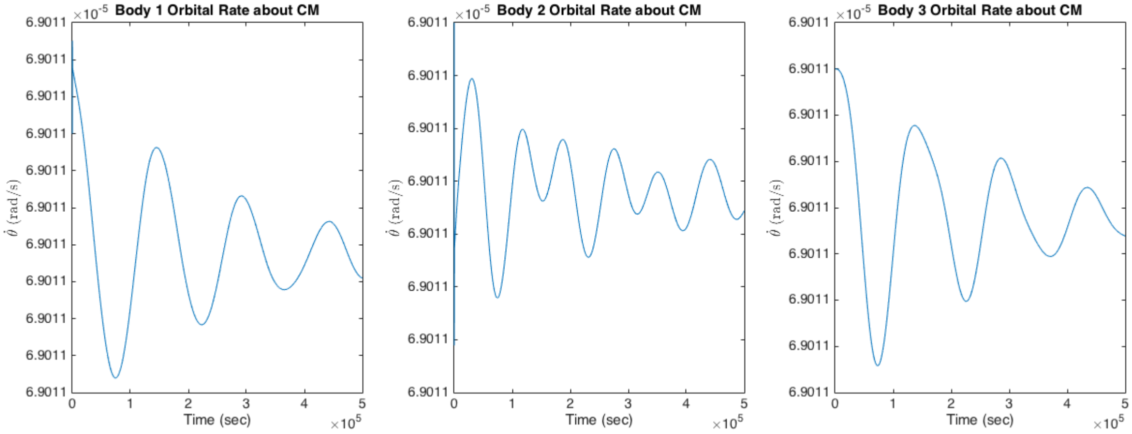

Figure 5.24: Instantaneous mean motion of each body about barycenter for the static Aligned Mixed simulation. The value is equivalent to the analytical orbital rate.

As seen from the plot, the bodies are rotating about the barycenter at same rate as the analytical rate we calculated. Thus we are able to say that the behavior of the simulated static Aligned Mixed configuration agrees with the expected behavior of the analytical case.

We see that all three simulated minimum energy configurations behave in a physically accurate way. These tests cases support the robustness simulation to produce accurate and useable results. We are aware of small errors produced by the soft-sphere DEM contact force model and tidal torques and how they may influence the results of the transitional test cases. The nature of the errors in this model and simulation will be addressed further in the Error Analysis chapter. We will now investigate the pathways of transitioning minimum energy configurations and the timescales to reach a terminal, tidally locked configuration.

5.3 Transitions Between Minimum Energy Configurations

There are three minimum energy configurations for the full three-body problem over the entire range of possible angular momenta, allowing for a total of four possible transitions. Each minimum energy configuration exists on a definite interval of angular momentum. Once $\bar{H}^2$ exceeds the defined interval of a minimum energy configuration, the arrangement becomes unstable and the bodies will escape into a chaotic trajectory. Eventually, the bodies will reform into a different minimum energy configuration defined by the new angular momentum $\bar{H}^2$ of the system. There is no analytical method to determine the trajectories of the bodies as they transition between minimum energy configurations. We intend to elucidate the behavior of the bodies during this transition period and provide a more graphical, and thus intuitive, understanding of the entire process. During the transition, bodies may collide with each other multiple times before settling into a persistent contact. In addition, collisions dissipate huge amounts of excess mechanical energy and accelerate the time needed for all excess mechanic energy to decay. Any excess mechanical energy remaining after collisions will be slowly dissipated thru the interaction of tidal forces. We intend to demonstrate the mechanism by which tidal forces synchronize the rotation and orbital rates of the gravitating bodies. In addition, we estimate the timescales necessary for tidal locking to occur based on the rate of energy decay observed in the final quasi-steady state of the system.

The state variables of the bodies are initialized with a value of angular momentum $\bar{H}^2$ that is slightly outside of the range of valid $\bar{H}^2$ for which the minimum energy configuration exists. This initial state can be thought of as the moment after which the YORP affect has imparted enough change in angular momentum to invoke a transition.

Additionally, we applied a relatively small perturbation to the initial state variables compared to an idealized system. The perturbation was almost always a displacement in initial position of one the bodies that did not significantly affect the initial angular momentum of the system. This perturbation serves two purposes: first, it creates an asymmetry in the system that will cause the bodies to begin their transition faster. In a symmetric system, like the Euler Resting configuration, the forces on each body are equal and opposite. However for the bodies to transition, in this case say to an Aligned Mixed configuration, one outer body must remain in contact while the other separates - a physically impossible scenario if both outer bodies are behaving in an identically symmetric manner. Eventually, numerical errors will force an asymmetry in the system before the bodies begin their transition. Perturbing the system at the start of the simulation accelerates the simulation without disturbing the integrity of the results. Specifying an initial perturbation of the system also reduces the potential for additional state variable errors to enter the system during the aforementioned pre-transitional period of symmetry.

5.3.1 Lagrange Resting to Euler Resting

We begin our investigation with the transition from the Lagrange Resting configuration to the Euler Resting configuration. The Lagrange Resting configuration is the minimum energy configuration for values of angular momentum between $0 < \bar{H}^2 < 2.99$. Above this value, the Euler Resting configuration is the lowest energy state. The Lagrange Resting configuration continues to be energetically stable up until $\bar{H}^2 < 5.07$ at which point the centrifugal forces overcome gravitational forces and the bodies will initially transition to an unstable Lagrange Orbiting configuration and then a Euler Resting configuration. The only stable configuration immediately available above this threshold is the Euler Resting configuration.

The system is initialized with an angular momentum of $\bar{H}^2 = 5.2$. The position of body 3 is perturbed by a displacement $\delta x = d(10^{-3})$ in the positive X direction, where d is the diameter of the bodies. We use canonical units, such that $d = 2$. Given this displacement, the updated system angular momentum is displaced to $\bar{H}^2 = 5.204$.

The initial positions $\vec{r}_i$ and initial body rotation angles ψ_i for each body are specified as:

$$\vec{r}_1 = d \begin{bmatrix} -1/2 \\ -\sqrt{3}/6 \\ 0 \end{bmatrix} \qquad \vec{r}_2 = d \begin{bmatrix} 0 \\ \sqrt{3}/3 \\ 0 \end{bmatrix} \qquad \vec{r}_3 = d \begin{bmatrix} 1/2 + 10^{-3} \\ -\sqrt{3}/6 \\ 0 \end{bmatrix}$$

$$\psi_1 = \pi/6 \qquad \psi_2 = -\pi/2 \qquad \psi_3 = 5\pi/6$$

The simulation parameters are shown in Table 5.2.

Table 5.2: LR to ER Simulation Parameters

Error Tolerance	ϵ	10^{-6}
Initial Step Size	h_0	10^{-2} $[TU]$
Simulation Duration	t_{end}	$500,000[s]$

All bodies immediately separate from one another, forming a quasi-Lagrange Orbiting configuration as expected. The bodies continue to orbit until the initial asymmetry results in a soft collision at approximately $t = 12,300$ seconds between bodies 2 and 3. The two bodies immediately separate, after which another soft collision occurs between bodies 1 and 2. Then at $t = 19,880$ seconds a harder collision occurs betweens bodies 1 and 3, and they form a brief persistent contact the lasts for about 4,000 seconds before separating. These events are obvious by looking at the inelastic collision energy losses for the first 30,000 seconds in Figure

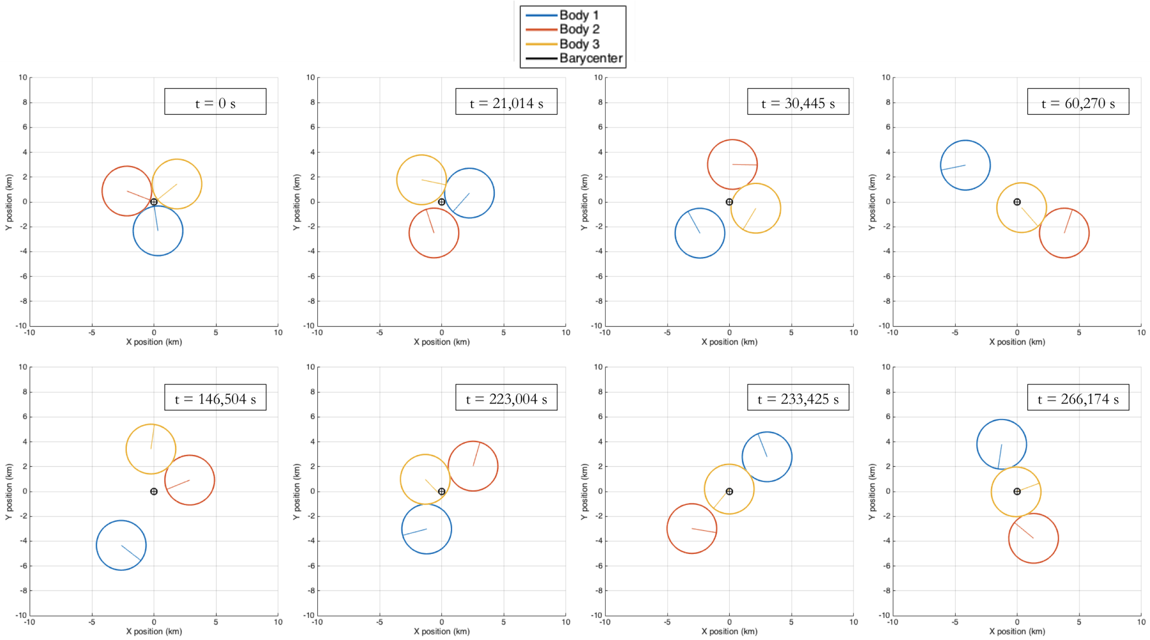

Figure 5.25: Lagrange Resting Configuration transitioning to Euler Resting Configuration. Each frame shows the orientation of the bodies and their body rotation angle at a specific time.

5.26.

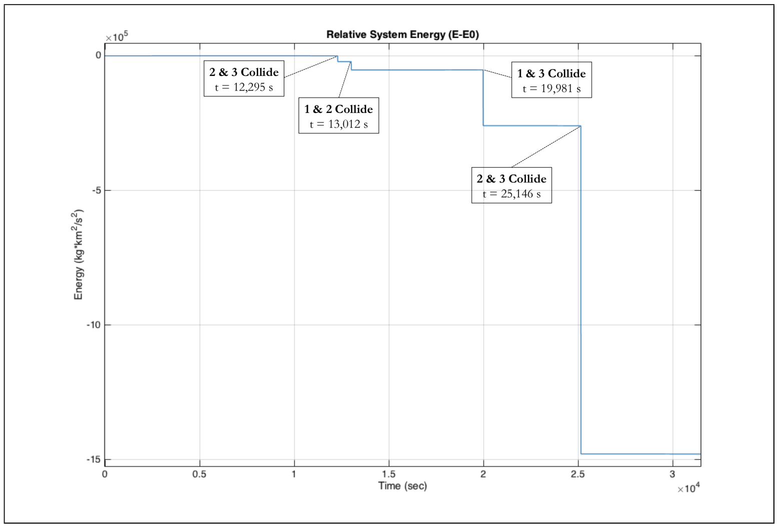

Figure 5.26: Collisions apparent through large system energy losses for the first 30,000 seconds for the simulated transition from LR to ER.

Next, bodies 2 and 3 experience the hardest collision yet (greatest energy loss) and form a long lasting persistent contact. During the next 200,000 seconds, the bodies appear to tumble chaotically and form a quasi-Aligned Mixed configuration. The orbiting body (1) nearly collides with the two in-contact bodies on multiple occasions, but ultimately avoids a collision. Finally at $t = 222,600$ seconds, body 1 collides hard with body 3, and for the first time, a quasi-Euler Resting configuration is formed with body 3 as the center body. The impact of the collision temporarily launches body 2 out of contact and into a brief orbit. About 34,000 seconds later, at $t = 244,200$ seconds, body 2 collides back with body 3 and forms a persistent contact. These collision events are apparent in the Figure 5.27 by the large energy drops of the elastic collisions. After this point, the outer bodies (1 and 2) remain in persistent contact with the center body (3) for the remainder of the simulation.

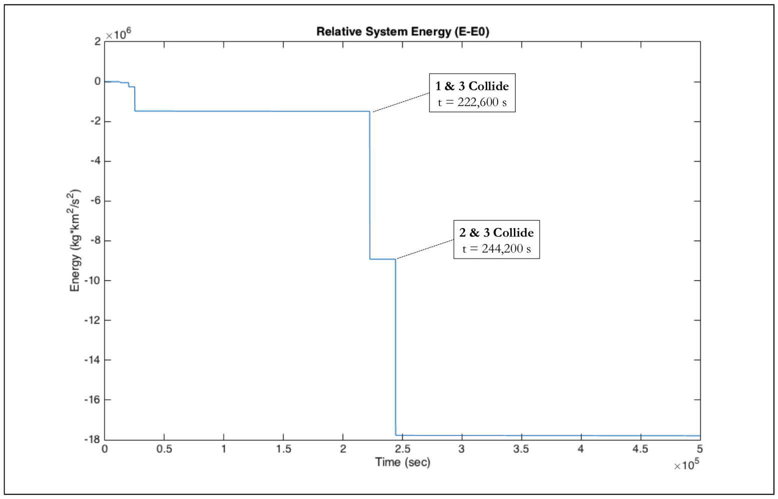

Figure 5.27: Collisions apparent through large system energy losses over full simulation duration for simulated transition from LR to ER.

All collisions cease beyond 244,200 seconds. To understand the behavior of system for the remaining 250,000 seconds of the simulation we turn out attention first to the relative positions of the bodies. Figure 5.28 shows that from about 250,000 seconds and onwards, the outer bodies 1 and 2 remain in contact with the center body 3. However, the distance between the two outer bodies oscillates as they roll across the surface of body 3, forming a quasi-V-Resting configuration.

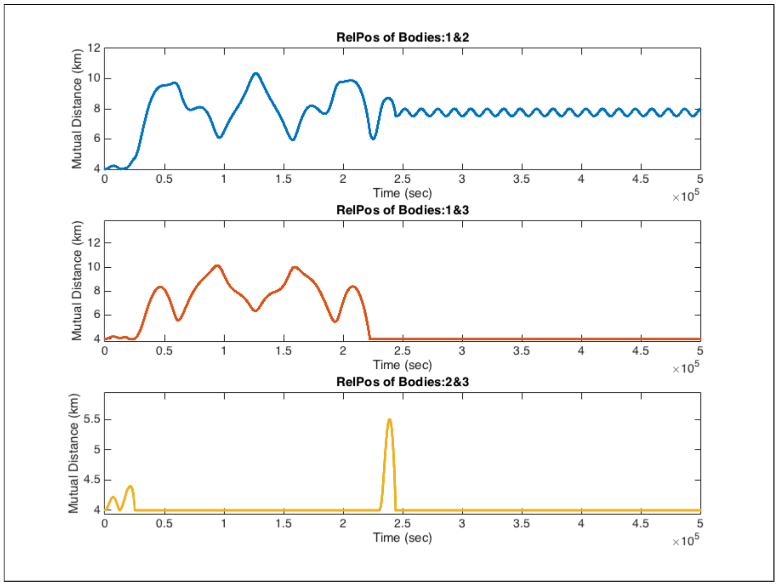

Figure 5.28: Relative body positions showing mutual body distances over the simulation. Note that the radius of each body is 2 km.

This oscillation of the outer bodies is further apparent by the form factor for the Euler Resting configuration, which we take to be the angle made between the center body and the two outer bodies. In this case, this equates to:

$$F\theta = \cos^{-1}\left(\frac{\vec{r}_{13} \cdot \vec{r}_{23}}{|\vec{r}_{13}|\,|\vec{r}_{23}|}\right) \tag{5.2}$$

From these two plots, we can infer that the two outer bodies are indeed rolling along the surface of the center body at regular intervals. The maximum deviance from the ideal form factor angle ($F\theta = 180°$) is bounded at about 40 degrees. However, we would like to be able to say whether these oscillation peaks are decreasing, suggesting that the bodies are approaching the analytical Euler Resting configu-

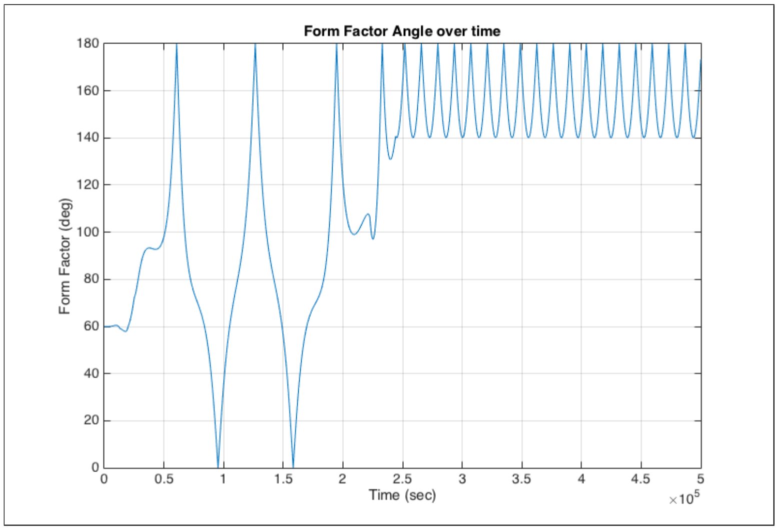

Figure 5.29: Form factor over the course of the simulation of the LR to ER transition. After collisions subside, the outer bodies oscillate between 140 and 180 degrees. Ideal form factor is 180 degrees.

ration. The brute force approach would be to simulate the system for a longer duration until we directly observe this event. However, in the second half of the simulation, all collisions have subsided and the bodies appear to have entered a stable, oscillatory state. At this point in the simulation, the only mode to decay the excess mechanical energy stored in the oscillations is thru tidal forces. To continue our investigation, we look at the weakly and slowly acting tidal forces present in the system.

Recall that the tidal torque and subsequent tidal force are essentially a constant for bodies in persistent contact but vary with their mutual body spin rate $\dot{\phi}$. If the 'Parent' body has a greater spin rate than the orbital rate of the 'Child' body ($\dot{\psi} > \dot{\theta}$), then a tidal torque Γ acts to slow the rotation rate $\dot{\psi}$ of the Parent body while an equivalent tidal force acts to increase the orbital rate $\dot{\theta}$ of the Child body. Indeed this is the case for the bodies in the last half of the simulation, as we can see from Figure 5.30.

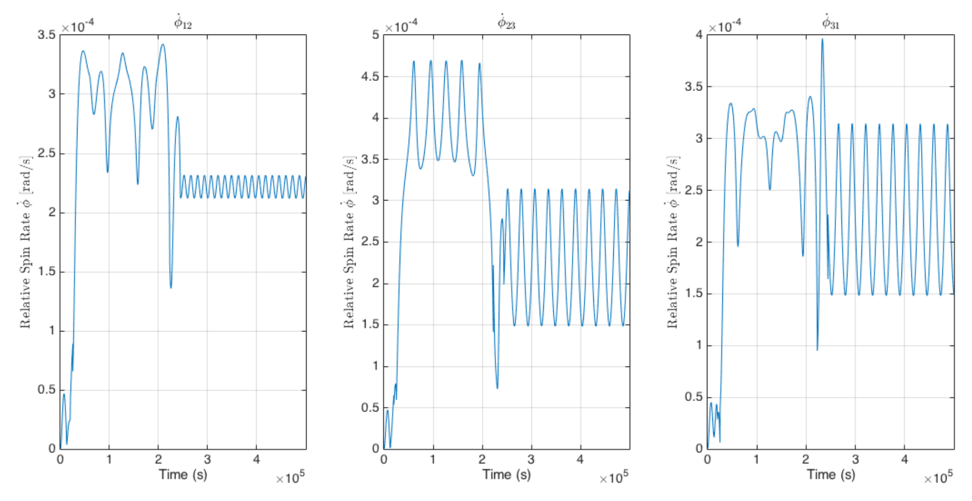

Figure 5.30: Relative body spin rate during the simulation of the LR to ER transition.

We see that after 250,000 seconds, all three bodies have a positive relative body spin rate that oscillates about $\dot{\phi} = 2.3145 \cdot 10^{-4}$ $[rad/s]$. A positive $\dot{\phi}$ for all body pairs implies that all bodies should be experiencing a decrease in their rotation rates $\dot{\psi}$ while experiencing an increase in their orbital velocity at a relatively constant rate. This is exactly the trend that is observed in Figure 5.31.

The top plot of Figure 5.31 represents the net change in orbital angular momentum starting at $t = 250,000$ seconds. Since the relative positions of the bodies remain fairly fixed ($d\vec{r}/dt \approx 0$), this plot implies that the orbital velocity (and orbital rate $\dot{\theta}$) of each body must be increasing. Similarly, the middle plot of the figure represents the change in angular momentum about each body's spin axis starting at $t = 250,000$ seconds. A net decrease here indicates that the rotation rate $\dot{\psi}$ of each body is also decreasing. Furthermore, the bottom plot of total angular momentum, which is the sum of the middle and top plots, indicates that the effects of these tidal

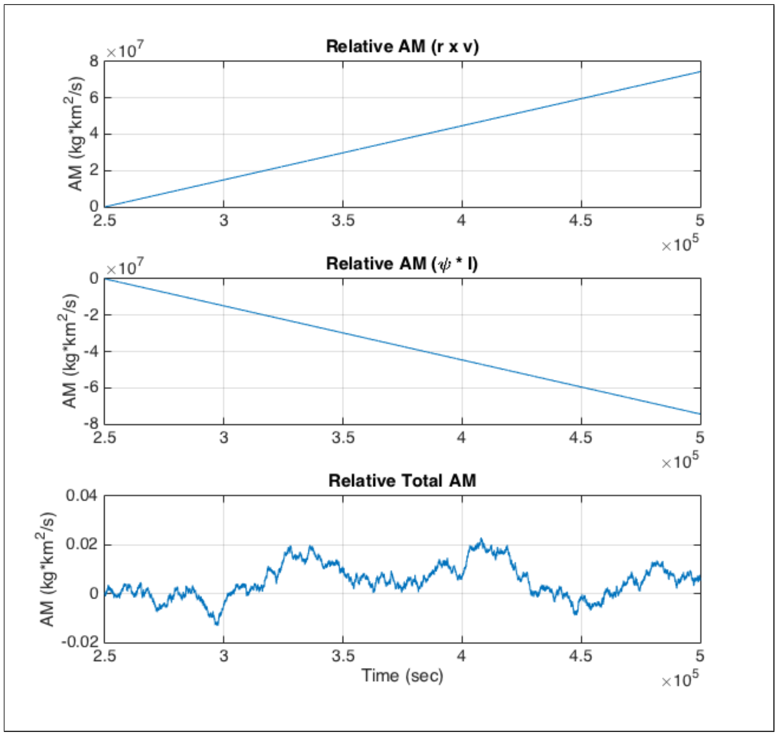

Figure 5.31: Changes in angular momentum relative to the system starting at 250,000 seconds for the simulation of the LR to ER transition. Top: Orbital angular momentum. Middle: Body-Centered rotational angular momentum. Bottom: Combined system angular momentum (Top + Middle).

forces are not significantly affecting the overall angular momentum of the system. This is expected as tidal torques conserve the angular momentum of the system and only dissipate energy.

Even though all collisions have subsided, tidal forces should be decaying the excess mechanical energy until the system reaches a tidally locked Euler Resting configuration. When the simulation ends, the system possesses an energy of $-9.2608 \cdot 10^{13}$ $[J]$ compared to the analytical ground state energy of $-4.10298 \cdot 10^{14}$ $[J]$ for an Euler Resting configuration (taking $\bar{H}^2 = 5.204$, the angular momentum of the system when the simulation terminates). This excess energy is stored in the rotational kinetic energy of the system. Although the tidal torque will be decreasing the rotational energy of the system, the equivalent tidal force will be increasing the kinetic energy of the system. In order for the bodies to reach a tidally locked state, the total energy of the system must be decreasing. By looking at the change of energy for the system over the remaining 250,000 seconds in Figure 5.32, we see that the system is indeed experiencing a net loss in energy.

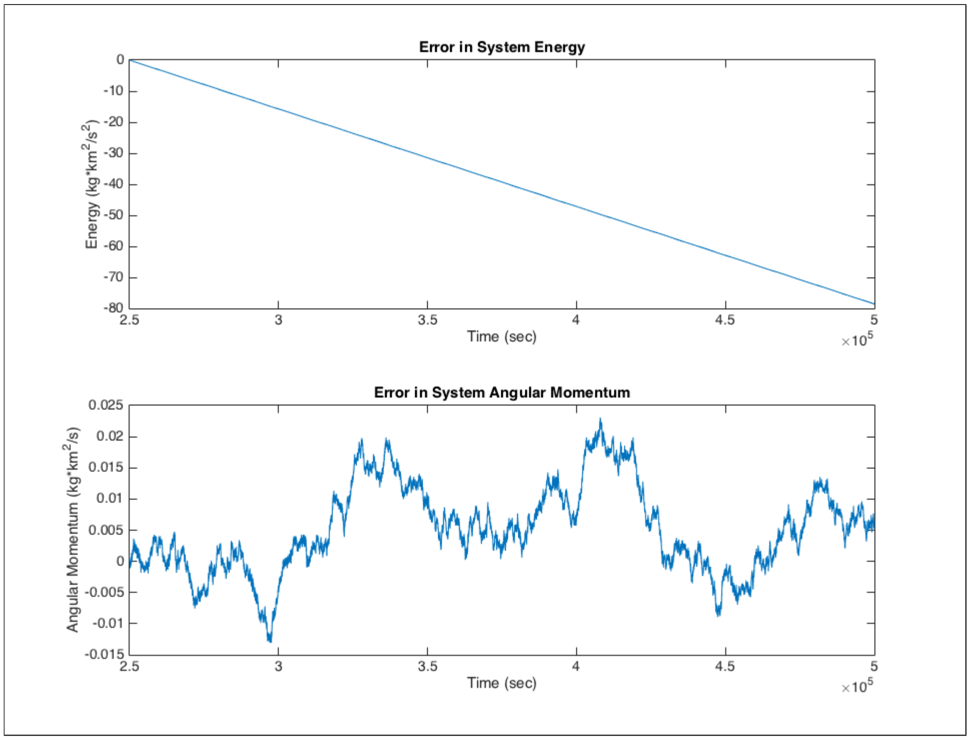

Figure 5.32: Net change in energy and angular momentum of the system starting at 250,000 seconds for the simulation of the LR to ER transition. "Error" in total system energy is actually the expected deviation in energy here.

The energy of the system is decaying at a near constant linear rate. From the graph, we can approximate the rate of energy decay as $\dot{E} = -0.31428 \cdot 10^{-4}$ $[kg \cdot km^2/s^3]$ or $\dot{E} = -314.28$ $[W]$. Compare this to the approximate analytical rate of energy decay:

$$\dot{E}_{pred.} = -\Gamma(\dot{\psi} - \dot{\theta}) \tag{5.3}$$

Where $\Gamma =$ is the tidal torque, $\dot{\psi}$ is the rotation rate of the Parent body, and $\dot{\theta}$ is the orbital rate of the Child body. Note that Γ remains fairly constant as it varies only with the sign of $\dot{\phi}$ (always positive here) and the relative displacement between bodies (constant other than a roughly 6% periodic change in r_{12}). Because there are a total of 6 tidal torques/forces present in the system (2 between each pair of bodies), we must calculate $\dot{E}$ for each applied tidal torque and sum them together.

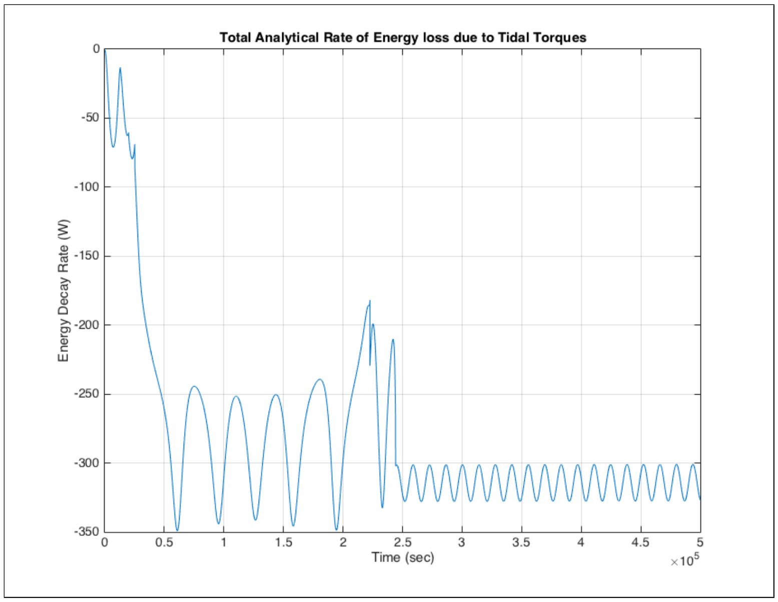

Figure 5.33: Rate of Energy decay due to Tidal Torques.

According to Figure 5.33, the rate of energy decay for the last 250,000 seconds oscillates around a mean value of $\dot{E} = -314.2\ W$. Comparing this with the analytical rate of energy decay of -314.28 $[W]$, we see this the two results agree very well, with an error of 0.025%. This result is not surprising as we've previously showed that applying the calculated tidal torque and equivalent tidal force will cause a decrease in energy at the same rate as the analytical prediction.

However, we cannot directly use our calculated value of $\dot{E}$ to find the time τ_{tidal} required for the bodies to become tidally locked. To see why, we must look at the equation for $\dot{E}$:

$$\dot{E} = -\Gamma(\dot{\phi}) \tag{5.4}$$

Although Γ will remain fairly constant over the entire evolution, $\dot{\phi}$ is gradually becoming smaller as the tidal torque acts to synchronize the rotation rates. Thus, $\dot{\phi}$ is a function of time. To solve this problem, we would need to solve the integral:

$$\Delta E = -\Gamma \int_{t_0}^{\tau_{tidal}} \dot{\phi}(t)\, dt \tag{5.5}$$

It would be possible to derive an expression for $\dot{\phi}(t)$ given that we know how the tidal torque Γ will affect the orbital rate $\dot{\theta}$ and rotation rate $\dot{\psi}$ of the bodies. However there is a much simpler way: the angular acceleration of the bodies $\ddot{\psi}$ will be roughly a constant since $\ddot{\psi}_k = -\Gamma_k/I$, where I is the moment of inertia of the body and Γ_k is the sum of the tidal toques acting a body k. Assuming a constant deceleration $\ddot{\psi}_k$, we can easily calculate the tidal locking time τ_{tidal} for each body as follows:

$$\tau_{tidal,k} = \frac{\Delta\dot{\psi}_k}{\ddot{\psi}} \tag{5.6}$$

Where $\Delta\dot{\psi}_k = \dot{\psi}_{req} - \dot{\psi}_k(t)$ is the difference in rotation rate of body k relative to the required spin rate of the tidally locked Euler Resting configuration. For a Euler Resting configuration with $\bar{H}^2 = 5.204$, the required rotation rate for a tidally locked system is $\dot{\psi}_{req} = 2.62206(10^{-4})$ $[rad/s]$. Based on these equations, the tidal lock time for each body is given below in Table 5.3:

Table 5.3: Time for Tidal Locking: LR to ER

	Body 1	Body 2	Body 3
$\Delta\dot{\psi}$ $[rad/s]$	$-2.01285(10^{-4})$	$-2.01163(10^{-4})$	$-2.00971(10^{-4})$
$\ddot{\psi}$ $[rad/s^2]$	$-3.32766(10^{-15})$	$-3.32767(10^{-15})$	$-6.55193(10^{-15})$
τ_{tidal} $[yrs]$	1918.1	1916.9	972.7

The timescale of this process is slightly below the expected range for tidal forces to synchronize rotational and orbital rates of bodies. Typical tidal locking timescales for a heterogenous ternary system range from 10^6 to 10^7 years [3]. To account for the differences in timescales, we can reason factors that would shorten the calculated time: most importantly, the initial rotation rate of the bodies $\dot{\psi}$ was fairly close to the required spin rate $\dot{\phi}_{req}$ of the tidally locked state and didn't need to undergo drastic changes. Second, the multiple inelastic collisions dissipated about 5.3% of the initial excess energy. The energy dissipated thru these collisions sped the process up by 5 - 6 years. Finally, the symmetry of bodies and their rotation rates means that they all experience near-identical tidal torque effects. The combined tidal torques were acting synchronously to slow the rotation rates of all bodies while increasing their orbital rates, so there were no competing tidal effects to delay this process.

Overall, the simulation clearly shows the bodies transition from a Lagrange

Resting configuration to an Euler Resting configuration. The trajectory of the bodies involved six collisions before coming to steady-state persistent contact. During the transition, two bodies remained in contact while orbiting a third body to form a quasi-Aligned Mixed configuration. Once all bodies were in persistent contact, the two outer bodies rolled along the center body at slowly dampening oscillations. Tidal torques were shown to decay excess mechanical energy in the system and began to synchronize the orbital rates of the bodies with their rotational rates. Finally, we were able to estimate the total time required for the bodies to reach a tidally locked Euler Resting configuration.

5.3.2 Euler Resting to Lagrange Resting

The next tested transition is the reverse scenario: the transit of the bodies from the Euler Resting configuration to the Lagrange Resting configuration. The Euler Resting configuration is the minimum energy configuration for values of angular momentum between $2.99 < \bar{H}^2 < 5.65907$. The energetic stability of the Euler Resting configuration extends from the range $1.98375 < \bar{H}^2 < 6.6125$; for any lower value of $\bar{H}^2$, the centrifugal forces acting on the bodies will not be enough to overcome gravity. In this scenario, the two outer bodies will roll along the center body and form variable angle V-Resting configurations until finally collapsing into a Lagrange Resting configuration.

The system is initialized with an angular momentum of $\bar{H}^2 = 1.8$. The position of body 2 is perturbed by a displacement $\delta x = d(10^{-3})$ in the positive X direction.

We use canonical units, such that $d = 2$. Given this displacement, the updated system angular momentum is displaced to $\bar{H}^2 = 1.8015$.

The initial positions $\vec{r}_i$ and initial body rotation angles ψ_i for each body are specified as:

$$\vec{r}_1 = \begin{bmatrix} 0 \\ 0 \\ 0 \end{bmatrix} \qquad \vec{r}_2 = \begin{bmatrix} d + \delta x \\ 0 \\ 0 \end{bmatrix} \qquad \vec{r}_3 = \begin{bmatrix} -d \\ 0 \\ 0 \end{bmatrix}$$

$$\psi_1 = 0 \qquad \psi_2 = 0 \qquad \psi_3 = 0$$

The simulation parameters are shown below in Table 5.4:

Table 5.4: ER to LR Simulation Parameters

Error Tolerance	ϵ	10^{-6}
Initial Step Size	h_0	10^{-2} $[TU]$
Simulation Duration	t_{end}	$500,000[s]$

Almost immediately, the displaced body 2 makes contact with the center body 1. All three bodies rotate in the unstable Euler Resting configuration for the next 80,000 seconds. Around $t = 81,000$ seconds, the two outer bodies 2 and 3 begin to roll towards each other to form varying angle V-Resting configurations. Then at $t = 109,100$ seconds, bodies 2 and 3 collide hard to form for the first time a Lagrange Resting configuration. The impact of the initial collision, causes body 1

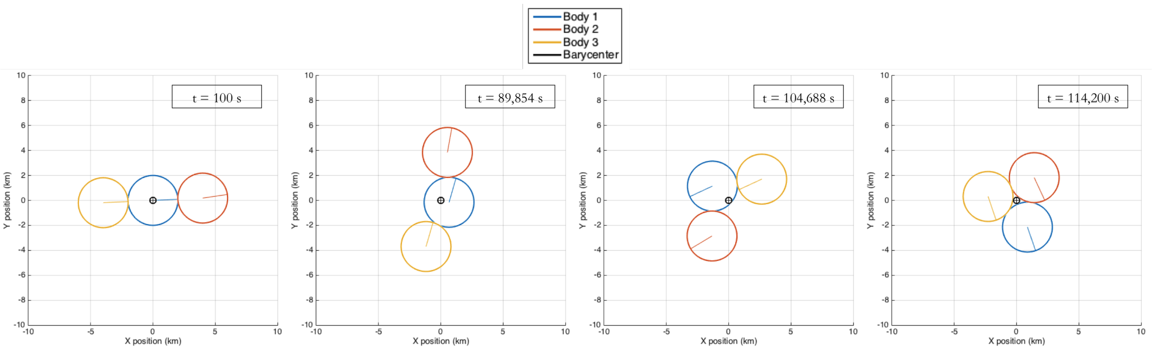

Figure 5.34: Euler Resting Configuration transitioning to Lagrange Resting Configuration. Each frame shows the orientation of the bodies and their body rotation angle at a specific time.

to temporarily break contact with the other two bodies but quickly comes back into a persistent contact. These events are obvious by looking at the inelastic collision energy losses for the first 120,000 seconds in Figure 5.36.

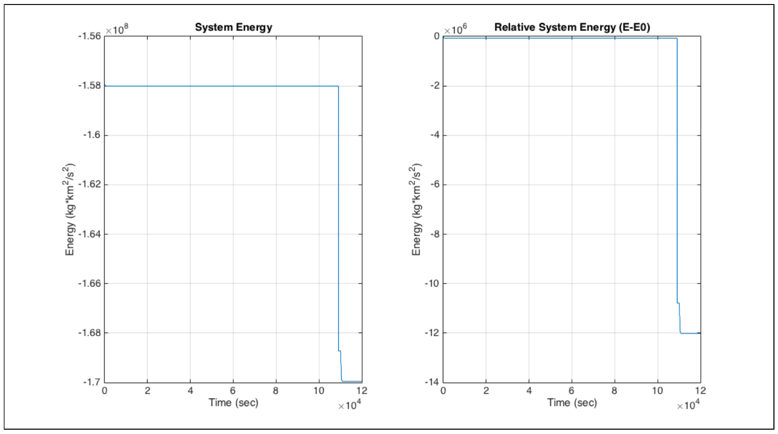

Figure 5.35: Left: Total energy of system for first 120,000 seconds of the simulation for the ER to LR transition. Right: Relative change in energy since start of simulation.

From the time $t = 110,800$ seconds to the end of the simulation, all three bodies remain in a persistent contact with each other. We can visualize these events by looking the the plot of relative positions between body pairs.

All collisions cease beyond 110,800 seconds. The nominal form factor angle

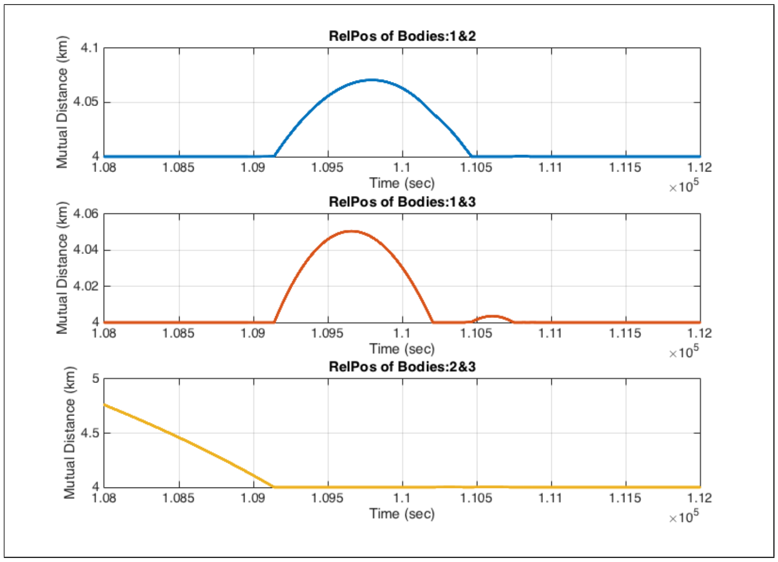

Figure 5.36: Relative body positions showing mutual body distances over the simulation for the transit of the bodies from ER to LR configuration. Notice the subsequent separation events after the impact of bodies 2 and 3. Note that the radius of each body is 2 km.

$F\theta$ for the Lagrange Resting configuration is 60 degrees which is the angle between the unit vector connecting the center of any one body to the centers of the other two. Although we can show numerically that the bodies achieve this exact form factor angle after 110,800 seconds, it serves as an example that the bodies must take on this angle in order for all three bodies to be in mutual contact. Indeed, all three bodies are in contact after 110,800 seconds so they are in the correct relative positions to form the Lagrange Resting configuration. All that remains is to show that the tidal forces are working to synchronize the orbital and rotation rates of the bodies.

We can see in Figure 5.37 that once the bodies reach the nominal Lagrange Resting orientation at $t = 110,800$ seconds, the relative body spin rate $\dot{\phi}$ between bodies pairs is approximately $-1.539 \cdot 10^{-4}$ $[rad/s]$. A negative $\dot{\phi}$ indicates that the orbital rate $\dot{\theta}$ of the bodies about the barycenter is greater than the rotation rate $\dot{\psi}$ of the bodies. As such, a tidal torque Γ will be applied to the bodies to increase their rotation rate while an equivalent tidal force F_Γ will work to decrease the orbital velocity of the bodies. Indeed, this is the trend observed by looking the two components of angular momentum for the second half of the simulation 5.38. The component of angular momentum derived from the orbital velocity about the barycenter (top plot of Figure 5.38) is decreasing while the component of angular momentum derived from the rotation of each body about its spin axis (middle plot of Figure 5.38) is increasing. Furthermore, the bottom plot of total angular momentum, which is the sum of the middle and top plots, indicates that the effects of these tidal forces are not significantly affecting the overall angular momentum of the system.

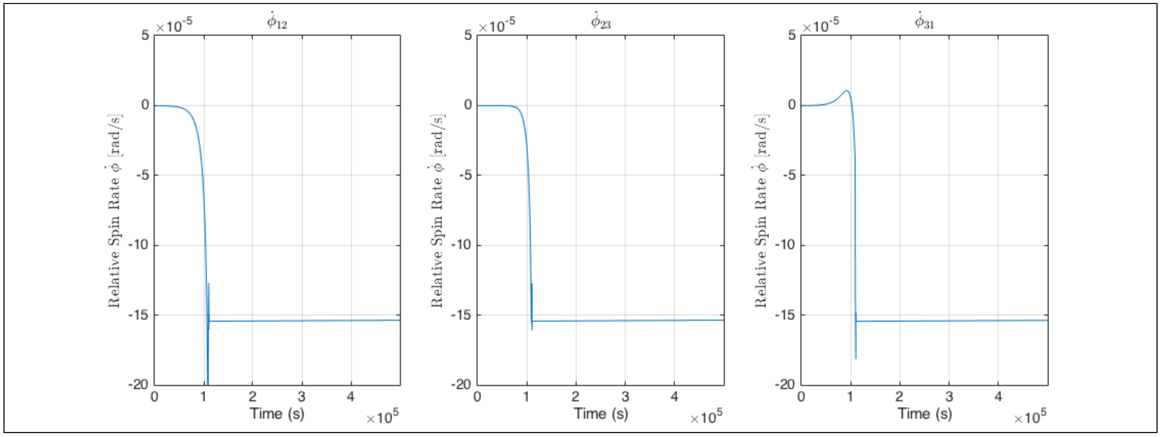

Figure 5.37: Relative body spin rate during the simulation of the Euler Resting to Lagrange Resting transition.

Finally, we can show that the tidal forces are decaying excess energy in the system and estimate the time for the system to reach a tidally locked Lagrange Resting state. When the simulation ends, the system possesses an energy of $-1.69979\,\cdot$

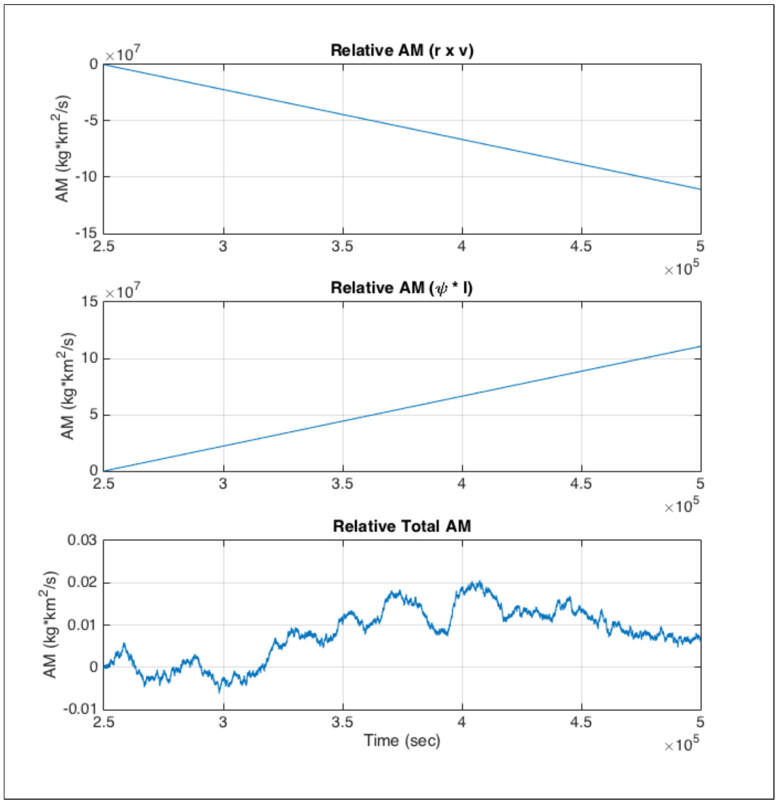

Figure 5.38: Changes in angular momentum relative to the system starting at 250,000 seconds for the simulation of the Euler Resting to Lagrange Resting configuration. Top: Orbital angular momentum. Middle: Body-Centered rotational angular momentum. Bottom: Combined system angular momentum (Top + Bottom).

10^{14} $[J]$ compared to the analytical ground state energy of $-6.91603 \cdot 10^{14}$ $[J]$ for an Euler Resting configuration (taking $\bar{H}^2 = 1.80157$, the angular momentum of the system when the simulation terminates). This excess energy is stored in the orbital energy of the system. The tidal torque will be increasing the rotational energy of the system while the equivalent tidal force will be decreasing the translational kinetic energy of the system. By looking at the change of energy for the system over the remaining 250,000 seconds in Figure 5.39, we see that the system is indeed experiencing a net loss in energy.

The energy of the system is decaying at a near constant linear rate. From

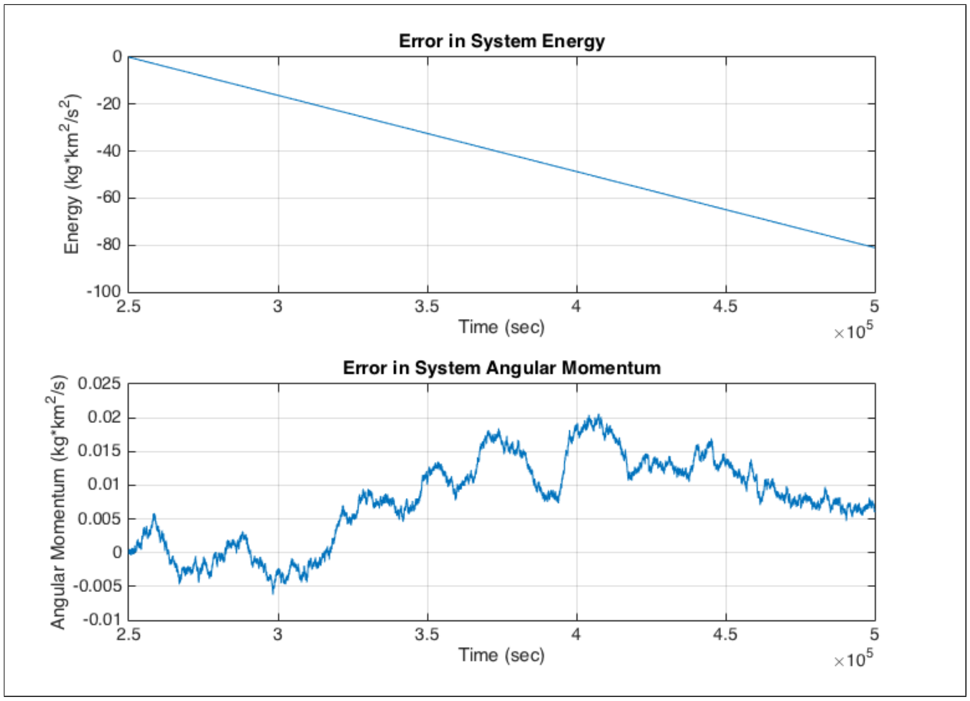

Figure 5.39: Net change in energy and angular momentum relative to the system at 250,000 seconds for the simulation of the ER to LR transition.

Figure 5.39, we can approximate the rate of energy decay as $\dot{E} = -.32432 \cdot 10^{-4}$ $[kg \cdot km^2/s^3]$ or $\dot{E} = -324.32$ $[W]$. Compare this to the approximate analytical rate of energy decay $\dot{E}_{pred.} = -323.9$ $[W]$ in Figure 5.40, we see that the two quantities are in good agreement.

To calculate the time required for tidal locking to occur for each body, we look at the angular acceleration of each body and change in spin rate necessary to match the required spin rate. For a Lagrange Resting configuration with $\bar{H}^2 = 1.80157$, the required rotation rate for a tidally locked system is $\dot{\psi}_{req} = 2.72923(10^{-4})$ $[rad/s]$. Based on these equations, the tidal lock time for each body is given below in Table 5.5:

The timescale for tidal locking to occur for the reverse transition (compared to

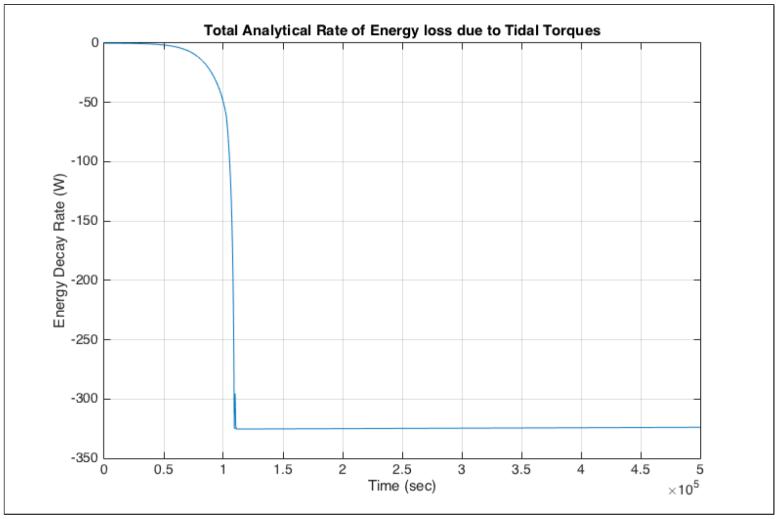

Figure 5.40: Rate of Energy decay due to Tidal Torques.

Table 5.5: Time for Tidal Locking: ER to LR

	Body 1	Body 2	Body 3
$\Delta\dot{\psi}\ [rad/s]$	$1.18165(10^{-4})$	$1.18099(10^{-4})$	$1.18237(10^{-4})$
$\ddot{\psi}\ [rad/s^2]$	$6.552(10^{-15})$	$6.552(10^{-15})$	$6.552(10^{-15})$
$\tau_{tidal}\ [yrs]$	571.89	571.57	572.24

the LR to ER case) is about an order of magnitude smaller. Again, this is because the bodies were initially rotating at rate similar to the required rotation rate of the tidally locked system. It seems that the tidal locking time for the transition between minimum energy configurations is orders of magnitude less than that for arbitrary systems. As a minimum energy configuration crosses the stability threshold in terms of $\bar{H}^2$, its previous synchronous rotation rate is very close to the synchronous rotation rate of the new minimum energy configuration.

Overall, the simulation provided a clear pathway for which the bodies transition from a Euler Resting configuration to an Lagrange Resting configuration. The trajectory of the bodies was fairly intuitive and involved one major collision event followed by a few small reactionary collisions. During the transition, the two outer bodies rolled along the surface of the center body to form quasi-V-Resting configurations before slamming into each other. Once all bodies were in persistent contact, all bodies rotated at nearly the same rate. Tidal torques were shown to decay excess mechanical energy in the system and began to synchronize the orbital rates of the bodies with their rotational rates. Finally, we were able to estimate the total time required for the bodies to reach a tidally locked Euler Resting configuration.

5.3.3 Euler Resting Transition to Aligned Mixed

For the next test, we will examine the transition from a Euler Resting Configuration to an Aligned Mixed configuration. The Euler Resting configuration is the minimum energy configuration for values of angular momentum between $2.99 < \bar{H}^2 < 5.65907$. The energetic stability of the Euler Resting configuration extends from the range $1.98375 < \bar{H}^2 < 6.6125$; for any higher value of $\bar{H}^2$, the centrifugal forces acting on the bodies will overcome gravity. The bodies will initially separate and transition into an unstable Euler Orbiting configuration. Eventually, the center body and one of the outer bodies in the Euler Orbiting configuration will come in contact while the remaining outer body orbits the contact pair at a distance.

The system is initialized with an angular momentum of $\bar{H}^2 = 6.7$. The position of body 2 is perturbed by a displacement $\delta x = d(10^{-3})$ in the positive X direction. We use canonical units, such that $d = 2$. Given this displacement, the updated system angular momentum is displaced to $\bar{H}^2 = 6.7058$.

The initial positions $\vec{r}_i$ and initial body rotation angles ψ_i for each body are specified as:

$$\vec{r}_1 = \begin{bmatrix} 0 \\ 0 \\ 0 \end{bmatrix} \qquad \vec{r}_2 = \begin{bmatrix} d + \delta d \\ 0 \\ 0 \end{bmatrix} \qquad \vec{r}_3 = \begin{bmatrix} -d \\ 0 \\ 0 \end{bmatrix}$$

$$\psi_1 = 0 \qquad \psi_2 = 0 \qquad \psi_3 = 0$$

The simulation parameters are shown below in Table 5.6:

Table 5.6: ER to AM Simulation Parameters

Error Tolerance	ϵ	10^{-6}
Initial Step Size	h_0	10^{-2} $[TU]$
Simulation Duration	t_{end}	$2,000,000[s]$

The outer bodies 2 and 3 immediately separate from the center body 1 and the bodies remain in an unstable Euler Orbiting configuration for 8,898 seconds. After this purely orbital period, bodies 1 and 3 rejoin to form a persistent contact while body 2 is now isolated and orbiting the contact body pair at a distance. This is the one and only collision event for the entire duration of the simulation. For the remaining 1.991 million seconds, all three bodies continue to tumble freely in space with seemingly chaotic behavior. Comparatively, this transitioning configuration

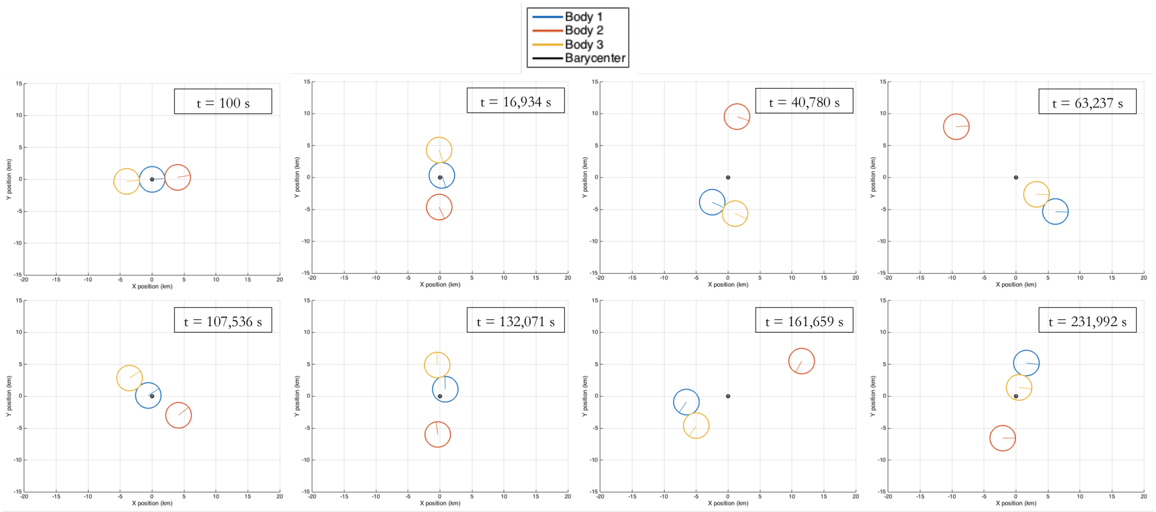

Figure 5.41: Euler Resting Configuration transitioning to Aligned Mixed Configuration. Each frame shows the orientation of the bodies and their body rotation angle at a specific time.

has fewer physical constraints than the other transitional cases and as such, does not readily conform to any identifiable equilibrium configuration. For instance, we would like to know which of the two in-contact bodies (1 and 3) will ultimately reside closer to the barycenter and which will face away from the barycenter. But the bodies have not settled enough to make a clear conclusion. For instance, looking at Figure 5.42, we see that the respective relative distances between the contact pair bodies (1 and 3) and the isolated body 2 jump around wildly; there is no clear evidence which body of the contact pair will ultimately lie closer to body 2 and which will lie further away. In order to discern this information, we would need to run the simulation longer to allow energy in the system to further dissipate and stop the contact pair from tumbling over each other.

Despite the tumbling of the contact pair, we would still like to assess the likeness of the configuration to the intended Aligned Mixed configuration. We can

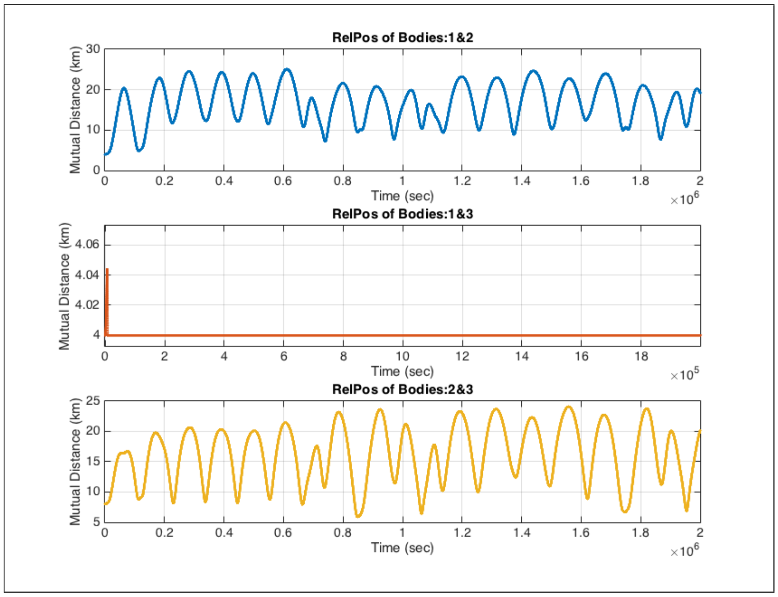

Figure 5.42: Relative distance between bodies over the simulation for the ER to AM transition. Note that the radius of each body is 2 km.

define the form factor angle $F\theta$ to be the angle between vectors connecting the center of the isolated body 2 to the centers of the two in-contact bodies 1 and 3. Here, we calculate this angle as:

$$F\theta = \cos^{-1}\left(\frac{\vec{r}_{21} \cdot \vec{r}_{23}}{|\vec{r}_{21}|\ |\vec{r}_{23}|}\right) \tag{5.7}$$

The notional form factor angle for a tidally locked Aligned Mixed configuration is $F\theta = 0°$. From Figure 5.43, we see that the measured form factor angle bounces around between 0° and 23°. Again, there is no clear indication that the bodies are becoming aligned to form an Aligned Mixed configuration.

However, we do not need to show a visual alignment of the bodies to know whether the system will reach an Aligned Mixed configuration. As long as the system is dissipating energy through tidal forces, then the system will be eventually

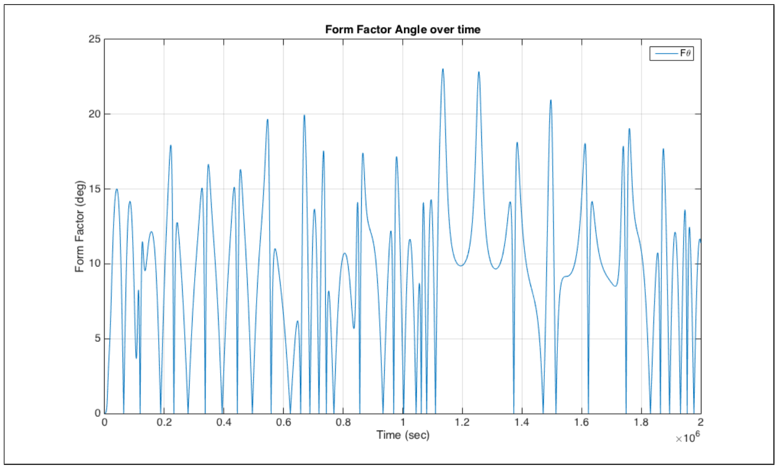

Figure 5.43: Relative body positions showing mutual body distances over the simulation of the ER to AM transition. Note that the radius of each body is 2 km.

forced into the only energetically stable configuration available, which is the Aligned Mixed configuration. From inspection of the positive relative body spin rates in Figure 5.44, we know that the tidal torques will decrease the rotation rate of the bodies while increasing their orbital rate about the barycenter. Indeed, this is the trend observed by looking the two components of angular momentum for the second half of the simulation in Figure 5.45. The component of angular momentum derived from the orbital velocity about the barycenter (top plot of Figure 5.45) is increasing while the component of angular momentum derived from the rotation of each body about its spin axis (middle plot of Figure 5.45) is decreasing. Furthermore, the bottom plot of total angular momentum, which is the sum of the middle and top plots, indicates that the effects of these tidal forces are not significantly affecting the overall angular momentum of the system.

Unlike the previously tested cases, one of the bodies (body 2) is in a physically unconstrained orbit about the other bodies. This condition allows the equivalent

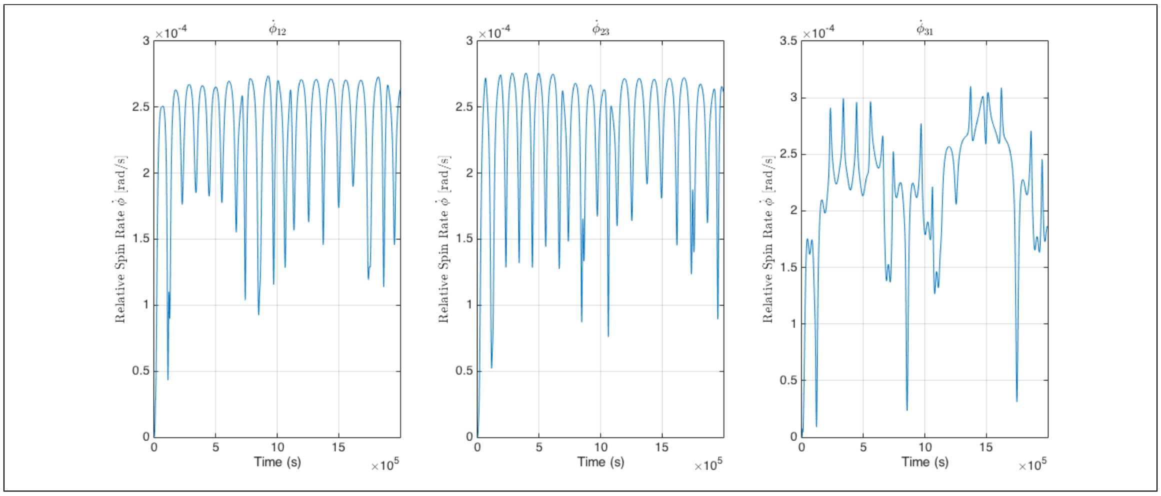

Figure 5.44: Relative body spin rate for the simulation of the Euler Resting to Aligned Mixed transition.

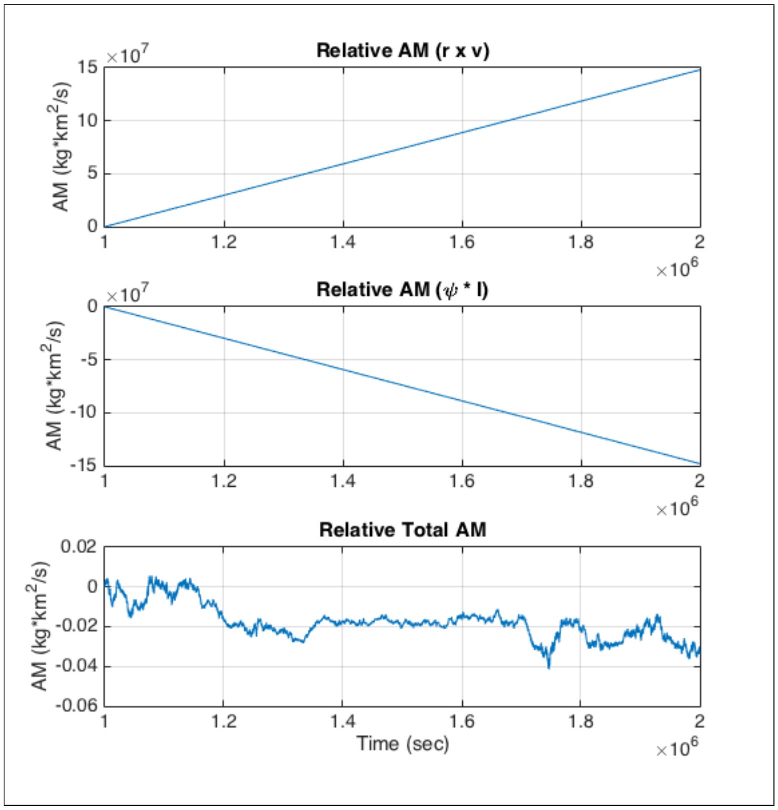

Figure 5.45: Changes in angular momentum relative to the system starting at 1,000,000 seconds for the simulation of the Euler Resting to Aligned Mixed transition. Top: Orbital angular momentum. Middle: Body-Centered rotational angular momentum. Bottom: Combined system angular momentum (Top + Bottom).

tidal force F_Γ acting on the unconstrained body to raise or lower the semi-major axis of the orbiting body.

Finally, we can show that the tidal forces are decaying excess energy in the system and estimate the time for the system to reach a tidally locked Aligned Mixed state. When the simulation ends, the system possesses an energy of $-7.82051 \cdot 10^{13}$ $[J]$ compared to the analytical ground state energy of $-3.645536 \cdot 10^{14}$ $[J]$ for an Aligned Mixed configuration (taking $\bar{H}^2 = 6.7058$, the angular momentum of the system when the simulation terminates). This excess energy is stored in the rotational kinetic energy of the bodies. The tidal torque will be decreasing the rotational energy of the system while the equivalent tidal force will be increasing the translational kinetic energy of the system. By looking at the change of energy for the system over the last 1,000,000 seconds in Figure 5.46, we see that the system is indeed experiencing a net loss in energy.

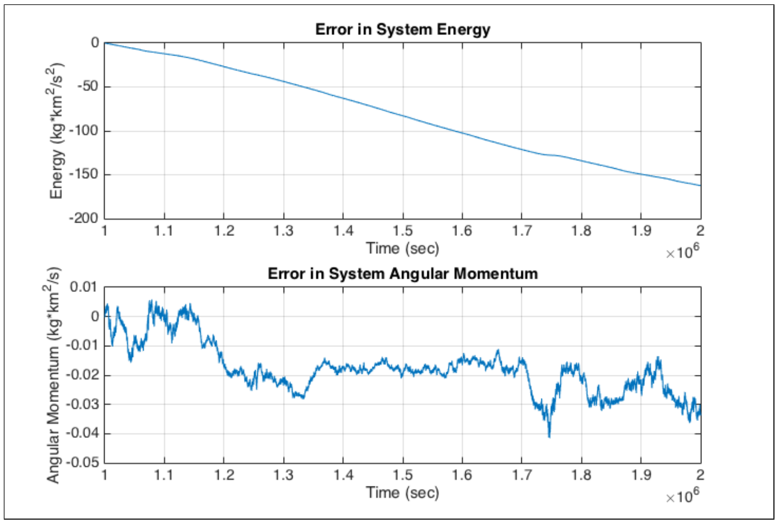

Figure 5.46: Net change in energy and angular momentum of the system starting at 1,000,000 seconds for the simulation from ER to AM transition.

Even though the contact pair is tumbling and the system hasn't reached stable configuration, the energy of the system is decaying at a near constant linear rate. From the graph, we can approximate the rate of energy decay as $\dot{E} = -1.624 \cdot 10^{-4}$ $[kg{\cdot}km^2/s^3]$ or $\dot{E} = -162.4$ $[W]$. Comparing this to the approximate analytical rate of energy decay $\dot{E}_{pred.} = -323.9$ $[W]$ in Figure 5.47 is not as straight forward because it is highly volatile due to the doubly changing relative distances between bodies and their mutual body spin rates $\dot{\phi}$. However, for sake of approximation, we can average the analytical $\dot{E}_{pred.}$ over the last 1,000,000 second interval. Doing so yields an average of $\dot{E}_{pred.} = -148.62$ $[W]$. Even with this loose approximation, we see that the two quantities are in good agreement.

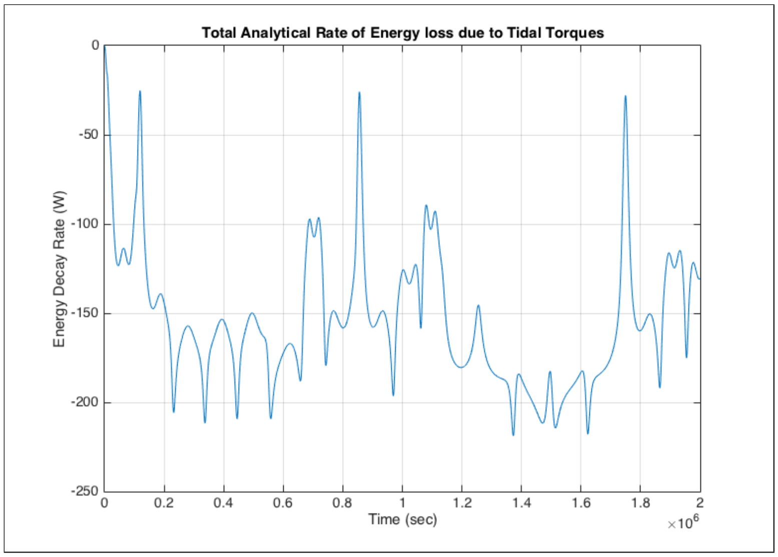

Figure 5.47: Rate of Energy decay due to Tidal Torques for the simulation of the ER to AM transition.

To calculate the time required for tidal locking to occur for each body, we look at the angular acceleration of each body and change in spin rate necessary to match the required spin rate. However, the angular acceleration for each body continues to fluctuate throughout the simulation, so we use the average angular acceleration over the last 1,000,000 seconds of the simulation. For an Aligned Mixed configuration with $\bar{H}^2 = 6.7058$, the required rotation rate for a tidally locked system is $\dot{\psi}_{req} = 4.07799(10^{-5})$ $[rad/s]$. Based on these equations, the tidal lock time for each body is given below in Table 5.7:

Table 5.7: Time for Tidal Locking: ER to AM

	Body 1	Body 2	Body 3
$\Delta\dot{\psi}$ $[rad/s]$	$-2.5535(10^{-4})$	$-2.5672(10^{-4})$	$-2.55357(10^{-4})$
$\ddot{\psi}$ $[rad/s^2]$	$-3.5538(10^{-15})$	$-2.1024(10^{-15})$	$-3.5675(10^{-15})$
τ_{tidal} $[yrs]$	2471.4	$1.7474(10^7)$	2471.6

As expected, the two contact pair bodies become tidally locked to each other in a significantly shorter amount of time. Bodies 2 and 3 remain significantly closer to one another and the resulting tidal torque, which varies by the relative displacement between bodies raised to the 6^{th} power, is nearly 2 orders of magnitude stronger. As a result, their mutual tidal torques synchronize the rotation of the bodies much faster than can done with the isolated orbiting body 2. In order for the entire system to reach a tidally locked state, all bodies need to be synchronized to the same rotation and orbital rates, so $\tau_{tidal,2}$ is the dominating factor. There are two main reasons for the large tidal locking time. First is that body 2 is further away from the other bodies - the resulting tidal torque is orders of magnitude smaller and unable to affect the rotation rates of bodies as effectively. Second, body 2 is physically unconstrained and the tumbling of the contact pair causes the affecting tidal torque to fluctuate around near 0 values.

Overall, the simulation provided a clear pathway for which the bodies transition from a Euler Resting configuration to an Aligned Mixed configuration. The initial transition between a Euler Resting configuration and quasi-Aligned Mixed was intuitive, but the resulting trajectory was seemingly chaotic in behavior. The bodies separated to form an unstable Euler Orbiting configuration before the center body and a outer body came together to form a persistent contact. During the transition, the contact pair tumbled freely and did not yet show signs of aligning to an Aligned Mixed configuration. The simulation would need to be run for longer durations to better determine which body of the contact pair would face inwards and which would face outwards. Tidal torques were shown to decay excess mechanical energy in the system and began to synchronize the orbital rates of the bodies with their rotational rates. Finally, we were able to estimate the total time required for the bodies to reach a tidally locked Aligned Mixed configuration.

5.3.4 Aligned Mixed to Euler Resting

The final case we test is the reverse transition from Aligned Mixed configuration to a Euler Resting configuration. The Aligned Mixed configuration continues its energetic stability down until $\bar{H}^2 = 5.32417$ at which point the bodies orbit too slow to maintain the configuration. Immediately below this point, the Euler Resting configuration is the only stable and thus the only minimum energy configuration available to the bodies. In this scenario, the isolated orbiting body will enter a trajectory that gradually spirals inwards until finally making a persistent contact with the innermost body of the body pair.

The Aligned Mixed configuration is initialized with normalized distance value of $R = 2.33696$, which equates to an angular momentum of $\bar{H}^2 = 5.32416$. The initial velocities of the bodies are adjusted to be consistent with a system of reduced $\bar{H}^2 = (1 - 10^{-3})\bar{H}_0^2$, where $\bar{H}_0^2 = 5.32416$ is the angular momentum of the initial configuration. We use canonical units, such that $d = 2$. Given this perturbation, the updated system angular momentum is displaced to $\bar{H}^2 = 5.3182$.

The initial positions $\vec{r}_i$ and initial body rotation angles ψ_i for each body are specified as:

$$\vec{r}_1 = \begin{bmatrix} -d/2 \\ 0 \\ 0 \end{bmatrix} \qquad \vec{r}_2 = \begin{bmatrix} d/2 \\ 0 \\ 0 \end{bmatrix} \qquad \vec{r}_3 = \begin{bmatrix} dR \\ 0 \\ 0 \end{bmatrix}$$

$$\psi_1 = 0 \qquad \psi_2 = 0 \qquad \psi_3 = 0$$

The simulation parameters are shown in Table 5.8.

Table 5.8: AM to ER Simulation Parameters

Error Tolerance	ϵ	10^{-6}
Initial Step Size	h_0	10^{-2} $[TU]$
Simulation Duration	t_{end}	$2,000,000[s]$

The isolated body 3 begins an inwards spiral trajectory towards the barycenter while keeping its body axis aligned with the centers of the body pair (bodies 1 and 2).

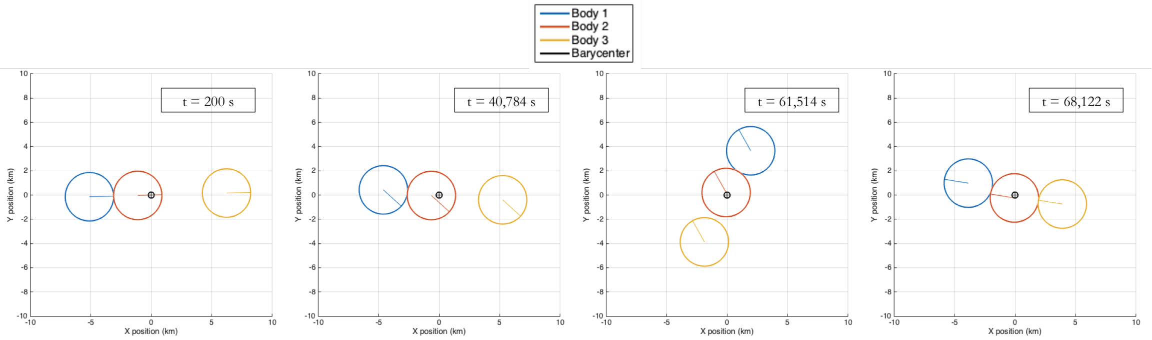

Figure 5.48: Aligned Mixed Configuration transitioning to Euler Resting Configuration. Each frame shows the orientation of the bodies and their body rotation angle at a specific time.

Equivalently, the body pair spirals inwards towards the barycenter while maintaining the initial relative alignment of body 2 facing inwards and body 1 facing outwards. At $t = 64,363$ seconds, the isolated body 3 collides with the inwards facing body 2 to form a quasi-Euler Resting configuration with body 2 as the center body. As expected for bodies of equal mass, the isolated body 3 translated radially twice the distance as body 1 and 2 before coming in contact. This collision event is easily captured by the drop in energy of the system as seen in Figure 5.49.

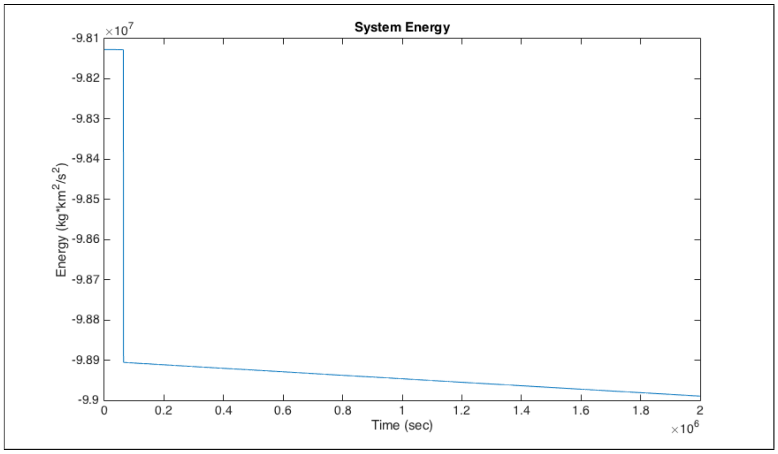

Figure 5.49: Energy of Aligned Mixed configuration as it transitions to a Euler Resting configuration.

After this time, all collisions cease and the two outer bodies 1 and 3 begin orbiting the center body 2 in a quasi-Euler Resting configuration. The two outer bodies roll along the surface of the center body 2 at a relatively high frequency and small oscillation peaks. If we examine the form factor angle for the Euler Resting configuration (ideal form factor angle $F\theta = 180°$), we see in Figure 5.50 that the bodies are nearly aligned with that of the ideal collinear Euler Resting configuration.

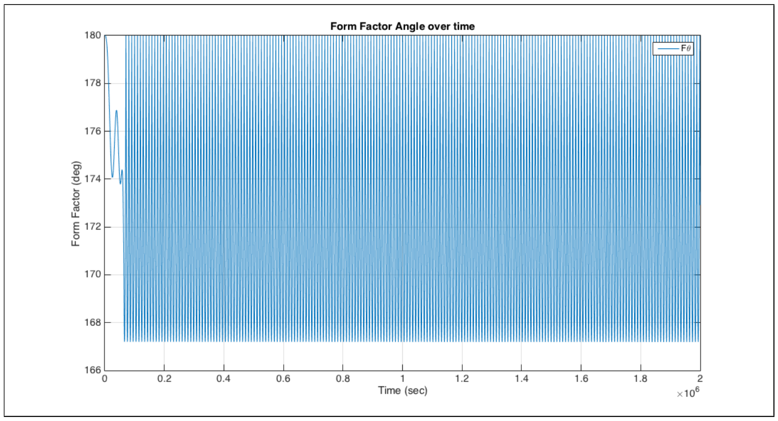

Figure 5.50: Form factor angle of the system for a Euler Resting configuration. Ideal FF angle is 180 degrees.

The oscillations of the outer bodies about the center body is representative of the excess mechanical energy that is in the system. Tidal forces will eventually decay this excess energy and synchronize the rotation rates of the bodies. Once the bodies reach the quasi-Euler Resting orientation at $t = 64,363$ seconds, the relative body spin rate $\dot{\phi}$ between bodies pairs is approximately $-1.463{\cdot}10^{-4}$ $[rad/s]$ as can be seen in Figure 5.51. A negative $\dot{\phi}$ indicates that the orbital rate $\dot{\theta}$ of the bodies about the barycenter is greater than the rotation rate $\dot{\psi}$ of the bodies. As such, a tidal torque Γ will be applied to the bodies to increase their rotation rate while an equivalent tidal force F_{Γ} will work to decrease the orbital velocity of the bodies. From the figure, we can already see $\dot{\phi}$ begin to approach 0. Indeed, this is the trend is further confirmed by looking at Figure 5.52 which shows the two components of angular momentum for the remainder of the simulation. The component of angular momentum derived from the orbital velocity about the barycenter (top plot of Figure 5.52) is decreasing while the component of angular momentum derived from the rotation of each body about its spin axis (middle plot of Figure 5.52) is increasing. The bottom plot of total angular momentum, which is the sum of the middle and top plots, indicates that the effects of these tidal forces are not significantly affecting the overall angular momentum of the system.

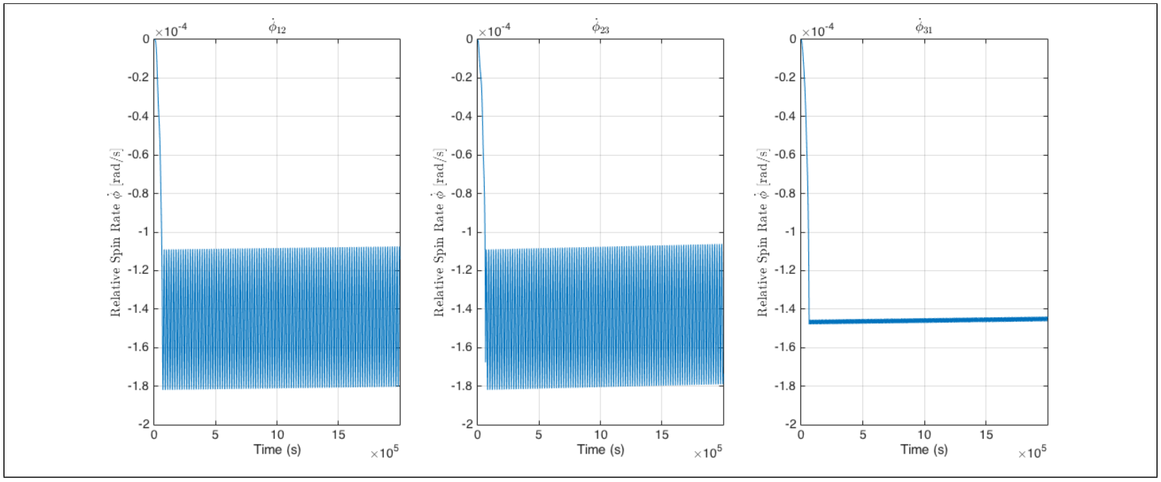

Figure 5.51: Relative body spin rate during the simulation of the AM to ER transition.

Finally, we can show that the tidal forces are decaying excess energy in the system and estimate the time for the system to reach a tidally locked Euler Resting state. When the simulation ends, the system possesses an energy of $-9.8989 \cdot 10^{13}$ $[J]$ compared to the analytical ground state energy of $-4.0937 \cdot 10^{14}$ $[J]$ for a Euler Resting configuration (taking $\bar{H}^2 = 5.3182$, the angular momentum of the system when the simulation terminates). This excess energy is stored in the orbital energy

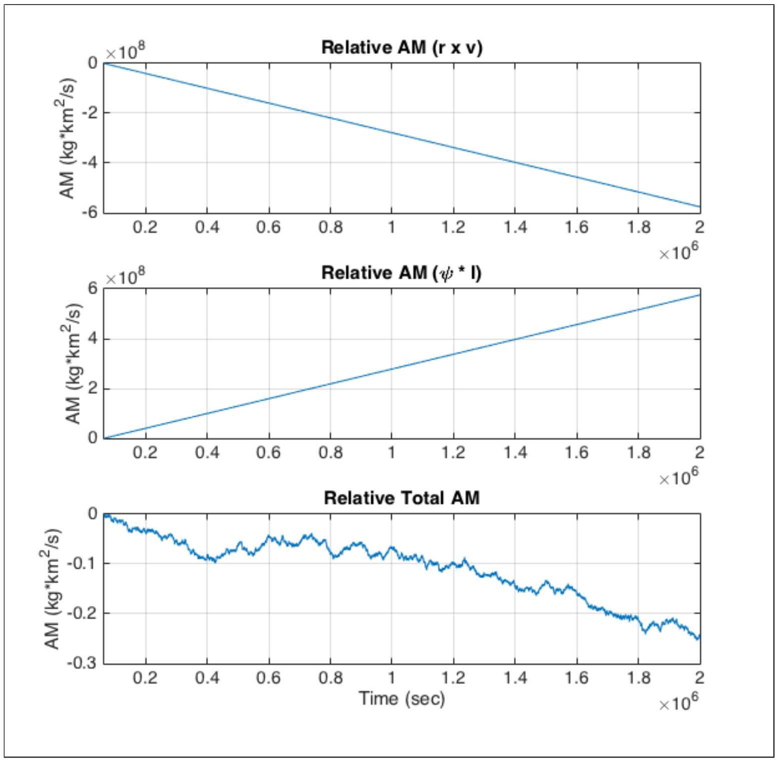

Figure 5.52: Changes in angular momentum relative to the system starting at 65,000 seconds for the simulation of the AM to ER transition. Top: Orbital angular momentum. Middle: Body-Centered rotational angular momentum. Bottom: Combined system angular momentum (Top + Bottom).

of the system. The tidal torque will be increasing the rotational energy of the system while the equivalent tidal force will be decreasing the translational kinetic energy of the system. By looking at the change of energy for the system over the remaining 1,935,000 seconds in Figure 5.53, we see that the system experiences a net loss in energy.

The energy of the system is decaying at a near constant linear rate over these timescales. From the graph, we can approximate the rate of energy decay as $\dot{E} = -2.0615 \cdot 10^{-4}\ [kg \cdot km^2/s^3]$ or $\dot{E} = -206.15\ [W]$. Compare this to the approximate analytical rate of energy decay $\dot{E}_{pred.} = -204.6\ [W]$, we see that the two quantities are in good agreement with an error of 0.76%.

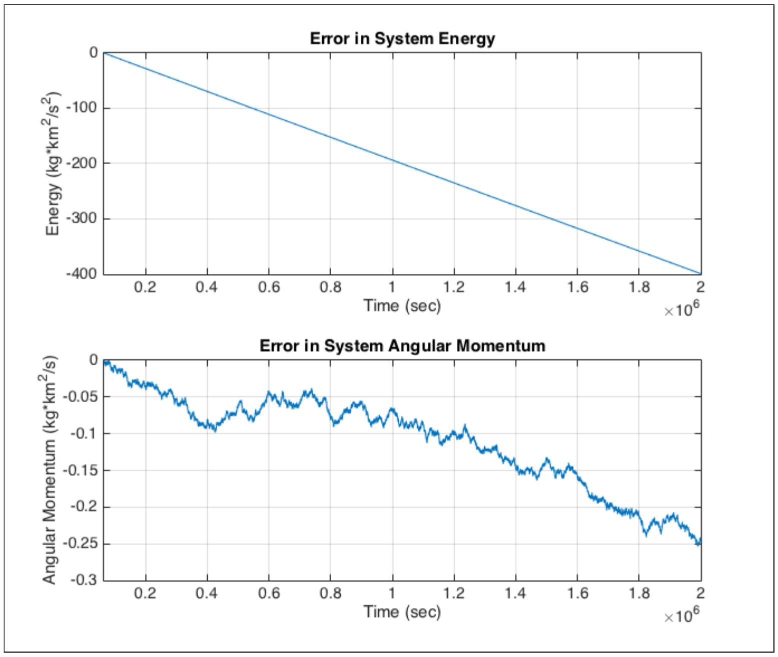

Figure 5.53: Net change in energy and angular momentum relative to the system at 65,000 seconds for the simulation of the AM to ER transition.

To calculate the time required for tidal locking to occur for each body, we look at the angular acceleration of each body and change in spin rate necessary to match the required spin rate. For an Euler Resting configuration with $\bar{H}^2 = 5.3182$, the required rotation rate for a tidally locked system is $\dot{\psi}_{req} = 2.62564(10^{-4})$ $[rad/s]$. Based on these equations, the tidal lock time for each body is given below in Table 5.9:

Table 5.9: Time for Tidal Locking: AM to ER

	Body 1	Body 2	Body 3
$\Delta\dot{\psi}$ $[rad/s]$	$1.2518(10^{-4})$	$1.2387(10^{-4})$	$1.2522(10^{-4})$
$\ddot{\psi}$ $[rad/s^2]$	$3.328(10^{-15})$	$6.552(10^{-15})$	$3.328(10^{-15})$
τ_{tidal} $[yrs]$	1192.86	599.49	1193.21

The timescale for tidal locking to occur for the reverse transition (compared to the ER to AM case) is 4 orders of magnitude smaller based on the longest time of each body to become tidally locked. Even though the two outer bodies have slight rolling oscillations along the center body surface, their relative distance is fairly constant, resulting in a near constant tidal torque term. All bodies are significantly closer to each other in the quasi-Euler Resting configuration compared to the quasi-Aligned Mixed configuration of the previous test, resulting in a significantly larger magnitude of the applied tidal torques on each body. These two effects result in a significantly shorter tidal locking time for all of the bodies. Once again, the tidal locking times are much shorter compared to an arbitrary ternary system due to the initial rotation rate of the bodies in the Aligned Mixed configuration being close to the required rotation rate of the tidally locked Euler Resting configuration.

Overall, the simulation provided a clear pathway for which the bodies transition from an Aligned Mixed configuration to a Euler Resting configuration. The trajectories of the bodies were fairly predictable as the isolate body and body pair spiraled inwards towards the barycenter until making contact. During the transition, the body pair maintained its initial alignment relative to the isolated body, such that we could predict that the initially inwards facing body of the body pair (body 2) would end as the center body of the Euler Resting configuration. Once all bodies were in persistent contact, the two outer bodies rolled along the surface of the center body with decaying oscillations. Tidal torques were shown to decay the excess mechanical energy in the rolling oscillations and began to synchronize the orbital rates of the bodies with their rotational rates. Finally, we were able to estimate the total time required for the bodies to reach a tidally locked Euler Resting configuration.

Chapter 6: Error Analysis

The accuracy of the presented results ultimately depend on the errors produced by the simulation, dynamic models, and propagator scheme. Each source of error has the potential to alter to the true state of the system, including errors in the position and velocity of the bodies, or changes to conserved quantities like energy and angular momentum. We wish to show that the errors identified in the simulation do not significantly alter the behavior or results of the system for the timescales we tested. The true state of the system is often ill-defined when the bodies undergo a transition because the dynamics describing the motion of the three bodies have no analytic solution. For these cases, we can only estimate the error in conserved quantities (energy and angular momentum) and the known error of the propagator. For static equilibrium configurations, we know that there should be no change to any of the body relative positions and velocities; thus we can take the initial state of the system to be the true state for comparison purposes.

There are three primary sources of errors that arise in the simulation that alter the bodies from their true states:

- Propagation tolerance & propagator accuracy
- Penetration of bodies in persistent contacts

- Repositioning of bodies during a collision event

6.1 Propagation Tolerance and Propagator Accuracy

Each error source affects the system in a measurable and predictable way. We will first examine the error caused by the propagator. A Velocity Verlet scheme is a second-order symplectic integrator. The local error of velocity per timestep is $O(\Delta t^2)$ and the local error of position is $O(\Delta t^4)$ [18]. The global error in position and velocity per timestep is $O(\Delta t^2)$. The timestep Δt is indirectly controlled by the propagation convergence tolerance ϵ that is set before running the simulation. ϵ is the maximum allowed difference between states using the Half-Step method. For all of the presented simulation results, a convergence tolerance of $\epsilon = 10^{-6}$ was used. This value of ϵ was the smallest value achievable that produced accurate results and reasonable computation times. For instance, reducing the tolerance to $\epsilon = 10^{-7}$ reduced the error in energy and angular momentum by an order of magnitude while increasing the simulation runtime from from 1 day to 10 days. With a convergence tolerance of $\epsilon = 10^{-6}$, the average timestep taken in all simulations was $\Delta t = 0.1$ seconds. Thus we should expect a local error in velocity of $O(10^{-2})$ and a local error in position of $O(10^{-4})$. We must look at the error in energy and angular momentum between timesteps to infer the error induced by the propagator. Energy depends inversely on the relative position of the bodies and on the velocity of the bodies to the second power. Based on the errors in position and velocity, we can expect a change in the total mechanical energy per timestep of about $O(10^{-2})$ without the effects of tidal torques and the contact spring damper. Similarly, we expect errors in angular momentum of $O(10^{-2})$. If we look at the change in energy and angular momentum for the static Lagrange Resting case in Figure 6.1, we see that local errors are much smaller and more in line with the propagator convergence tolerance ϵ; errors in energy are $O(10^{-6})$ and errors in angular momentum are $O(10^{-4})$.

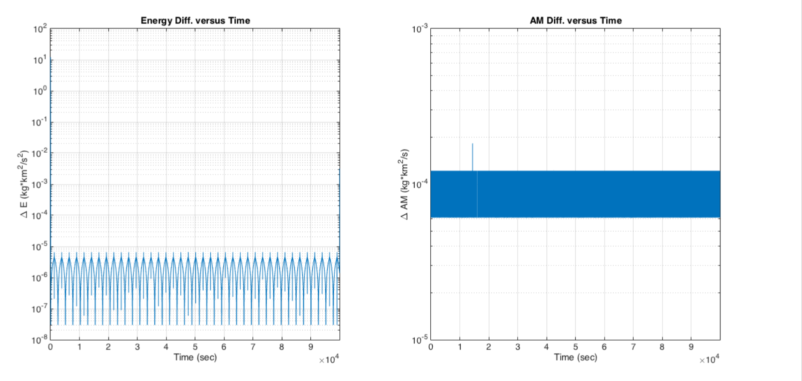

Figure 6.1: Change in energy and angular momentum between timesteps (left) and between iteration steps (right) for the static Lagrange Resting configuration simulation.

The discrepancy in error can be attributed to the spring forces used to the keep the bodies in contact that causes the bodies to oscillate about a fixed equilibrium. Indeed, we see that the errors in energy and angular momentum do not accumulate and seem to oscillate about a fixed value in Figure 6.2. This is the case for the static Aligned Mixed and Euler Resting cases as well.

Similarly, the errors in angular momentum for the transitioning case under the effects of tidal torques are small and bounded. If we look at error per timestep in angular momentum for the transition case going from a Euler Resting to Lagrange Resting configuration in Figure 6.3, we see that the local errors are $O(10^{-4})$. The local error in energy cannot be inferred from the figure because tidal torques are

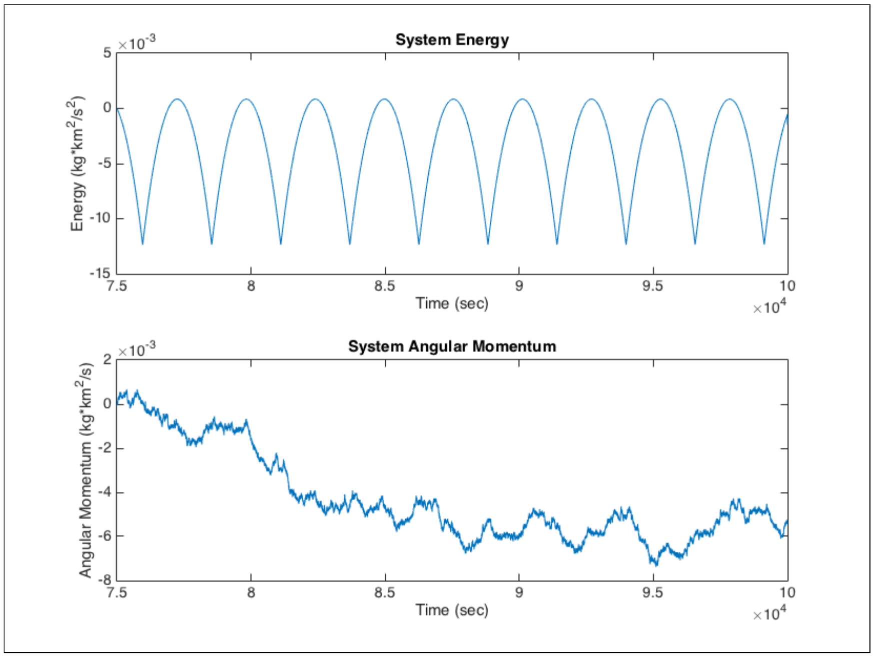

Figure 6.2: Energy and angular momentum over the last 25,000 seconds for the static Lagrange Resting configuration. Quantities are relative to the energy and angular momentum of the system at 75,000 seconds.

decaying energy from the system. However, we compared the analytic rate of tidal energy decay to the measured rate of energy decay in the system in the Results chapter and found that differences in rates were $O(10^{-3})$, which can be taken as a first-order approximation of the local error in energy.

Again, we can see in Figure 6.4 that these local errors in angular momentum do not accumulate in one direction and produce a global error of about $O(10^{-2})$. This global error is approximately equal to the expected global error in angular momentum based on the timestep used for the velocity verlet integrator.

The total energy of simulated systems is typically $O(10^7)$ and the total angular momentum is $O(10^{11})$. A global error in energy and angular momentum of $O^{-2})$ is insignificant and has a negligible affect on the macro behavior of the bodies. Thus the propagator and integrator errors are too small to have an impact on the results

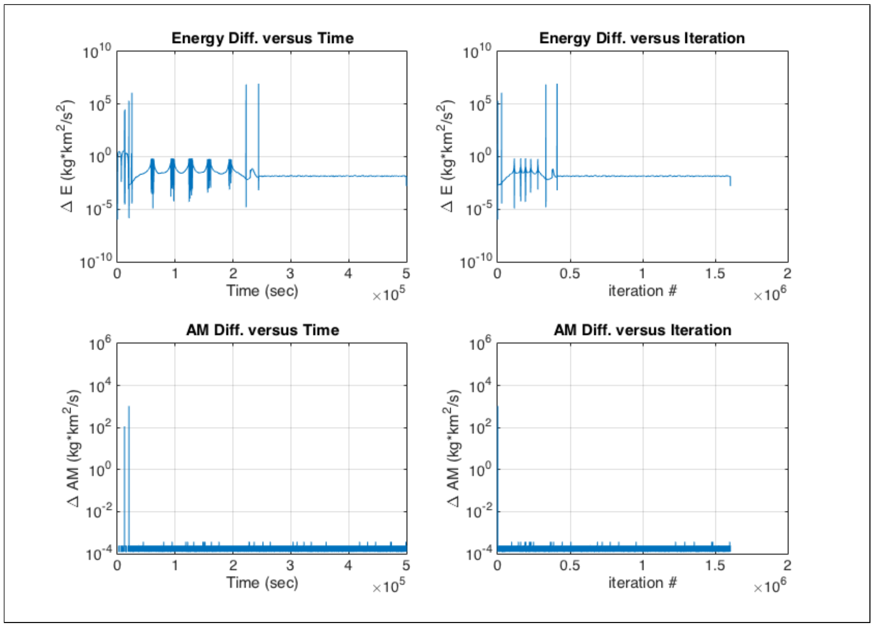

Figure 6.3: Change in energy and angular momentum between timesteps (left) and between iteration steps (right) for the Euler Resting to Lagrange Resting transition.

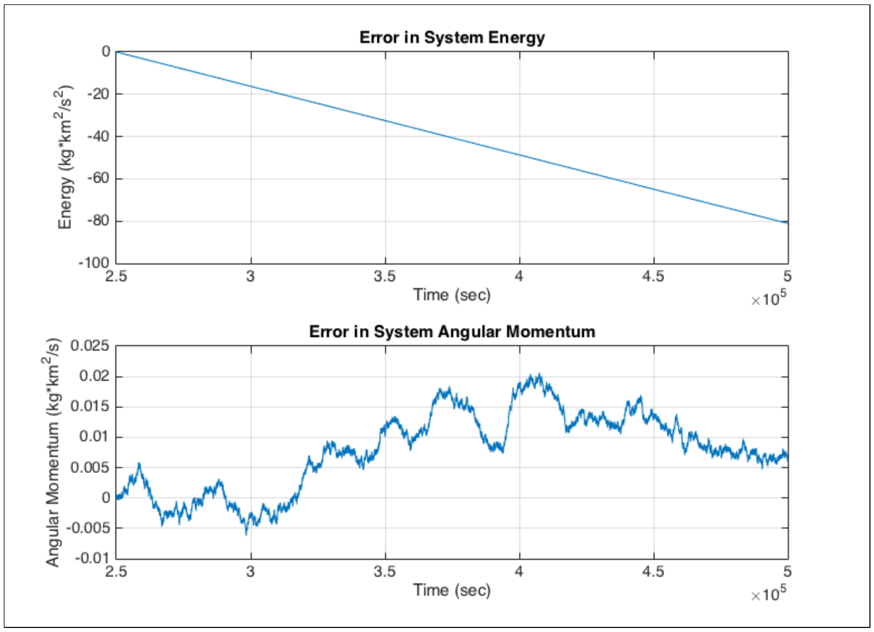

Figure 6.4: Energy and angular momentum over the last 250,000 seconds for the Euler Resting to Lagrange Resting transition. Quantities are relative to the energy and angular momentum of the system at 250,000 seconds.

of the simulation and we can disregard any result biases these errors introduced. If higher simulation accuracy was needed, then a higher order symplectic integrator or smaller convergence tolerance ϵ could be used at the cost of greatly increased computation time.

6.2 Penetration Error

The spring contact force model allows for a small penetration of the bodies surfaces which will change the resting energy point of the system. The equilibrium point for the contact springs is when the displacement between body surfaces is exactly 0. However, if the bodies are in perfect contact at their surfaces, then the contact force will evaluate to 0 but a gravitational force will pull the body centers together. At the next timestep, the bodies will have penetrated slightly and the contact forces will evaluate to a nonzero value and attempt to restore the displacement between the body surfaces to 0. This is a cyclic process that will continue for any persistent contact configuration.

The mean penetration distance is a function of the spring constants and mean timestep taken. For the static Lagrange Resting simulation, the mean penetration distance between bodies is approximately 1.5 mm. The incurred potential energy from this penetration decreases the energy of the system by 67 $[kg \cdot km^2/s^2]$, which accounts for less than $10^{-4}\%$ of the total energy of the system. Additionally, the oscillation of energy caused by the penetration is bounded by looking at the top plot of Figure 6.2. Similarly for the transition results, such as between a Euler Resting and Lagrange Resting configuration, we measure a similar mean penetration distance.

Overall, the energy of the system is not significantly affected by the small penetration distance in a way that alters the results of the simulations or the macroscopic behavior of the bodies. Using a smaller timestep would decrease the mean penetration distance and magnitude of the energy oscillations, but a 0 energy error cannot be realistically obtained with this propagator. Instead, an implicit integrator such as the SHAKE algorithm used for constrained dynamics could be used to guarantee that each propagation step obeys the physical constraint on the system to within a specified tolerance [5].

6.3 Body Displacement Following a Collision

The manner in which collision events are handled can lead to a instantaneous spike in the angular momentum of the system. When a collision is detected after a propagation step, the simulation rewinds to the previous state and calculates the time t_c to the collision assuming a constant acceleration. The system is then propagated by t_c after which point the bodies are assumed to be in contact. Realistically, there will be some remaining gap between the surfaces of the colliding bodies, so the simulation manually moves the two colliding bodies to be in perfect contact. This displacement is typically on the order of 10^{-3} mm; however, even a small non-physical displacement of the bodies can significantly affect the angular momentum of the system because the velocity of the bodies are not correspondingly adjusted to account for the displacement. For instance, displacing the bodies by 10^{-3} mm will change the angular momentum of the system by 10^4 $[kg \cdot km^2/s]$ due to the large mass of the bodies.

The jump in angular momentum scales with the required manual displacement of the bodies during a collision. Figure 6.5 shows the spikes in angular momentum following each collision event. The scale of the spikes is roughly correlated with the energy loss following each collisions because larger energetic collisions are associated with faster relatively moving bodies. The slower the bodies are moving, the better approximation the time to collision t_c is which correlates to a small manual displacement needed to place the bodies in contact at their surfaces.

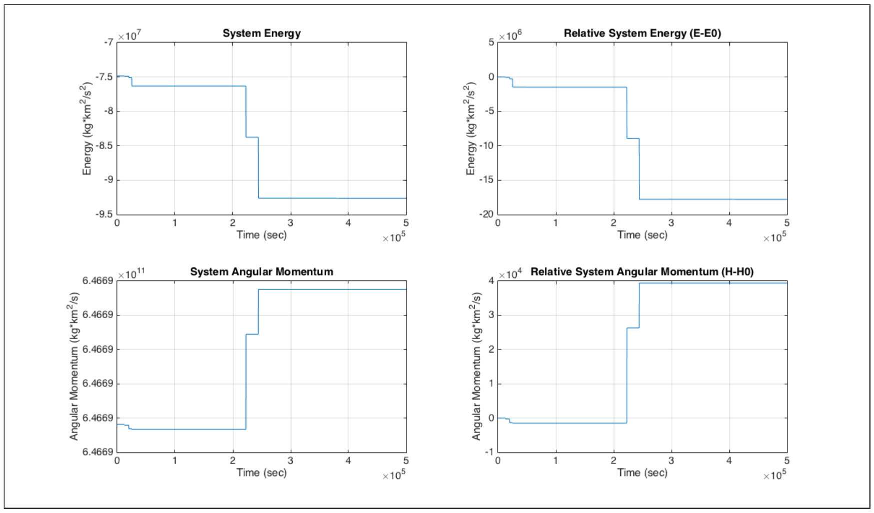

Figure 6.5: Energy and angular momentum for the Lagrange Resting to Euler Resting transition.

The angular momentum errors because of the way collisions range from $O(10^3)$ to $O(10^4)$. These are by far the largest errors that occur in the simulation. The total change to the angular momentum of the system because of these errors still amount to less than 1 part in 10^7. Such a small error does not significantly affect he behavior of the bodies nor the long-term conditions of the minimum energy configuration. Furthermore, the errors cause by this source are bounded because there are finite number of collisions during any given transition. The greatest amount of collisions occurred for the simulation of the Lagrange Resting configuration to the Euler Resting configuration, and yet the total change in system angular momentum was about 6 parts in 10^8. Clearly, even the worse-case offenders do not alter the final results of the simulation. These errors could be reduced by using a Newton-Raphson method to iteratively solve for when the bodies are in direct contact to within some desirable tolerance. This would allow control over the maximum manual displacement of the bodies and thereby bound the largest spike in angular momentum caused by this error.

6.4 Physical vs. Non-Physical Results

The behavior of the system and conclusions about the transitions are evaluated based on the macro-scale results of the simulation. However, the results constitute a mixture of physically observable behaviors and simulation artifacts. We want to separate the two different phenomena and discern which results can be expected in a physically observable system based on the governing physics. The non-physical results of the simulation are attributed to the imperfect dynamic model and propagator methodology used by the simulation; thus these non-physical effects would not be observable in a real system. Below are simulations results that represent the physical and non-physical results of the simulation:

- **Physical Simulation Results**

    1. Collisions Between Bodies - The collisions occur in a consistent manner

using impulsive momenta transfer in the absence of friction.

2. Transient Body Trajectories - The bodies evolved according to the physical effects of gravitational potentials and tidal forces that would be felt by asteroids in the absence of friction.
3. Tidal Energy Decay - The energy decayed through tidal forces represented the physical dissipation of energy caused by an undulating wave of mechanical stress propagating throughout the bodies due to asymmetric gravity gradients.
4. Tidal Rotation Synchronization - The tidal forces caused the relative orbital and rotational rates of the bodies to approach the same value, representative of a ternary asteroid system in its lowest energy state.
5. Tidal Locking Times - In a frictionless system, the time required for the bodies to reach a tidally locked state is completely dominated by the tidal torques modeled in the simulation.

- **Non-physical Simulation Results**

    1. Surface Penetration Between Bodies - The 2mm penetrations between body surfaces is non-physical and is a result of using a soft-sphere contact force model to keep contact pairs in close proximity. In a physical system, the asteroids will not penetrate and any collisional energy will go into fragmenting the contacting surfaces and generating frictional heat.
    2. Steady State Contact Surface Oscillations - The tendency for persistent

> contact bodies to oscillate normal to their surfaces is a non-physical result caused by the spring force model used to keep bodies in close proximity. In a physical system, asteroids in persistent contact will not penetrate and will approach a fixed distance from their centers. Any relative velocity along the contact normal will be dissipated through frictional heat and fragmentation.

We are only concerned with keeping contact pairs in close proximity and understanding how bodies transition between relative equilibria. Overall, the non-physical results did not affect the overall behavior or evolution of the system that we were interested in studying. All of the non-physical results of the simulation were centered around small interpenetrations of contact pairs, which had negligible effects on the transition between relative equilibria and the timescales required for tidal locking. The physically consistent results are representative of the true dynamics governing the evolution of the bodies and are adequately captured by the simulation.

Chapter 7: Conclusion

7.1 Future Work

Although the simulation was capable of demonstrating physically realistic behavior of the bodies as they transitioned between minimum energy configurations, there are a few improvements that can be made to increase the accuracy of the results. Currently, the only modeled mode of energy decay is through tidal force interactions which can happen at a distance. Bodies in contact with a nonzero relative velocity will lose rotational energy through coulomb friction. This effect will increase the rate at which bodies become tidally locked because coulomb friction would act proportional to the relative body spin rate $\dot{\phi}$. The coulomb friction force model would be integrated into the contact force model to be applied only for persistent contacts that is talked more about in a paper by Sanchez [8]. There is also a contact friction impulse that would be applied during a collision event [6]. Modeling both of these effects ultimately allows the timescales for tidal locking to be more accurately predicted.

The velocity verlet integrator introduces errors to the energy and angular momentum of the system at each time step. Because the system dynamics depend on velocity, the energy and angular momentum conserving advantages of using a symplectic integrator are not fully achieved. Furthermore, the underlying physical constraints of the system are not intrinsically known by the integrator, allowing for small penetrations to occur and altering the conserved quantities of the system. A more accurate approach would be to use a discretization of the underlying physical constraints to formulate an integrator. There are large numbers of discretized integrators used commonly for applications in simulating molecular dynamics or robotic manipulators. One attractive discretized integrator is the SHAKE algorithm, which is typically paired with a velocity verlet integration scheme [5]. At each timestep, a force derived from the physical constraint of the system is applied to the bodies so as to satisfy the physical constraints at the next state. Additionally at each step, a set of Lagrange multipliers are iteratively solved for that conserve the underlying energy and angular momentum of the system. Implementing SHAKE with a velocity verlet integrator would potentially increase the accuracy of the results while allowing larger timesteps to be taken at the cost of increased computation time per step.

Finally, the current paper assumes the bodies are perfect spheres, although the simulation is performed in the larger context of how ternary solar system bodies evolve. We would want to extend the simulation to be compatible with ellipsoidal body shapes so that physical asteroid systems could be better modeled. Much of the contact force code and collision detection works on the assumption of spherical bodies of equal diameter. Adding in a code that is generic for any set of ellipsoidal bodies would be the next step to modeling real systems. Once this change is made, one would be able to simulate observed ternary asteroid systems and predict their transition times to a tidally locked state.

7.2 Conclusion

The evolution of three finite density, self-gravitating asteroids is highly varied as the system transitions between relative equilibria configurations. The energy gap created after stable ternary asteroid systems are spun-up by the YORP effect allow the bodies to take on a variety of orbits before settling on stable configuration. The trajectory of the transitioning bodies were impossible to predict like for the case of Euler Resting configuration transitioning to the Aligned Mixed configuration. Others like the Euler Resting to Lagrange Resting transition were predictable through a V-Resting configuration that gradually declined. In all cases, the simulation provided a clear pathway for the bodies to transition into their terminal minimum energy configuration. The terminal configuration reached by each initial system confirm the expected results postulated by a purely analytic approach to the problem.

For each simulated transition, we showed that the bodies do not become stuck in a local minima. All other available equilibria other than the minimum energy configuration for each transition were energetically unstable, so we would not reasonably expect the system to become stuck in one of these other equilibria. However, this result could not be determined analytically because of the complex interactions of the dynamics. With these simulation results, we can provide evidence that the transition between minimum energy configurations is a direct process with no unusual behavior that may go against our intuition.

Furthermore, tidal forces were shown to transfer angular momentum and rotational energy between bodies from a distance. In this way, tidal torques would synchronize the relative spin rates between the bodies and decay stored excess mechanical energy. The measured rate of energy decay was shown to be consistent with the analytic model used to generate the tidal torques and tidal forces. From the steady state tidal torque, we were able to estimate the time required for the bodies to reach a tidally locked state, and thus when the system will perfectly conform to the predicted minimum energy configuration. The transient and long term behavior of these bodies is exciting and complex, motivating a more comprehensive analysis of the transitions between equilibrium configurations.

Appendix A: Fast Contact Force Model

A.1 Further Discussion of Algorithm

By differentiating equation 3.36 twice with respect to time, the following expression is obtained:

$$\ddot{d}_i(t) = \ddot{\hat{n}}_i(t) \cdot (p_A(t) - p_B(t)) + 2\dot{\hat{n}}_i(t) \cdot (\dot{p}_A(t) - \dot{p}_B(t)) + \hat{n}_i(t) \cdot (\ddot{p}_A(t) - \ddot{p}_B(t)) \quad \text{(A.1)}$$

Assuming the surfaces of Body A and B are just touching at time t_0, that is, $p_A(t_0) = p_B(t_0)$, the final expression is simply:

$$\ddot{d}_i(t_0) = 2\dot{\hat{n}}_i(t_0) \cdot (\dot{p}_A(t_0) - \dot{p}_B(t_0)) + \hat{n}_i(t_0) \cdot (\ddot{p}_A(t_0) - \ddot{p}_B(t_0)) \quad \text{(A.2)}$$

The first normal force condition for the fast contact force model is thus:

$$\ddot{d}_i(t_0) \geq 0 \quad \text{(A.3)}$$

As a matter of convention, say a contact force $f_i\hat{n}_i$ acts on Body A at the i^{th} contact point. Physically, we know that contact forces must be either 0 or repulsive, and since $\hat{n}_i$ points from Body B to Body A by convention, we arrive at the second normal force condition:

$$f_i \geq 0 \tag{A.4}$$

These two contact force conditions are actually coupled, as there is an underlying symmetry between their articulations. If $\ddot{d}_i$ is greater than 0, the bodies will separate so there will be no contact forces, $f_i = 0$, between Bodies A & B at the i^{th} contact point. Similarly, if $\ddot{d}_i = 0$, there must be a nonzero contact force to prevent Bodies A & B from interpenetrating. These ideas and the previous conditions come together to form the final normal force condition:

$$f_i \ddot{d}_i(t_0) = 0 \tag{A.5}$$

Finally, we must consider the external and internal forces acting on each contact point and how they interact with the calculated contact forces. The external forces, like gravity, linearly affect the contact point acceleration. For a multi body system, the sum of all gravitational forces at the i^{th} contact point, b_i is applied to $\ddot{d}_i$. Simply put:

$$\ddot{d}_i \propto b_i \tag{A.6}$$

The internal forces are the contact forces present at each contact point. For a simple two-body system with a single contact point, the interaction between the contact force and the contact point acceleration $\ddot{d}_i$ is trivial. For a multi body system with n contact points, the applied contact force at a contact point will affect the acceleration of the other contact points. Because of this interdependent nature, the contact forces must be solved for simultaneously. In general, we can derive a matrix $\mathbf{A_{n,n}}$ that quantitatively relates how the gap acceleration of contact point i is affected by the contact forces $f_1, f_2, ...f_n$.

$$\ddot{d}_i \propto \mathbf{A_i}[f_1, f_2, ...f_n]^T \tag{A.7}$$

The effects of the external and internal forces acting on each contact point can be compactly expressed in matrix form: [6]

$$\begin{bmatrix} \ddot{d}_1(t_0) \\ \vdots \\ \ddot{d}_n(t_0) \end{bmatrix} = \mathbf{A} \begin{bmatrix} f_1(t_0) \\ \vdots \\ f_n(t_0) \end{bmatrix} + \begin{bmatrix} b_1(t_0) \\ \vdots \\ b_n(t_0) \end{bmatrix} \tag{A.8}$$

Or more simply:

$$\mathbf{a} = \mathbf{Af} + \mathbf{b} \tag{A.9}$$

Where

$\mathbf{a}$ = (n x 1) column vector of $\ddot{d}_i(t_0)$

$\mathbf{A}$ = (n x n) matrix governing how contact force f_j affects the acceleration of contact point i

$\mathbf{b}$ = (n x 1) column vector of how external forces affect the acceleration of contact point i

$\mathbf{f}$ = (n x 1) column vector of contact forces to be solved for

This system of equations and the underlying contact force conditions represent a Quadratic Programming (QP) problem. Solving the problem and satisfying the constraints is a matter of optimization, given by the refined problem statement below:

$$\min_{f} \ \mathbf{f}^T(\mathbf{Af}+\mathbf{b}) \text{ Subject to: } \begin{cases} \mathbf{Af}+\mathbf{b} \geq \mathbf{0} \\ \\ \mathbf{f} \geq \mathbf{0} \end{cases} \tag{A.10}$$

There are a number general QP solvers available that can solve this NP-hard problem, including two built-in MATLAB optimization routines, quadprog and fmincon. The result from solving this QP problem is a vector of contact forces f_i that, when applied to each body at the i^{th} contact, prevents any interpenetration while allowing the bodies to behave in a physically accurate way. The remaining problem is solving for the elements a_{ij} of $\mathbf{A}$ and b_i of $\mathbf{b}$. The expressions for calculating A and b are listed further on in this appendix.

However in practice, solving this QP is computationally expensive and the solvers would routinely fail to find a valid solution. Ideally we would like a solution to always be found, even if numerical inaccuracies produce some small surface penetration between the bodies. Furthermore, solving the system as a QP undermines the simpler condition of each contact force $f_i a_i = 0$. By attempting to solve the more general problem of $\mathbf{f}^T\mathbf{a}$, we are solving a much harder problem than necessary. Barraff solves this issue by applying a more specific solver algorithm known as the Pivot Step method.

The Pivot Step method has been specially adapted by David Barraff for the efficient computation of contact forces in modeling real-time systems. [7] The goal of the algorithm is to increase the contact force at each sequential contact point so that the normal force conditions hold at this and all previously inspected contact points. Contact points are split between two sets: Clamped {C} and Not Clamped {NC}. The Clamped contact points are those with $a_i = 0$ such that the bodies are effectively locked to one another. The Not Clamped contact points are those with $f_i = 0$ such that the bodies are free to separate. The general procedure for the algorithm is outlined as follows:

1. Set all contact forces $\mathbf{f}$ to 0 and let the acceleration of the contact points a_i be equal to the external forces b. Thus all contact points are currently in the {NC} set.

2. Find the first contact point with a negative gap acceleration, call it contact point d.

3. Increase the contact force at point d by a unit step and compute how this changes the other contact forces in the Clamped set $\{C\}$, collectively labeled as $\mathbf{\Delta f}$.

4. Compute the largest scalar factor s that multiplies $\mathbf{\Delta f}$ and is added to $\mathbf{f}$ such that clamped points retain $a_i = 0$ and unclamped points retain $f_i = 0$.

5. During this cycle, if any clamped point has $f_i = 0$, then the i^{th} contact point is considered unclamped and moved to the {NC} set. The same is true if an

unclamped point has $a_i = 0$, except now it's considered clamped and moved to the {C} set. This switching of points between sets is known as pivoting.

6. The algorithm terminates when there are no longer any negative accelerations a_i for $i = 1 : n$.

The Pivot Step method is advantageous over traditional QP solvers for a few reasons. Most importantly, a solution is always guaranteed to exist [citation] even in the event that matrix **A** is singular. Empirically, the Pivot Step algorithm produces more accurate results and has a shorter computation time compared to the QP solver quadprog & fmincon. Although this method produces very accurate, instantaneous results and maintains the physical constraint of the rigid bodies well, its interaction with the numerical propagator of choice lead to unstable energy increases.

A more detailed pseudo-code arrangement of the algorithm can be found in [7].

A.2 Solving for A

Start with the expression for the contact gap acceleration at the i_{th} contact point:

$$\ddot{d}_i(t_0) = 2\dot{\hat{n}}_i(t_0) \cdot (\dot{p}_A(t_0) - \dot{p}_B(t_0)) + \hat{n}_i(t_0) \cdot (\ddot{p}_A(t_0) - \ddot{p}_B(t_0)) \tag{A.11}$$

When calculating the elements of **A**, a_{ij}, the only concern are terms that depend on contact force at the j^{th} contact point, f_j. The term $\hat{n}_i(t) \cdot (\ddot{p}_A(t_0) - \ddot{p}_B(t_0))$

is only dependent on already known velocities of the contact point, so this term will be lumped into the **b** matrix.

Next consider the contact force f_j at the j^{th} contact point. If neither Body A nor Body B is involved at the j^{th} contact point, then f_j has no direct effect on $\ddot{d}_i$ and thus $a_{ij} = 0$.

Suppose Body A is involved at the j^{th} contact such that a force $+f_j\hat{n}_j$ acts on Body A. We are interested in calculating how $\ddot{p}_A(t_0)$ is affected by this force. Let's start by defining some preliminary variables:

$x_A =$ center of mass of body A in inertial frame

$r_A =$ vector from center of mass of Body A to the i-th contact point

$r_{j,A} =$ vector from center of mass of Body A to the j-th contact point

$\omega_A =$ angular velocity of Body A

$v_A = \dot{x}_A =$ velocity vector of center of mass of Body A

$m_A =$ mass of Body A

Then $p_A = x_A + r_A$ and by differentiating twice with respect to time, the following expression is obtained:

$$\ddot{p_A}(t) = \dot{v}_A(t) + \dot{\omega}_A(t) \times r_A(t) + \omega_A(t) \times (\omega_A(t) \times r_A(t)) \tag{A.12}$$

The last term $\omega_A(t) \times (\omega_A(t) \times r_A(t))$ only depends on velocity and so will contribute to the **b** vector. The term $\dot{v}_A(t)$ is the linear acceleration of Body A and is given by Newton's law: $\dot{v}_A(t) = \frac{\sum \text{forces acting on A}}{m_A}$. The f_j dependent part of $\dot{v}_A = f_j\hat{n}_j/m_A$.

Similarly, we need an expression for $\dot{\omega}_A$. One starts with $L_A(t) = I_A(t)\omega_A(t)$, where $L_A(t)$ is the angular momentum of Body A and $I_A(t)$ is the moment of inertia matrix representing Body A (which for a spherical body is just a constant). Differentiating both sides with respect to time and solving for $\dot{\omega}_A(t)$ yields:

$$\dot{\omega}_A(t) = \dot{I}_A^{-1}(t)L_A(t) + I_A^{-1}(t)\dot{L}_A(t) \tag{A.13}$$

David Baraff derives another workable form of the equation:

$$\dot{\omega}_A(t) = I_A^{-1}(t)(L_A(t) \times \omega_A(t) + \dot{L}_A(t)) \tag{A.14}$$

Note that $\dot{L}_A(t) = \tau_A(t)$, the total torque acting on Body A. Any external torques will fit into this equation but those terms will be later grouped into the b vector. There will be a torque exerted on Body A due to the j^{th} contact force located at p_j. This is expressed as:

$$\tau_{A,int} = (p_j - x_A(t_0)) \times f_j\hat{n}_j \tag{A.15}$$

However, in the case of perfectly spherical bodies, this extra torque term will always be 0 because the j^{th} contact force vector and the line joining the center of Body A and the j^{th} will always be parallel. Nevertheless, the angular contribution to $\ddot{p}_A$ will be:

$$f_j(I_A^{-1}(t_0)((p_j - x_A(t_0)) \times \hat{n}_j(t_0))) \times r_A \tag{A.16}$$

And finally, the total dependence of $\ddot{p}_A$ on f_j is given by:

$$f_j(\hat{n}_j/m_A + I_A^{-1}(t_0)((p_j - x_A(t_0)) \times \hat{n}_j(t_0))) \times r_A \tag{A.17}$$

Similarly, $\ddot{p}_B$ depends on f_j in the same way, except a force of $-f_j\hat{n}_j$ would affect Body B, thus a minus sign would appear in front of the equation. These two results are combined and dotted with $\hat{n}_j$ as it appears in equation A.11 to obtain $a_{i,j}$.

A.3 Solving for b

The b vector is calculated using all the remaining terms that do no depend on any contact forces f_i. From equation A.11, we can pull out the term: $2\dot{\hat{n}}_i(t_0) \cdot (\dot{p}_A(t_0) - \dot{p}_B(t_0))$, which depends only on the velocity of each point on the body in contact. The velocity of each point in contact, $\dot{p}_{A/B}$ can be calculated by:

$$\dot{p}_A = v_A + \omega_A \times r_A \tag{A.18}$$

The remaining contact force independent terms comes from the calculation of $\ddot{p}_{A/B}$. These terms are a result of external gravity forces and external torques, in addition to force-independent terms.

- External Force on Body A: F_A/m_A
- External Torque on Body A: $(I_A^{-1}(t_0)\tau_{A,ext}(t_0)) \times r_A$
- $\omega_A(t_0) \times (\omega_A(t_0) \times r_A(t_0))$

- $(I_A^{-1}(t_0)(L_A(t_0) \times \omega_A(t_0))) \times r_A$

Thus, the final expression for $\ddot{p}_A$ independent of f_j is:

$$F_A/m_A + ((I_A^{-1}(t_0)\tau_{A,ext}(t_0)) + \omega_A(t_0) \times (\omega_A(t_0)) + (I_A^{-1}(t_0)(L_A(t_0) \times \omega_A(t_0)))) \times r_A \tag{A.19}$$

The same calculation is performed for $\ddot{p}_B$ and the two results are combined and dotted with $\hat{n}_j$ following equation A.11. This term is then added to the term $2\dot{\hat{n}}_i(t_0) \cdot (\dot{p}_A(t_0) - \dot{p}_B(t_0))$ to obtain b_i. Once the **A** and **b** matrices are calculated, the next step is to find an appropriate solution of contact forces that satisfy the normal force conditions.

Appendix B: Derivation of Reduced System

The state variables used in the dynamics and for calculations are based on an inertial reference frame I where the position and angle of each body is specified in terms of cartesian coordinate system with an origin defined at the system barycenter. Using this coordinate system, there are nine state variables and nine degrees of freedom (DOF) - two position coordinates and one angle for each of the three bodies. The system has three notionally conserved quantities assuming no energy dissipation modes: the conserved quantities are the linear momenta along the X and Y axes and the angular momentum of the system. Using these conserved quantities, it is possible to reduce the system from nine DOF to six DOF, thereby reducing the number of state variables from nine to six.

The body coordinates can be redefined in terms relative to the other two bodies. The origin of the reduced coordinate system B_1 is placed at the center of body 1 and rotates with body 1. Then the reduced positions of the three bodies are defined as:

$$ {}^{B_1}\vec{r}_1 ={}^{I} \vec{r}_1 -{}^{I} \vec{r}_1 = \vec{0} \qquad \text{(B.1)} $$

$${}^{B_1}\vec{r}_2 ={}^I \vec{r}_2 -{}^I \vec{r}_1 \tag{B.2}$$

$${}^{B_1}\vec{r}_3 ={}^I \vec{r}_3 -{}^I \vec{r}_1 \tag{B.3}$$

where ${}^{B_1}\vec{r}_i$ is the position of body i $(i = 1, 2, 3)$ with respect to the center of body 1, and ${}^I\vec{r}_i$ is the position of body i with respect to an inertial reference frame I. Similarly, the rotation angle of each body is specified relative to the rotation of body 1:

$${}^{B_1}\theta_1 ={}^I \theta_1 -{}^I \theta_1 = 0 \tag{B.4}$$

$${}^{B_1}\theta_2 ={}^I \theta_2 -{}^I \theta_1 \tag{B.5}$$

$${}^{B_1}\theta_3 ={}^I \theta_3 -{}^I \theta_1 \tag{B.6}$$

where ${}^{B_1}\theta_i$ is the position of body i with respect to the rotation of body 1, and ${}^I\theta_i$ is the rotation of body i with respect to the +X direction of the inertial reference frame I.

Bibliography

[1] D. J. Scheeres. Minimum energy configurations in the n-body problem and the celestial mechanics of granular systems. *Celestial Mechanics and Dynamical Astronomy*, 113(3):291–320, 2012.

[2] William F. Bottke, David Vokrouhlicky Jr., David P. Rubincam, and David Nesvorny. The yarkovsky and yorp effects: Implications for asteroid dynamics. *The Annual Review of Earth and Planetary Science*, pages 157–185, 2006.

[3] Seth A. Jacobson and Daniel J. Scheeres. Dynamics of rotationally fissioned asteroids: Source of observed small asteroid systems. *Icarus*, 214(1):161–178, July 2011.

[4] D. C. Lewis. Comments on the sundman inequality. Technical report, NASA, January 1968.

[5] Benedict J Leimkuhler and Robert D. Skeel. Symplectic numerical integrators in constrained hamiltonian systems. 1994.

[6] David Baraff. *An Introduction to Physically Based Modeling: Rigid Body Simulation II—Nonpenetration Constraints.* Robotics Institute: Carnegie Mellon University, 1997.

[7] David Baraff. Fast contact computation for nonpenetrating rigid bodies. In *Computer Graphics Proceedings, Annual Conference Series*, 1994.

[8] Paul Sanchez and Daniel J. Scheeres. Simulating asteroid rubble piles with a self-gravitating soft-sphere distinct element method model. *The Astrophysical Journal*, February 2011.

[9] Carl D. Murray and S. F. Dermott. *Solar System Dynamics.* Cambridge University Press, 1999.

[10] Patrick Alan Taylor. *Tidal Interactions in Binary Asteroid Systems.* PhD thesis, Cornell University, May 2009.

[11] C. Z. Zhang. Love numbers of the moon and of the terrestrial planets. *Earth, Moon, and Planets*, 56(3):193–207, March 1992.

[12] P. Goldreich and S. Soter. Q in the solar system. *Icarus*, 5:375–389, 1966.

[13] K.S. Krishnaswamy. *Astrophysics: A Modern Perspective.* New Age International Pvt Ltd Publishers, 2006.

[14] Desmond J. Higham and Llyod N. Trefethen. Stiffness of odes. January 1992.

[15] J. R. Dormand and P. J. Prince. A family of embedded runge-kutta formulae. *Journal of Computational and Applied Mathematics*, 6(1):19–26, 1980.

[16] M. P. Allen and D. J. Tildesley. *Computer Simulation of Liquids.* Oxford University Press, 1991.

[17] William C. Swope, Hans C. Andersen, Peter H. Berens, and Kent R. Wilson. A computer simulation method for the calculation of equilibrium constants for the formation of physical clusters of molecules. *AIP*, 76, 1982.

[18] Robert D. Skeel, Guihua Zhang, and Tamar Schlicks. A family of symplectic integrators: Stabilty, accuracy, and molecular dynamics applications. *Society for Industrial and Applied Mathematics*, 18(1):203–222, January 1997.

[19] Liz Bradley. *Numerical Solution of Differential Equations.* Department of Computer Science, University of Colorado, Boulder, Colorado, USA 80309, 2002.

[20] Horizons web-interface, http://ssd.jpl.nasa.gov/horizons.cgi, Novemeber 2016.